# FUNCTIONALIZATION OF GRAPHENE AND STOICHIOMETRIC GRAPHENE DERIVATIVES

A DISSERTATION SUBMITTED TO
THE INSTITUTE OF MATERIALS SCIENCE AND NANOTECHNOLOGY
AND THE GRADUATE SCHOOL OF ENGINEERING AND SCIENCE
OF BILKENT UNIVERSITY
IN PARTIAL FULFILLMENT OF THE REQUIREMENTS
FOR THE DEGREE OF
DOCTOR OF PHILOSOPHY

By
Hasan Şahin
December, 2011

I certify that I have read this thesis and that in my opinion it is fully adequate, in scope and in quality, as a dissertation for the degree of doctor of philosophy.

Prof. Dr. Salim Çıracı(Advisor)

I certify that I have read this thesis and that in my opinion it is fully adequate, in scope and in quality, as a dissertation for the degree of doctor of philosophy.

Prof. Dr. R. Tuğrul Senger

I certify that I have read this thesis and that in my opinion it is fully adequate, in scope and in quality, as a dissertation for the degree of doctor of philosophy.

Prof. Dr. Engin Umut Akkaya

I certify that I have read this thesis and that in my opinion it is fully adequate, in scope and in quality, as a dissertation for the degree of doctor of philosophy.

Prof. Dr. Taner Yıldırım

I certify that I have read this thesis and that in my opinion it is fully adequate, in scope and in quality, as a dissertation for the degree of doctor of philosophy.

Assoc. Prof. Dr. Dönüş Tuncel

Approved for the Graduate School of Engineering and Science:

Prof. Dr. Levent Onural
Director of the Graduate School

# ABSTRACT

## FUNCTIONALIZATION OF GRAPHENE AND STOICHIOMETRIC GRAPHENE DERIVATIVES

Hasan Şahin
Ph.D. in Materials Science and Nanotechnology
Supervisor: Prof. Dr. Salim Çıracı
December, 2011

Recent developments in experimental techniques have made the design and production of materials at nanoscale possible. In particular, graphene has been the focus of research in diverse fields owing to high mobility carrier transport and other exceptional properties. Over the past four years experimental studies have demonstrated that chemical conversion of graphene to its stoichiometric derivatives is possible by hydrogenation, fluorination and chlorination. The aim of this thesis is to predict stable stoichiometric graphene derivatives and explore their mechanical, electronic and magnetic properties. Moreover, the functionalization of graphene and its derivatives are achieved, whereby their physical properties are modified to derive novel materials. Our predictions revealing stable 2D single layer conformers, which can be used as novel nanocoeting materials, are obtained from state-of-the art first-principles Density Functional calculations of total energy, phonons, transition state analysis and ab-initio molecular dynamics.

An extensive theoretical study on the stability of hydrogenated graphene ($C_nH$), fully hydrogenated graphane i.e graphane (CH), and their quasi one-dimensional nanoribbons is performed. The formation of meshes of dehydrogenated domains on graphane resulted in geometry specific magnetic structures showing interesting magnetic interactions. Creation of H and CH vacancies, as well as adsorption of transition metal atoms give rise to significant spin-polarization in graphane nanoribbons. It is shown that as a result of one-sided or two-sided fluorination of graphene one can obtain nanostructures with diverse electronic and magnetic properties. Fully fluorinated graphene or fluorographene CF is a stable, stiff and non-magnetic semiconductor. Additionally, this conformer of buckled graphene is functionalized by alkali, non-metal, metalloid and transition metal atoms, and each group leads to diverse adsorption properties.

Adsorption of chlorine to graphene is dramatically different from those of hydrogen and fluorine. While the binding energy of chlorine is significant, its migration on the surface of perfect graphene takes place almost without barrier. This is crucial for energy harvesting on graphene surface. Energy optimization and phonon calculations indicate that the chair configuration of fully chlorinated graphene (chlorographene) is energetically most favorable and stable. It is a nonmagnetic semiconductor with 1.2 eV direct band gap, which can be tuned by applied uniform strain.

Graphene by itself can be functionalized by creating meshes of vacancies or adatoms conserving specific symmetries. Under these circumstances linearly crossing bands and hence the massless Dirac Fermion behavior can be maintained.

Finally, it is demonstrated that multilayer, even single layer graphene constitute an excellent nanoscale coating, which can prevent a reactive metal surface from oxidation without changing the size and other physical properties. Graphene can stick to flat metal surfaces and hinders free oxygen atom and molecule from penetrating to the metal surface. Single layer fluorographene can be used also for the same purposes.

Design of novel nanomaterials, in particular biological molecules and complexes using first-principles methods derived from quantum theory indicates a new direction in theory, which promises a productive hybridization with experimental studies.

*Keywords:* Graphene, Stoichiometric Graphene Derivatives, Nanocoating, Fluorographene, Graphane, Chlorographene.

# ÖZET

# GRAFİNİN FONKSİYONELLEŞTİRİLMESİ VE STOKİYOMETRİK GRAFİN TÜREVLERİ

Hasan Şahin
Malzeme Bilimi ve Nanoteknoloji, Doktora
Tez Yöneticisi: Prof. Dr. Salim Çıracı
Aralık, 2011

Deneysel tekniklerdeki son gelişmeler nano boyutlu malzemelerin dizaynını ve üretimini mümkün kılmıştır. Özellikle grafin, yüksek hızlarda elektron taşınımı ve diğer üstün özellikleri dolayısıyla çeşitli araştırma alanlarının ilgi odağı olmuştur. Geçtiğimiz dört yıl boyunca yapılan deneysel çalışmalar grafinin hidrojenlenmesi, florlanması ve klorlanması yolu ile stokiyometrik türevlerine kimyasal dönüştürülebileceğini göstermiştir. Bu tez çalışmasının amacı olası grafin türevlerinin varlığını öngörerek bunların mekanik, elektronik ve manyetik özelliklerinin araştırılmasıdır. Ayrıca, modifiye edilmiş fiziksel özelliklere sahip yeni malzemeler elde etmeye olanak sağlayan, grafin ve türevlerinin işlevselleştirilmesi mümkündür. Yeni nano kaplama malzemeleri olarak kullanılabilecek sağlam iki boyutlu malzemelerin varlığına işaret eden sonuçlarımız toplam enerji, fonon, geçiş durumu ve moleküler dinamik için üst seviyede temel ilkeler yoğunluk fonksiyoneli kuramı kapsamında yürütülen hesaplardan elde edilmiştir.

Hidrojenlenmiş grafin ($C_nH$), grafan olarak adlandırılan tümüyle hidrojenlenmiş grafin (CH) ve bunların bir boyutlu nanoşeritlerinin kapsamlı analizi yapılmıştır. Grafan üzerinde dehidrojene edilmiş bölgelerin geometrisine bağlı olarak ilginç manyetik etkileşmelere sahip olduğu gösterilmiştir. Grafan üzerinde H ve CH kusurlarının oluşturulması ve ayrıca geçiş metali atomlarının bağlanması yolu ile grafan nanoşeritlerde dikkate değer miktarda spin polarizasyonu sağlar. Ayrıca grafinin tek ve çift yüzeyinin florlanması sonucu olarak çeşitli elektronik ve manyetik özelliklere sahip olan nanoyapıların elde edilebileceği gösterilmiştir. Florografin olarak bilinen, tümüyle florlanmış grafin, sğlam, gerilmelere karşı dayanıklı ve manyetik olmayan bir yarıiletken malzemedir. Florografinin alkali, metal olamayan, metaloid ve geçiş metali ile işlevselleştirilmiştir ve her bir atom grubun farklı bağlanma karakteristiklerine sahiptir.

Klor atomunun grafine absorbe olması hidrojen ve fluor atomuna göre oldukça farklıdır. Klor atomunun grafine baǵlanması çok güçlü olmasına raǵmen, yüzey üzerindeki hareketi neredeyse bariyersizdir. Bu, grafin yüzeyinde enerji elde edilmesi için büyük öneme sahiptir. Enerji optimizasyonları ve fonon hesaplamaları, tümüyle klorlanmış grafinin (klorografin) chair halinin enerjetik olarak en tercih edilebilir ve saǵlam yapı olduǵunu göstermiştir. Klorografin, germe yoluyla deǵiştirilebilir olan 1.2 eV yasak band aralığına sahip ve manyetik olmayan yarıiletkendir

Grafin tek başına belli simetrilere uyan yapısal kusurlar ve adsorbe edilmiş atom grupları ile işlevselleştirilebilirdir. Bu yapılarda lineer olarak çakışan bantların varlığı da korunabilmektedir. Hatta belli durumlar için kütlesiz Dirac fermiyonu davranışı bile elde edilmektedir.

Son olarak, çok tabakalı ve hatta tek tabakalı grafin malzemelerin, reaktif metal yuzeylerinin boyut ve diǵer fiziksel özelliklerini deǵiştirmeksizin koruyan, mükemmel nano ölçek kaplama malzemeleri olduǵu gösterilmiştir. Grafin düz metal yüzeylere yapışabilir ve serbest oksijen atomunun ve molekülünün metal yüzeye sızmasına engel olur. Tek tabaka florografin de benzer amaçlar için kullanılabilirdir.

Özellikle biyolojik molküller ve kompleksler gibi yeni nanomalzemelerin kuantum teorisinden türeyen yoǵunluk fonksiyoneli kuramı ile dizayn edilmesi teori açısından yeni bir doǵrultuya işaret etmektedir.

*Anahtar sözcükler*: Grafin, Stokiyometrik Grafin Türevleri, Nanokaplama, Florografin, Grafan, Klorografin.

# Acknowledgement

Foremost, I would like to express my sincere gratitude to my advisor Prof. Dr. Salim Çıracı for the continuous support of my Ph.D study and research, for his motivation, enthusiasm, and immense knowledge. I am deeply grateful to him for giving me the confidence to explore my research interests and the guidance to avoid getting lost in my exploration. His guidance helped me in all the time of research and writing of this thesis.

I am deeply grateful to my co-advisor Prof. Dr. R. T. Senger, for opening the doors of Bilkent University to me and attracting my interest to spintronics and nanotechnology.

Also I thank my friends Engin Durgun, Sefa Dağ and Haldun Sevinçli for their valuable friendship and guidance.

I also thank my groupmates: Seymur Cahangirov, Can Ataca, Mehmet Topsakal and Ethem Akturk, for the stimulating discussions, for the sleepless nights we were working together before paper submissions, and for all the fun we have had in the last four years.

I would like to thank my parents for giving birth to me at the first place and supporting me spiritually throughout my life. They are always the compass of my life.

Lastly, I owe my loving thanks to my wife Şeyda Horzum Şahin. Without her encouragement, patience and understanding it would have been impossible for me to finish this work.

# Contents

# List of Figures

# List of Tables

# Chapter 1

# Introduction

The industrial revolution of the late eighteenth century had a major impact on almost every aspect of industry, machinery and daily life in a manner that very few other developments in the world have. Subsequent technological and scientific developments opened the way of realization of novel materials that are the parts of devices operating at one millionth of a meter. However, ability to measure and design at micro-scale not only led to the emergence of microscopic devices but also provide equipments to explore the world at the smaller dimensions. Nowadays, in the rapidly developing field of nanotechnology, researchers are taking control of atoms and molecules individually, manipulating them and putting them to use with an extraordinary degree of precision. Over the last decade, nanoscience and emerging nanotechnologies have been dominated by honeycomb structured carbon based materials in different dimensionality, such as fullerenes, single and multi walled carbon nanotubes, graphene and its nanoribbons. In particular, graphene, a two dimensional (2D) honeycomb structure of carbon, has been an active field of research for last seven years.

In this thesis we mainly focus on the use of graphene and graphene-based chemical derivatives as nano-scale coating materials that can protect reactive surfaces underneath by posing a high energy barrier surface. The reaction of material surfaces with foreign atoms and controlling damages from corrosion have been the

subject of intensive research for decades. While the protective coatings of reactive surfaces at macroscale resulted in the change of size and physical properties, protection against corrosion at nanoscale has required new paradigms using ultrathin and nanocomposite coatings. Graphene, being not only the thinnest ever but also the strongest material, has the potential for nano-coating applications. When sticks to or grown on various surfaces, graphene adds only 3-6 Å to the size of underlying sample and forms an electrically and thermally conductive coating on it. Moreover, graphene has exceptional thermal and chemical stability; it is stable up to temperatures higher than 1500 C under inert environment. It is also stable under many conditions where other substrates would undergo rapid chemical reactions ending with degradation. With these properties graphene keep the promises of being an excellent candidate for a nanoscale protection layer against corrosion.

Although graphene is one of the most mechanically strong material having a wide range of extraordinary properties, practical device applications are limited by it's metallic behavior and tendency to interact with environment. Efforts to manufacture of chemically modified graphene composites with tailored electronic, optical, and chemical properties present an exciting new direction in graphene research. In particular, band gap engineering of graphene through chemical modification such as oxygenation, and hydrogenation is appealing for electronic applications since it facilitates the scalable fabrication of graphene-based devices without disturbing the strong honeycomb lattice. However, due to the complex atomic structure of grapheneoxides and thermal instabilities of hydrogenated graphenes even at low temperatures, search for the novel graphene-based materials is still continuing. Recent studies have also revealed that oxygenated, hydrogenated and fluorinated derivatives of graphene having diverse electronic and mechanic properties can be synthesized. Easy manufacturability, high-quality insulating behavior and extraordinary mechanical strength of fluorographene (CF) have inspired intense research on other halogen decorated graphene derivatives. In this thesis we also present electronic, magnetic, mechanic and vibrational properties of CH, CF and CCl. It was shown that these derivatives are as strong as graphene, quite flexibile and stable at high temperatures. From the technological point of

view, graphene composites having saturated surfaces are also good candidates for chemically stable and mechanically strong protection layer. Since fluorographene is the most stable derivative among the experimentally realized materials we also examine the performance of CF as a coating material.

The thesis begins with this brief introduction, followed by a chapter on the basics of density functional theory and stability analysis of nanoscale materials within the framework of ab initio methods. In Chapter III, it is predicted that each hydrogen vacancy created at the surface of hydrogenated graphene, namely graphane, results in a local unpaired spin. For domains of hydrogen vacancies the situation is, however complex and depends on the size and geometry of domains, as well as whether the domains are single or double-sided. Owing to the different characters of exchange coupling in different ranges and interplay between unpaired spin and the binding geometry of hydrogen, vacancy domains can attain sizable net magnetic moments.

In Chapter IV, the electronic and magnetic properties of graphane nanoribbons are investigated. It is found that zigzag and armchair graphane nanoribbons with H-passivated edges are nonmagnetic semiconductors. While bare armchair nanoribbons are also nonmagnetic, adjacent dangling bonds of bare zigzag nanoribbons have antiferromagnetic ordering at the same edge. Band gaps of the H-passivated zigzag and armchair nanoribbons exponentially depend on their width. Detailed analysis of adsorption of C, O, Si, Ti, V, Fe, Ge and Pt atoms on the graphane ribbon surface reveal that functionalization of graphane nanoribbons is possible via these adatoms.

In Chapter V, fluorination of graphene are investigated. Analysis of fluorinated graphenes shows that different $C_nF$ structures can form at different level of F coverage. Calculated properties of these structures, such as lattice parameter, $d_{CC}$ distance, band gap, density of states, work function, in plane stiffness $C$, Poisson's ratio and surface charge, are shown to depend on the level of coverage. Perfect fluorographene structure is a stiff, nonmagnetic wide band gap nanomaterial having substantial surface charge, but attains significant local magnetic moment through F-vacancy defects. Moreover, unlike graphane, half fluorinated

graphene with only one side fluorinated is found to be stable, which can be further functionalized by the adsorption of adatoms to other side. It is also noted that relevant data reported in various experiments do not appear to agree with the properties calculated any one of the stable $C_nF$ structures. This finding lets us to conclude that domains of various $C_nF$ structures can form in the course of the fluorination of graphene. Therefore, the experimental data may reflect a weighted average of diverse $C_nF$ structures together with extended defects in grain boundaries.

In Chapter VI, analysis of the interaction of chlorine atoms with graphene and the presence of possible chllorinated graphene derivatives are presented. It is found that differing from hydrogen and fluorine adatoms, while the binding of single chlorine atom to graphene is significant, its migration on the surface of perfect graphene takes place almost without barrier. It is also found that strong Cl-Cl coupling in one sided high chlorine coverage of graphene hinders the formation of boat, armchair and zigzag configuration. While the bonding of single chlorine atom leads to ionic bonding and negligible local distortion in the planar graphene, full chlorine coverage (chlorographene) where one chlorine atom is bonded alternatingly to each carbon atom from different sides gives rise to the buckling and covalent $sp^3$-bonding. Phonon and electronic energy structure of chlorographene, a stoichiometric graphene derivative, largely deviate from those of graphene. Energy optimization and phonon calculations indicate that the chair configuration of fully chlorinated graphene (chloragraphene) is energetically favorable and stable structure. It is a semiconductor with 1.2 eV direct band gap, which can be tuned by applied uniform strain. However, Cl vacancy defects can lead to dissociations of bound Cl atoms at high temperature.

In Chapter VII, it is demonstrated that continuous coating of pristine graphene on reactive surfaces can provide for an excellent protection from oxidation of reactive surfaces at nanoscale. The binding of oxygen atom at low coordinated carbon atoms is rather high, but their barrier to penetrate to the reactive surface under graphene is low. Therefore discontinuities in graphene coating or defects, such as vacancies or holes weaken the protection from oxidation by creating spots on the coating with low oxidation barrier. This limitation can be

circumvented by coating of bilayer or preferably graphene sheets comprising a few graphene layers, which provides even more effective protection. At macroscale, results are suggested that graphene additives can improve the strength of antioxidant paints. Graphene coating, which is thin at the atomic scale can also serve as a natural barrier between environment and solid surfaces for other atoms.

In Chapter VIII, functionalization of graphene via nanomeshes is investigated. Crystal structure of graphene and its symmetry properties are investigated by means of tight-binding model of $\pi$ electrons. It is predicted that adatom and hole patterned graphene nanomeshes can have metallic and semiconductor behavior. In particular the meshes providing six and threefold rotational symmetires maintain the Dirac fermions. It is also shown that depending on the mesh size and adsorbate atoms, velocity of the fermions and the magnetic ground state of the structure can be tuned. Zigzag and armchair edged hole arrays of meshes can also be in different states ranging from metallic to semiconducting including semimetallic state with the bands crossing linearly at the Fermi level.

Finally, the findings on the functionalized graphene structures and stoichiometric graphene derivatives are concluded in Chapter XI.

# Chapter 2

# Computational Methodology

This chapter of the thesis is devoted to the basics of computational many-body theory, relevant approximate functionals and the stability analysis of the structures via determination of phonon spectra.

## 2.1 Density Functional Theory

Density functional theory (DFT) is an extremely successful quantum mechanical approach modelling method for the description of ground state properties of metals, semiconductors and insulators. With this theory, the properties of a many-electron system can be determined by using functionals, i.e. functions of another function, which in this case is the spatially dependent electron density.[1, 2] Hence the name density functional theory comes from the use of functionals of the electron density. DFT is among the most popular and versatile methods available in condensed-matter physics, computational physics, and computational chemistry. The success of DFT not only encompasses standard bulk materials but also complex molecules.

The main idea of DFT is to describe the ground state of an interacting system of fermions as a functional of the electronic density instead of many body

wavefunction. For such a system satisfies the rule of conservation of the number of electrons, behavior of the entire many-body system becomes dependent only on three spatial coordinates. From computational point of view, DFT allows researchers to deal with much larger and complex systems by using less computational sources.

## 2.2 Exchange-Correlation Potentials

While DFT in principle gives a good description of ground state properties, the axact form of exchange-correlation potential that describes all electron-electron interactions is not known. Therefore the effects of Pauli principle and the Coulomb potential on electron-electron interactions have to be approximated by the appropriate functionals in terms of the electron density. However, there are well-established approximations to the exchange-correlation potential exist which permit the calculation of certain physical quantities quite accurately: Local Density Approximation and the Generalized Gradient Approximation.

### 2.2.1 Local Density Approximation

Local density approximation (LDA) is one of the most widely used approximation to exchange- correlation potential. LDA assumes that exchange-correlation energy is equal to that of uniformly distributed electron gas at the same coordinate and the functional is a function of coordinates. Thus the inhomogeneous system of a molecular or crystal structure is approximated by using local density of the homogen electron gas.

For a spin unpolarized system, exchange-correlation energy can be written as

$$E_{xc}^{LDA}(\rho) = \int \rho(r)[\epsilon_x + \epsilon_c]dr \tag{2.1}$$

where $\rho(r)$, $\epsilon_x$ and $\epsilon_c$ are the ground state charge density, exchange energy and

correlation energy, respectively. A similar local density functional for spin polarized system, namely local spin density approximation (LSDA), can be written by using spin dependent electron density $\rho(r) = \rho^{\downarrow}(r) + \rho^{\uparrow}(r)$.

Lots of the ground state properties such as lattice constant, stiffness, bulk moduli, band structure well approximated LDA. However, while the potentials of finite systems approximated by LDA decay exponentially, in the real systems this decrease is much slower in a Coulombic manner.

### 2.2.2 Generalized Gradient Approximation

For the structures having rapidly changing charge densities, the exchange-correlation energy deviates significantly from the uniform result and LDA approximation may become poor. Beyond the LDA, Generalized gradient approximation (GGA) takes into account the gradient and higher order spatial derivatives of the electron density to correct for this deviation. Exchange-correlation energy approximated by GGA is in the form of

$$E_{xc}^{GGA}(\rho) = \int \rho(r)[\epsilon_x(\rho(r), \vec{\nabla}\rho(r)) + \epsilon_c(\rho(r), \vec{\nabla}\rho(r))]dr \tag{2.2}$$

where $\rho(r)$, $\epsilon_x(\rho(r), \vec{\nabla}\rho(r))$ and $\epsilon_c(\rho(r), \vec{\nabla}\rho(r))$ are the ground state charge density, exchange energy and correlation energy, respectively.

## 2.3 Calculation of Phonon Spectra

In addition to ground state propoerties it is also possible to calculate a lot of excited state properties of the structures within the framework of DFT. Determination of vibrational dispersion spectra of the structures is quite important for the characterization of predicted novel materials. Especially the calculation of almost perfect phonon spectra is possible within the reach of DFT.

As a starting point of phonon calculations performed within the framework of DFT, the Hellmann- Feynman[3] theorem, that relates the derivatives of total energy and Hamiltonian by a simple parameter, has a great importance. Since the ground state evolves as a function of ionic motions, the total energy of a structure can be seen as a function of atomic positions. When the parameter in the Hellman-Feynman theorem is choosen to be the spatial coordinate of the nuclei, it is possible to calculate all the forces in the structure. Fundamental quantities can be formalized as follows

energy

$$E = E_{tot}(R_i) \tag{2.3}$$

force on a nuclei locating at $R_i$

$$F_i = \frac{dE}{dR_i} \tag{2.4}$$

force constants

$$C_{ij} = \frac{dF}{dR_j} \tag{2.5}$$

By using the vibrational properties obtained from the simple formulation presented above it is also possible to calculate the dielectric constants, effective charges, electron-phonon interactions, specific heat and entropy of the systems. In this thesis, there are two main computational method used for the calculation of phonon spectra: small displacement method and density functional perturbation theory.

### 2.3.1 Small Displacement Method

For the calculation of the frequencies of phonons for any arbitrary choice of q-vector in the Brillouin zone small displacement method (SDM) provides a very simple and quite useful model by treating the crystalline and molecular structures as system of balls connected by springs. Propagation of lattice vibration waves through the structure can start with an initial perturbation on the atoms and is mediated by the electrons. Description of the atomic vibrations of a crystal or a molecule is simply based on a potential energy term expanded around the atomic equilibrium positions. As long as the atoms remain close to their equilibrium positions, energy of the system can be described by using harmonic approximation as follows

$$U_{harm} = E_{ground} + \frac{1}{2}\sum \Phi_{ls\alpha,l't\beta} R_{ls\alpha} R_{l't\beta} \tag{2.6}$$

where $\Phi_{ls\alpha,l't\beta}$ is the force constant matrix, $R_{ls\alpha}$ is the displacement of $s$ atom in unitcell $l$, and $\alpha$ and $\beta$ are cartesian coordinates. Therefore the force constant matrix that relates the force on each atomic site $F_{ls\alpha}$ to atomic displacements at neighboring sites $R_{l't\beta}$ as

$$F_{ls\alpha} = \frac{dU_{harm}}{dR_{ls\alpha}} = -\sum \Phi_{ls\alpha,l't\beta} R_{l't\beta} \tag{2.7}$$

and the force constant matrix is simply given as

$$\Phi_{ls\alpha,l't\beta} = \frac{d^2U_{harm}}{dR_{ls\alpha}dR_{l't\beta}} \tag{2.8}$$

It is seen that forces and displacements are linearly dependent eachother as long as the atomic displacements are small enough.

From the viewpoint of computational methodology, it is seen that the atomic displacements kept in the range of 0.01-0.04 Å give reasonably good results. Therefore the characteristics of the vibrational motion at each atomic site is

determined by finding the eigenvalues of the dynamical matrix whose elements are $F_{ls\alpha}$

$$D = \frac{1}{\sqrt{m_s m_t}} \sum \Phi_{ls\alpha,l't\beta} R_{l't\beta} e^{iq\cdot T} \tag{2.9}$$

It appears that the force constant matrix can also be used to determination of the elements of dynamical matrix for any q-vector in the Brillouin zone. Since calculations are performed for supercells by using periodic boundary conditions, the supercells must be choosen large enough to provide that the forces take negligible values at the boundary of the cell. For most of the metals, due to the large screening provided by electrons this convergence condition is satisfied for smaller supercells.

In the framework of small displacement method, phonon frequencies of a given structure can be observed via construction of the force constant matrix upon small displacement of the atoms in the periodically repeating supercells.[4] From the phonon frequencies in crystals it also possible to determine various thermodynamic quantities; Helmholtz free energy, entropy, specific heat and internal energy of the harmonic crystal.

### 2.3.2 Density Functional Perturbation Method

For the calculation of phonon spectra of ionic compounds the convergence can be problematic due to the motions of charged atoms. Since the displacement of charges creates dipoles that interacts with long range forces, force on the neighboring atoms decrease as $r^{-3}$. Hence, the long range polarization fields are artificially suppressed in supercells resulting in a vanishing LO- TO splitting. This is especially due to the wrong LO frequencies. Such a slow decrease requires very extended supercells for the treatment of ionic compounds within small displacement method.

Especially for the ionic crystals density functional perturbation theory

(DFPT) is quite advantegous compared to SDM. Due to the presence of macroscopic electric field generated by dipols, longitudinal and transversal optical phonon branches are splitted at gamma point and therefore the so called LO-TO splitting can be included in DFPT calculations.

A net dipol moment in the ionic compound can appear for the small values wave vector $q$ i.e. at the vicinity of $\Gamma$ point. Accordingly the non-analytical part of the dynamical matrix in the limit of small $q$ can be written as follows

$$D = \frac{4\pi e^2}{\Omega\sqrt{m_s m_t}} \frac{(q \cdot Z_s^*)(q \cdot Z_t^*)}{q \cdot \epsilon^\infty \cdot q} \tag{2.10}$$

where $Z^*$ is the Born effective charge tensor and $\epsilon^\infty$ is the high frequency static dielectric tensor.

Calculation of phonon spectra of crystal structures in the framework of DFPT is also provide an elegant strategy. A DFPT calculation starts from the ground state results obtained from the primitive unit cell of given material and the problem of dealing with large supercells is avoided. The response to arbitrary and infinitesimally small displacements of the atoms in the unitcell and the changes in the ionic potential is calculated for each $q$ by means of perturbation theory.[5] As a result of Hellmann-Feynman theorem perturbations yielding linear order deviations in the electron density also cause a second order perturbation in total energy. Therefore the linear order variation in the electron density can be calculated using only unperturbed wavefunctions of the ground state crystal. For the case of linear perturbation on charge density caused by phonon motion, force on each atom can be calculated for any wavevector $q$ without constructing extended supercells.

## 2.4 Graphene: Computational Analysis

Last two decades, nanoscience and emerging nanotechnologies have been dominated by honeycomb structured carbon based materials in different dimensionality, such as fullerenes, single and multi walled carbon nanotubes, graphene and its ribbons. In particular, graphene, a two dimensional (2D) honeycomb structure of carbon, has been an active field of research.[6] Because of unique symmetry, electron and hole bands of graphene show linear band crossing at the Fermi level[7] resulting in a massless Dirac Fermion like behavior of charge carriers.

The fabrication of graphene sheets[6] and observation of their unusual properties such as a half-integer quantum-Hall effect have attracted much interest in electronic transport properties of this type of two dimensional graphitic materials. Observed gapless energy spectrum and high mobility electron transport[8, 9, 10] are the most remarkable features of graphene. It was shown by tight-binding calculations considering the $\pi$ bands that in the electronic energy dispersion of graphene, energy is linearly dependent on the wave vector around the Fermi level[7] which makes it a unique material.

As a result, Klein paradox, an interesting result of quantum electrodynamics was expected to be observed in graphene.[6, 8] Moreover, it was shown that half-integer quantization of Hall conductance[8, 9, 10] can be observed in graphene. Unusual electronic and magnetic properties of graphene, such as high carrier mobility, ambipolar effect, have promised variety of applications. In addition to some early works on crystalline order in planar structures, possibility of very large one-atom-thick two dimensional (2D) crystals with intrinsic ripples is reported theoretically[8, 11] and experimentally.[8, 9] Not only extended 2D graphene sheets but also quasi-one-dimensional graphene ribbons with armchair or zigzag edges have shown unusual electronic,[12, 13] magnetic[14, 15] and quantum transport properties.[16, 17, 18, 19]

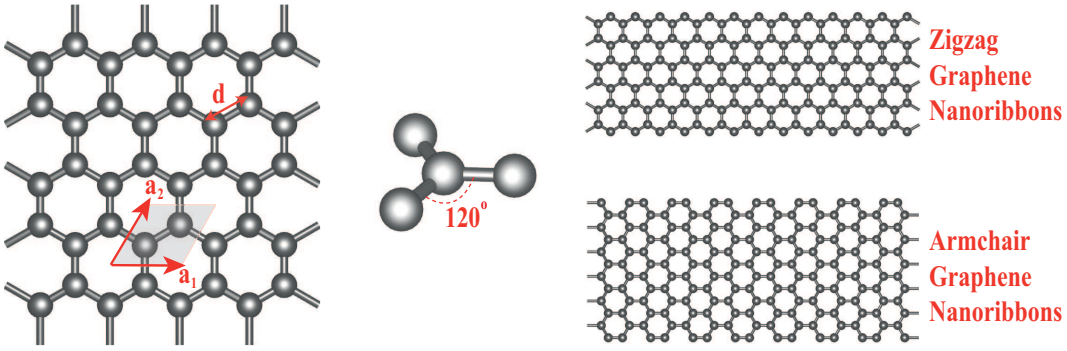


Figure 2.1: (a) Top view of honeycomb structure of graphene. Bravais lattice vectors for both structure are given with $|\vec{a_1}| = |\vec{a_2}| = a$. Hexagonal unitcell including two carbon atoms is delineated by dashed area. (b) Side view for the $sp^2$ coordinated carbon atoms of graphene. (c) Atomic configuration of zigzag and armchair graphene nanoribbons.

### 2.4.1 Atomic Structure

Graphene has a 2D hexagonal lattice in which C atoms are arranged to form a planar (PL) honeycomb structure as shown in Fig.2.1. Accordingly, it has a six fold rotation axis, $C_6$ at the center of the hexagon, which is perpendicular to the atomic plane. Hexagonal lattice has a two-atom basis in the primitive unit cell, corresponding to A- and B-sublattices. That is three alternating atoms of each hexagon belong to one of the two sublattices. In graphene planar geometry is assured by the formation of strong $\pi$-bonding between two nearest neighbor $p_z$-orbitals perpendicular to the graphene plane. The resulting $\pi$- and $\pi^*$-bands determine also relevant electronic properties. In addition, there are strong yet flexible, covalent $\sigma$-bonds derived from the planar hybrid $sp^2$ orbitals between adjacent C atoms. Nearest C atoms are separated by 1.42 Å and the magnitude of the hexagonal Bravais lattice vector is 2.46 Å. Briefly, the planar $sp^2$ hybridization and perpendicular $p_z$ orbitals underlie planar geometry, unusual mechanical strength and electronic structure of graphene.

However, in two of our studies,[20, 21] it is revealed that graphene-like two dimensional honeycomb structure of Group IV elements and their binary compounds, as well as the compounds of Group III-V elements can also be possible

stable. We find that all the binary compounds containing one of the first row elements, B, C or N have planar stable structures. On the other hand, in the honeycomb structures of Si, Ge and other binary compounds the alternating atoms of hexagons are buckled, since the stability is maintained by puckering.

### 2.4.2 Electronic Structure

Propagation of electron waves through the honeycomb lattice attributes exceptional features to graphene.[6, 8] Conduction of electrons within one-atom-thick layer with minute scattering makes the observation of quantum effects possible even at room temperature.[10] In graphene Dirac fermions have a high Fermi velocity, $v_F = c/300$. Due to its high carrier mobility, graphene based ballistic transistors operating at room temperature have already been fabricated. In addition to these unusual electronic properties of graphene, the observation of anomalous quantum Hall effect and the possibility of Klein paradox are features, which attract the interest of researchers. Electronic properties of graphene and graphene-based structures have recently been reviewed.[11] Experimental investigations have reported the observation of half-integer quantum Hall effect for carriers in graphene and possible magneto-electronic device applications.[9] Most of the unique properties of graphene are related to its monolayer lattice structure, linearly crossed $\pi$ bands at Fermi level with electron-hole symmetry.

Here, we start with a brief discussion of hexagonal symmetry and apply simple tight binding model of $\pi$-orbitals to reveal the effect of lattice symmetry on the band crossing.[7] Graphene has the space group P6/mmm and point group symmetry $D_{6h}$. At the-$\Gamma$ point, the group of the wave vector is isomorphic to the point group $D_{6h}$. However, irreducible representation of the wave vector point group turns into $D_{2h}$ and $D_{3h}$ at high symmetry points $M$ and $K$ (or $K'$), respectively. It was shown that the tight binding Hamiltonian with nearest neighbor hopping parameter, $t = 2.7$ eV

$$H = \sum_i \epsilon_i c_i^\dagger c_i + t \sum_{i,j} (c_i^\dagger c_j + H.c). \tag{2.11}$$

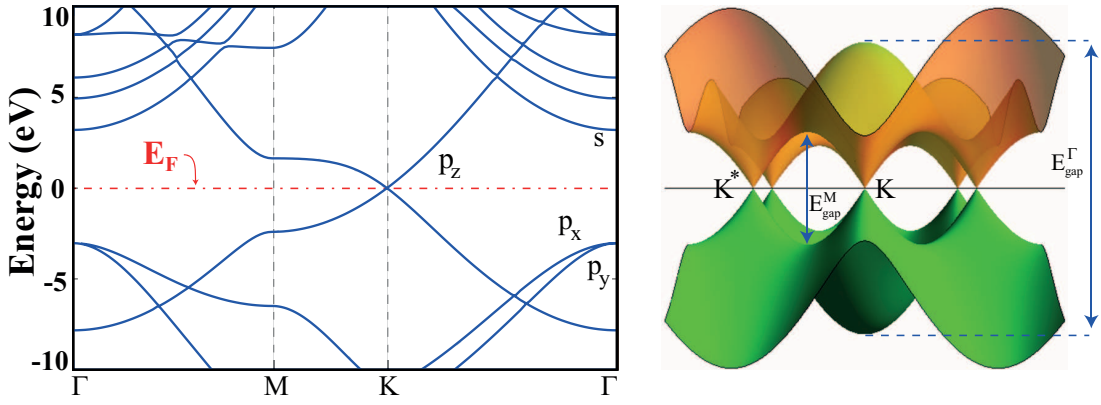


Figure 2.2: (a) Electronic band structure of graphene obtained by first principles method. High symmetry points and the orbital character of the bands are delineated. (b) Three dimensional band structure, obtained by tight-binding approximation, for valence and conduction bands and the Dirac points locating at the K symmetry points. Nearest neighbor hopping parameter is taken to be 2.7 eV.

well approximates the $\pi$-bands of perfect graphene.[7] Here $c_i^\dagger$ ($c_i$) is the creation (annihilation) operator of a $\pi$ electron at the lattice site $i$. The first term is the on-site energy of each carbon atom and equals to energy of the $2p_z$ orbital. Energy eigenvalues of graphene and other two hypothetical crystal having square and hexagonal lattices with single atom in the cell are calculated and the contour plots their energy band gap in BZ are shown in Fig.2.2. For graphene, energy dispersion is linear at the vicinity of the $K$- symmetry (Dirac) points and the Fermi velocity, which is linearly dependent to nearest neighbor interaction parameter, can be given by the expression $v_F = 3td/2\hbar$.[11]

Recently, we showed that the honeycomb structure with linear band crossings at Dirac points is also common to Si and Ge.[21, 20] and binary compounds between different Group IV elements and Group III-V elements,[20] which are stable in either infinite periodic form or in finite size, are presented in Fig. **??**. In these hexagonal lattice structures (PL or LB) relevant electronic energy bands around the Fermi level are derived from $\pi$ and $\pi^*$-bands. In elemental honeycomb

structures, such as graphene, Si and Ge, these bands have linear crossings at two in-equivalent $K$- and $K'$-points of BZ, called Dirac points and hence they are semimetallic. Because of their linear dispersion of $E(\mathbf{k})$, the charge carriers near the Dirac points behave as massless Dirac Fermions. By fitting the $\pi$-and $\pi^*$-bands at $\mathbf{k} = \mathbf{K} + \mathbf{q}$ to the expression,

$$E(\mathbf{q}) \simeq \mathbf{v_F}\hbar|\mathbf{q}| + \mathbf{O(q^2)} \tag{2.12}$$

and neglecting the second order terms with respect to $q^2$, one can estimate the Fermi velocity for both Si and Ge as $v_F \sim 10^6$ m/s. We note that $v_F$ calculated for 2D LB honeycomb structures of Si and Ge are rather high and close to that calculated for graphene using the tight-binding bands. It is also worth noting that because of the electron-hole symmetry at K- and $K'$-points of BZ, 2D LB Si and Ge are ambipolar for E($\mathbf{q}$)= $E_F \pm \delta E$, $\delta E$ being small. Among these, Si and Ge in honeycomb structure are semimetal and have linear band crossing at the Fermi level which attributes massless Fermion character to charge carriers as in graphene.

### 2.4.3 Transport Properties

In recent experimental studies graphene nanoribbons (GNRs) with narrow widths (10-70 nm) have been realized.[22] Li *et al* report producing ultra narrow ribbons with widths down to a few nanometers.[23] In addition to high carrier mobilities that are higher than those in commercial silicon wafers, existence of width-dependent energy band gaps makes the graphene nanoribbons a potentially useful structure for various applications. The width dependence of the band gap and transport properties in quasi-one dimensional narrow GNRs have been studied theoretically.[24, 25, 26, 27, 28, 12] Graphene nanoribbons having $r$ zigzag rows ($r$-ZGNRs) are predicted as semiconductors having a narrowing band gap with the increasing width of the ribbon. Armchair-edged ribbons (AGNRs) are also semiconducting with direct band gaps.[24] DFT calculations predict a high density of states around the valence and conduction band edges of ZGNRs, which derive

from the states that are localized at the edges of the ribbon, and lead to non-zero magnetic moments on the carbon atoms. Due to the edge effects, graphene ribbons show different one dimensional transport properties from those of carbon nanotubes. In particular ZGNRs, known to have large spin polarizations at the opposite edges of the ribbon, may be utilized to create spin-dependent effects such as spin polarized currents without the need of ferromagnetic electrodes or other magnetic entities.

Modification of electronic structure by impurities, adatoms and external fields is another potential of graphene and graphitic structures for applications in nanoelectronics. Effects on electronic properties and magnetic behavior of graphene by the adsorption of foreign atoms has been considered in some previous works.[16, 17, 29] Sizeable gap opening by hydrogen adsorption to Stone-Wales defect sites of graphene has been reported.[18] In the case of substitutional boron atom many of the electronic properties have been studied and it is suggested that GNRs may be used as spin filter devices.[30]

In our two different studies,[19, 31] the characteristics of quantum transport properties of electrons flowing through the rectangular and triangular shaped graphene nanoflakes were investigated. The spin-dependent transport properties of the graphene flake are calculated based on non-equilibrium Green's function formalism as implemented in package AtomistixToolKit. Ballistic conductance spectrum of the flake is given within Landauer- Büttiker formalism as

$$G(E) = G_0 \sum_{\sigma} T_{\sigma}(E) \tag{2.13}$$

where $G_0 = e^2/h$ is the conductance quantum and $T_\sigma$ ($\sigma$ = up, down) are the spin-dependent transmission spectra. For each spin state $\sigma$ the transmission probabilities are calculated as

$$T_{\sigma}(E) = \mathrm{Tr}[\Gamma_L G^r \Gamma_R G^a]_{\sigma}, \tag{2.14}$$

where $G^r$ and $G^a$ are the retarded and advanced Green's functions, $\Gamma_L$ and $\Gamma_R$

are the contact broadening functions associated with the left and right electrodes, respectively. The broadening functions are anti-Hermitian components of the self-energy terms of the contacts, $\Sigma_L$ and $\Sigma_R$, which depend on the electrode's surface Green's function and the contact-molecule (graphene flake) bonding:

$$\Gamma_{L,R} = i(\Sigma_{L,R} - \Sigma_{L,R}^{\dagger})/2 \tag{2.15}$$

The spatially-separated spin-states of the graphene flake are anticipated to break the spin symmetry in these conductance calculations when contacts to the electrodes are not symmetric at the armchair edges.

#### 2.4.3.1 Graphene Nanoribbons

At the first stages of this thesis, quantum transport properties of narrow graphene flakes and their functionalization with vanadium atoms were studied. Rectangular graphene flakes are stable, having geometric and electronic structures quite similar to that of extended graphene nanoribbons as shown in Fig.2.3(a). It was shown that a spin- polarized current can be produced by pure, hydrogenated rectangular graphene flakes by exploiting the spatially-separated edge states of the flake using asymmetric, non-magnetic contacts. Functionalization of the graphene flake with magnetic adatoms such as vanadium also leads to spin-polarized currents even with symmetric contacts as shown in Fig.2.3(b). Sharp discontinuities in the transmission spectra presented in Fig.2.3(c) arise from the Fano resonances of localized states in the flake.

#### 2.4.3.2 Triangular Graphene Flakes

Quantum transport properties of triangular graphene flakes with zigzag edges by using first principles calculations. Triangular graphene flakes shown in Fig. 2.4(a-c) have large magnetic moments which vary with the number of hydrogen atoms terminating its edge atoms and scale with its size. Electronic transmission and current-voltage characteristics of these flakes, when contacted with metallic

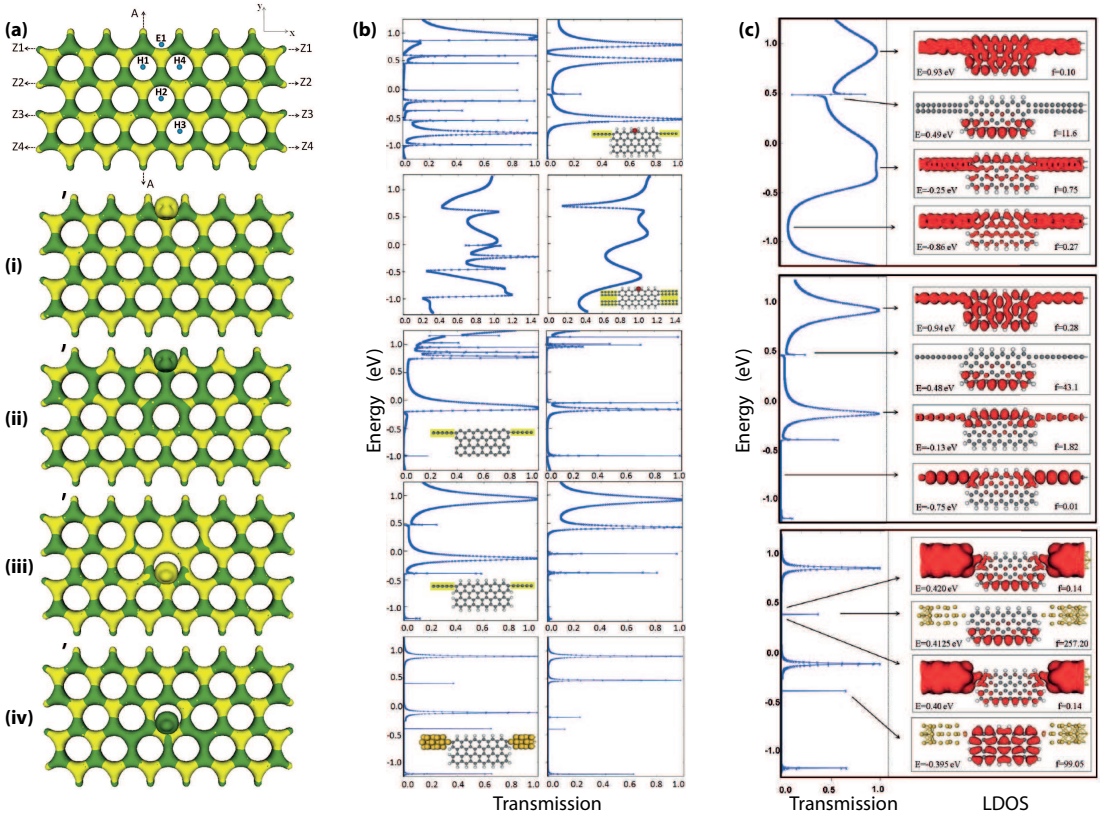


Figure 2.3: (Color online) Geometry and spin-dependent charge density of the graphene flake cut from 4-ZGNR. The edges are saturated with hydrogen atoms. Green (dark) and yellow (light) regions denote the local majority spin-type of the charge density. Possible adsorption sites of adatoms are also labelled. The lowest energy configuration for a single vanadium atom is shown in (i). (b) Spin-dependent transmission spectra for various cases of graphene fragment. Fermi level is set to zero. (c) Local density of states (LDOS) isosurfaces calculated for particular energy values of the up-spin transmission spectra of partially contacted graphene flake.

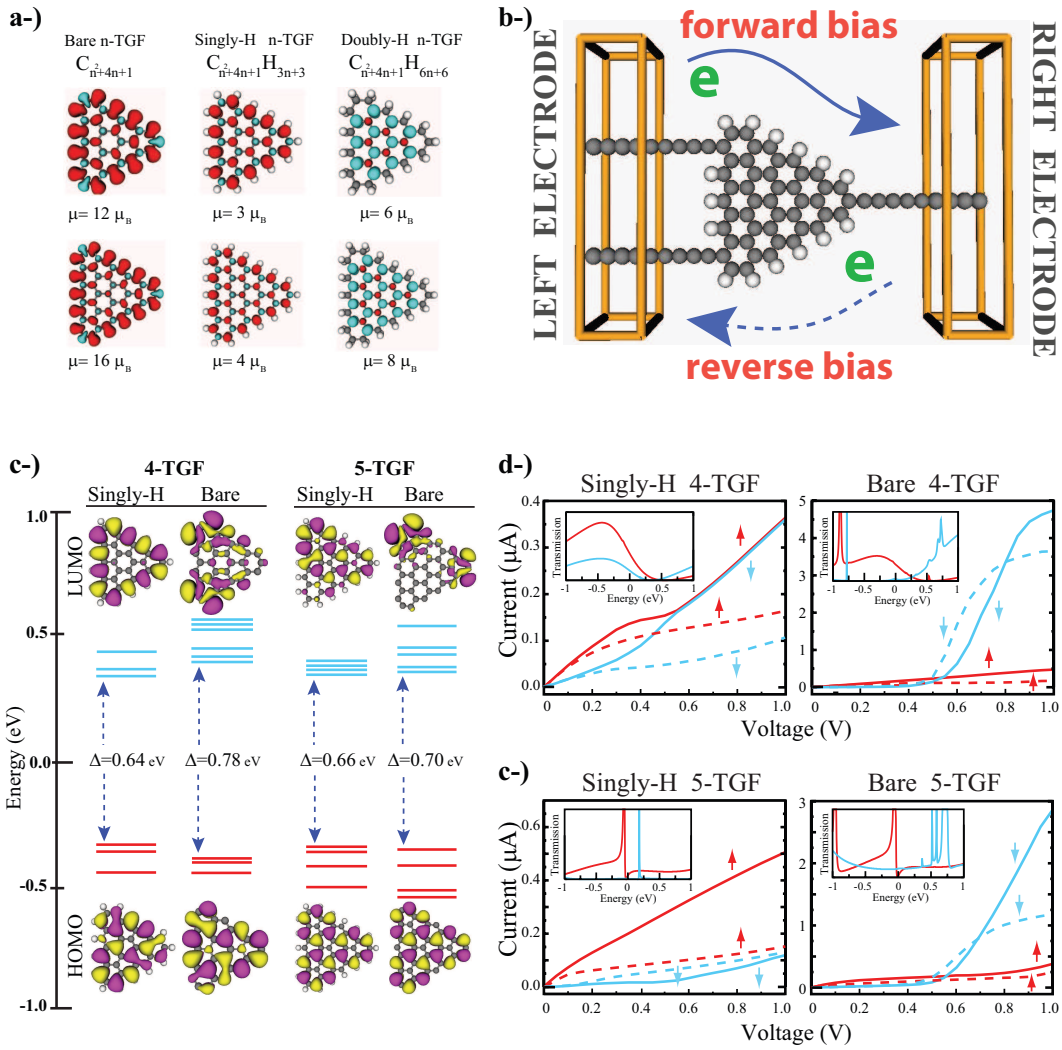


Figure 2.4: (Color online) Atomic structure and isosurface of charge density difference of spin-up (↑) and spin-down (↓) states for 4-(upper row) and 5-triangle (lower row) graphene flakes: Bare, singly- and doubly-hydrogenated edges. Calculated net magnetic moments of the flakes are given in terms of Bohr magneton ($\mu_B$). Difference charge density of spin-up and spin-down states is shown by red (dark) and blue (light) isosurface, respectively. Electrode-device geometry and convention for forward and reverse bias applied to triangular graphene flakes (TGFs).(a) Energy level spectra within ±1 eV range of Fermi level ($E_F$), the HOMO-LUMO gap ($\Delta$) and isosurface of HOMO and LUMO orbitals. (b-c) Calculated I-V curves for hydrogenated and bare triangular graphene flakes (TGFs). Results of 4-TGF and 5-TGF are presented, respectively. Spin-up (↑) and spin-down (↓) currents are shown by red (dark) and blue (light) lines, respectively. Solid and dashed lines denote forward and reverse bias calculations, respectively. Transmission curves of spin-up and spin-down under zero bias are also shown by insets. Transmission spectra of singly-H and bare TGFs are plotted up to maximum value of 0.03 and 0.4, respectively. Fermi levels are set to zero.

electrodes, reveal spin valve and remarkable rectification features as shown in Fig. 2.4(e). The transition from ferromagnetic to antiferromagnetic state under bias voltage can, however, terminate the spin polarizing effects for specific flakes. Geometry and size dependent transport properties of graphene flakes may be crucial for spintronic nanodevice applications.

### 2.4.4 Vibrational Spectra

Analysis of phonon modes provides a more reliable test for a structure optimized by using ab initio methods. If there is an instability related with a phonon mode with $\mathbf{k}$ in BZ, the square of frequency, $\Omega(\mathbf{k})$ obtained from the dynamical matrix becomes negative yielding imaginary frequency. Then this particular mode cannot generate restoring force to execute lattice vibration and hence the system is vulnerable to go away from its original configuration. Here results of SDM phonon calculations shown in Fig. 2.5 are performed by taking into account the interactions in (7x7x1) large supercells consisting of 98 atoms. However for the DFPT calculation use of single unitcell is enough.

Graphene honeycomb lattice have six different phonon branches: three acoustical (A) and three optical (O). It is seen that around 1600 $cm^{-1}$, LO and TO eigenmodes are degenerate at $\Gamma$ point. Since structure have a covalent character both the SDM and DFPT finds degeneracy of LO and TO at gamma. However, among the three acoustical modes, in-plane TA and LA eigenmodes have linear dispersion around the $\Gamma$ point. As it is mentioned in earlier works[32] on 2D structures, out-of-plane ZA eigenmode have quadratic phonon dispersion in the vicinity of $\Gamma$-point. Here, the calculated value for out-of-plane optical eigenmode ZO is around 900 $cm^{-1}$. Existence of strong electron-phonon coupling in TO eigenmode at the $K$-point and $E_{2g}$ modes at $\Gamma$ -point is the reason of the Kohn anomaly at these points. Therefore, scattering by phonon with the energies that corresponds to these modes can cause noticeable decrease in transmission spectrum.[32] It is well known that as $\mathbf{k}\rightarrow 0$ phonon dispersions of LA and TA branches are linear, but that of ZA branch is quadratic since transversal forces decay rapidly. Among these, the LA and TA phonon branches are heat carrying

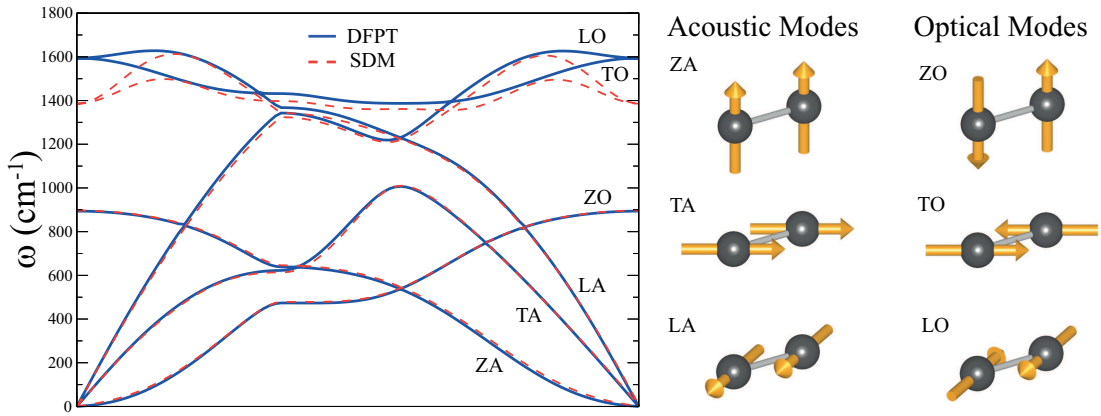


Figure 2.5: Phonon dispersion of the graphene. The results of SDM nad DFPT are presented by solid/blue and dashed/red lines. Atomic motions at the gamma symmetry point are also delineated.

modes. However, it was shown that bending branch ZA makes negligible contribution to thermal conductivity.[33] Calculated phonon dispersion of graphene shown in Fig. 2.5 is in good agreement with previous LDA results[32] and also with reported experimental data.[34, 35]

# Chapter 3

# Making Graphene Magnetic

In this part of the thesis, using first principles calculations, we show that each hydrogen vacancy created at graphane surface results in a local unpaired spin. For domains of hydrogen vacancies the situation is, however complex and depends on the size and geometry of domains, as well as whether the domains are single- or double-sided. In single-sided domains, hydrogen atoms at the other side are relocated to pair the spins of adjacent carbon atoms by forming $\pi$-bonds. Owing to the different characters of exchange coupling in different ranges and interplay between unpaired spin and the binding geometry of hydrogen, vacancy domains can attain sizable net magnetic moments. The results pertaining to this chapter are published in Ref.[[36]] and figures are reproduced with permission of the publisher.

## 3.1 Motivation

Graphene[6], a truly two-dimensional (2D) crystal of honeycomb structure, has sparked considerable interest not only because of its charge carriers behaving like massless Dirac fermions[8, 9, 37], but also the unusual magnetic properties displayed by its flakes and nanoribbons[23, 38, 39, 40, 19]. In addition to numerous experimental and theoretical studies on the physical properties of

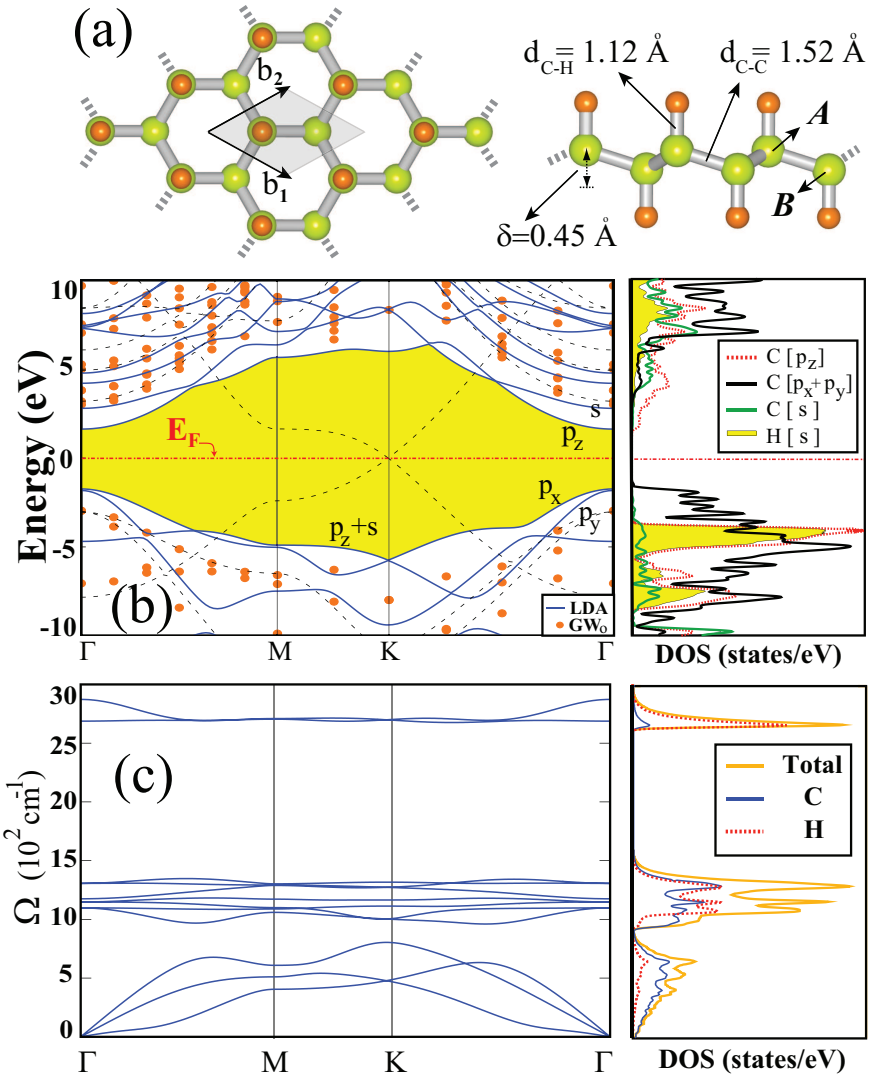


Figure 3.1: (Color online) (a) Top and side views of atomic structure showing of graphane primitive unit cell with Bravais lattice vectors $\mathbf{b}_1$ and $\mathbf{b}_2$ and buckling of alternating carbon atoms, A and B, in honeycomb structure $\delta$, bond lengths $d_{C-C}$ and $d_{C-H}$ optimized using LDA. Large green (light) and small orange (dark) balls indicate C and H atoms, respectively. (b) Energy band structure is calculated by using LDA and corrected using $GW_0$ (shown by blue lines and orange dots). For graphene, linear band crossing at Dirac point is shown by dashed grey lines. (c) Calculated phonon bands and density of states DOS projected to C and H atoms.

graphene, efforts have been also devoted to synthesize various types of derivatives of graphene. More recently, a 2D hydrocarbon material in the family of honeycomb structure, namely *graphane* is synthesized[41]. Interesting properties such as reversible hydrogenation-dehydrogenation with changing temperature[41], the electronic structure with a wide band gap[42] have been revealed soon after its synthesis. In this part of my thesis, we reveal that graphane can be magnetized by dehydrogenation of domains on its surfaces. Large magnetic moments can be attained in a small domain on the graphane sheet, depending on whether the defect region is one-sided or two-sided. Our predictions are obtained from the state-of-the-art spin polarized first-principles plane-wave calculations[43, 44, 45] within the LDA[46, 47] noncollinear calculations including spin-orbit interaction, using (11×11×1) supercells.

## 3.2 Graphane: Fully Hydrogenated Graphene

Graphane, in its chair conformation as illustrated in Fig. 3.1(a), is derived by the adsorption of a single hydrogen atom to each carbon atom alternating between the top ($A$) and bottom ($B$) side in the honeycomb structure. A charge of 0.1 electrons is transferred from H to C leaving behind positively charged H atoms on both sides of a double layer of negatively charged (-0.1 electrons) C atoms. Graphane having a 2D quadruple structure has the work function $\Phi$=4.97 eV, which is $\sim$ 0.2 eV larger than that of graphene. In contrast to semimetallic graphene, graphane is a semiconductor with a wide direct band gap of 3.42 eV calculated by LDA but corrected to be 5.97 eV with $GW_0$ self-energy method, as shown in Fig. 3.1(b). Doubly degenerate states at the $\Gamma$-point at the top of the valence band are derived from $2p_x$- and $2p_y$-orbitals of carbon atoms. The edge of the conduction band is composed mainly from C-$p_z$ orbitals. Calculated phonon bands all having positive frequencies confirm the stability of 2D graphane. High frequency vibration modes associated with C-H bonds are well separated from the rest of the spectrum, in Fig. 3.1(c).

## 3.3 Vacancy Formation on Graphane

The creation of a single H-vacancy at the hydrogen covered surfaces gives rise to the spin polarization in the non-magnetic perfect graphane. Desorption of a single H atom from graphane is an endothermic reaction with 4.79 eV energy. Various techniques, such as laser beam resonating with surface-hydrogen bond[48] and stripping with ionic vapor[49] can be used to create H-vacancy(ies). Upon desorption of a single hydrogen atom, local bonding through $sp^3$ hybrid orbital is retransformed into planar $sp^2$ and perpendicular $p_z$ ($\pi$) orbitals. At the vacancy site one unpaired electron accommodated by the dangling $p_z$ orbital contributes to the magnetization by one $\mu_B$ (i.e. Bohr magneton). The exchange interaction between two H-vacancies calculated in a (11x11x1) supercell is found to be non-magnetic for the first and second nearest neighbor distances due to spin pairings. Since the $\pi$-$\pi$ interaction vanishes for farther distances, antiferromagnetic (AFM) state between two H-vacancies for the third and fourth nearest neigbor distance is energetically favorable. The occurrence of long range spin interactions in carbon based structures was explained before by the superexchange[50] and magnetic tail interaction[51].

### 3.3.1 Single-sided Vacancy Domains

As for the islands of H-vacancies at the single (top) side of graphane, we consider various geometrical domains, where H atoms at their edges and inside are removed as seen in Fig.3.2. For a triangular domain specified as $\Delta_2^s$ at the top side, H atoms attached to three carbon atoms located at each edge are removed. Hydrogen atom which is normally adsorbed on the central C atom at the bottom side moves to the corner. Under these circumstances, spins of three hydrogen-free C atoms are antiferromagnetically ordered to yield a net magnetic moment of 1 $\mu_B$. Noncollinear calculations with spin-orbit interaction fix the directions of spins, which are tilted relative to the normal to the graphane plane. For $\Delta_4^s$, a triangular domain has ten H atoms removed from the top side of graphane. While part of six H atoms are attached to carbon atoms from bottom are relocated, remaining

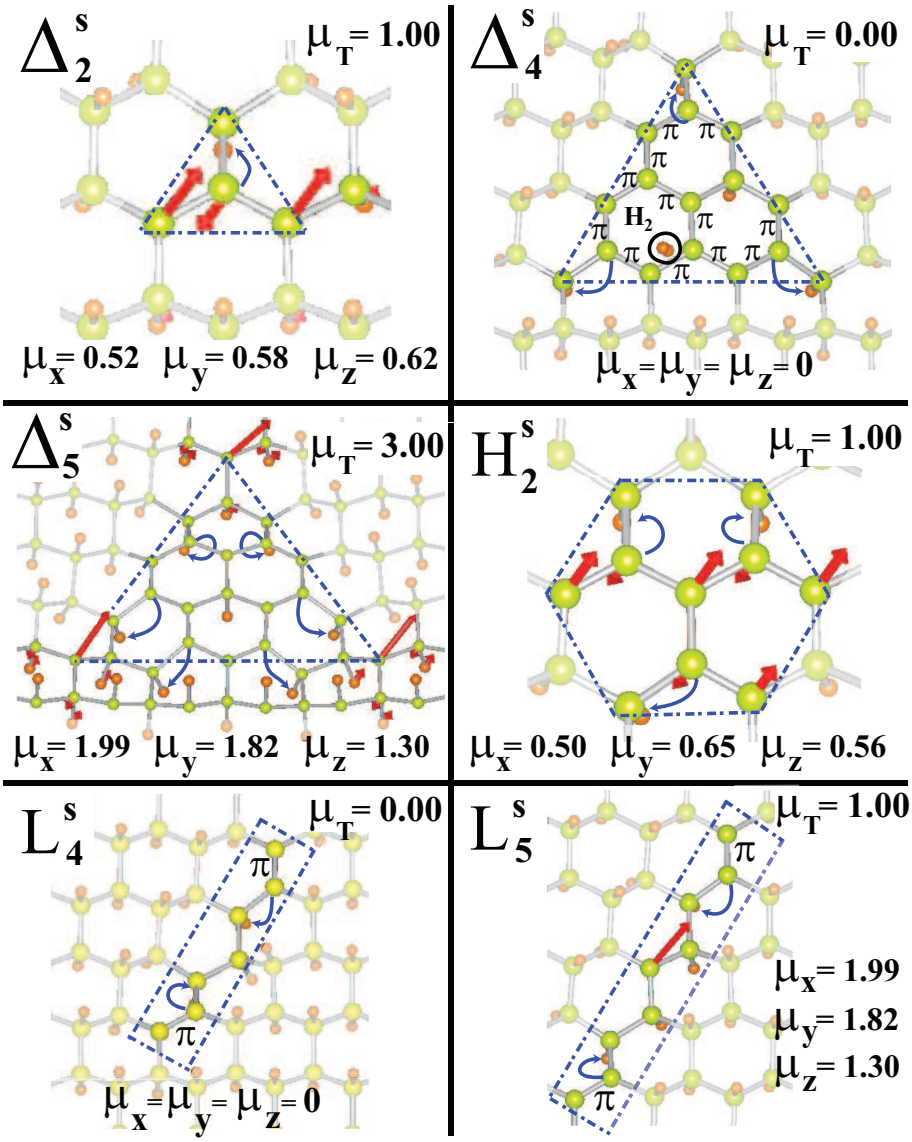


Figure 3.2: (Color online) Calculated magnetic state of various domains of single-sided H-vacancies, where all H atoms attached to C atoms from upper side in the unshaded region (delineated by dash-dotted lines) including edges, are removed. The triangles are specified by $\Delta_n^s$ with $n$ indicating the maximum number of C atoms at one edge and $s$ signifies the single-sided dehydrogenation. Similar symbols are used also for hexagonal, $H_2^s$ and lane $L_n^s$ ($n$ =4,5) domains. Total magnetic moment $\mu_T$ and its components $\mu_x$, $\mu_y$ and $\mu_z$ are given in units of the Bohr magneton $\mu_B$. Magnetic moments on C atoms are shown by red (black) arrows. Relocations of H atoms at the other side of graphane are shown by curly arrows. For the sake of clarity $\pi$-bonds formed after the relocation of bottom H atoms are indicated only for $\Delta_4^s$, $L_4^s$ and $L_5^s$ structures.

two H atoms are released by forming $H_2$ molecule. At the end spins are paired and the net magnetic moment of the domain becomes vanished. Generally, for a small single-sided domain, $\mu_T$=0 if $N_t$, the total number of H atoms stripped, is an even number so that adjacent $\pi$-orbitals form spin paired $\pi$-bonds. In this case, H atoms below the domain are relocated (without facing any energy barrier) to pair adjacent $\pi$-orbitals to form maximum number of $\pi$-bonds. At the end, a large buckled regions inside the domain tends to be flattened and reconstructed to make nonmagnetic graphene-like planar structure. In the case of $\Delta_5^s$, while spins are paired through the formation of $\pi$-bonding between two adjacent C atoms following the relocation H atoms at the bottom side, the unpaired spins at the corner atoms are aligned in the same direction to yield a net magnetic moment of $\mu_T$=3 $\mu_B$. The tendency to pair the spins of adjacent C atoms to form $\pi$-bonds are seen better in lane domains. Let us consider $L_4^s$ and $L_5^s$ in Fig.3.2. Because of relocation of H atoms at the bottom side, two pairs of nearest neighbor C atoms form $\pi$-bonds and hence pair their spins. At the end, $L_4^s$ has $\mu_T$=0. For $L_5^s$ having odd number of H-vacancy, while two pairs of C atoms are bound by two $\pi$-bonds, C atom at the center has an unpaired spin and attains $\mu_T$=1 $\mu_B$. In a similar manner, the hexagonal domain $H_2^s$ has total of seven C atoms at its center and corners, all H atoms stripped from top side. At the bottom side, H atoms are relocated and hence the spins of adjacent C atoms are paired to result in a total net magnetic moment of $\mu$=1 $\mu_B$.

### 3.3.2 Double-sided Vacancy Domains

We next show in Fig.3.3 that the magnetic moment of graphane can be tuned by changing the size and geometry of a given double-sided H-vacancy domain. In this case the situation is not complex and allows us to figure out the magnetic moment of the entire structure easily. Based on noncollinear calculations including the spin-orbit coupling, the direction of the unpaired spins on the $A$-type C atoms freed from H atoms is found to be opposite to that of the spins of $B$-type C atoms. However, instead of AFM spin ordering, lowest energy state of lane defects consisting of even number of C atoms is NM due to the entirely paired $p_z$ orbitals.

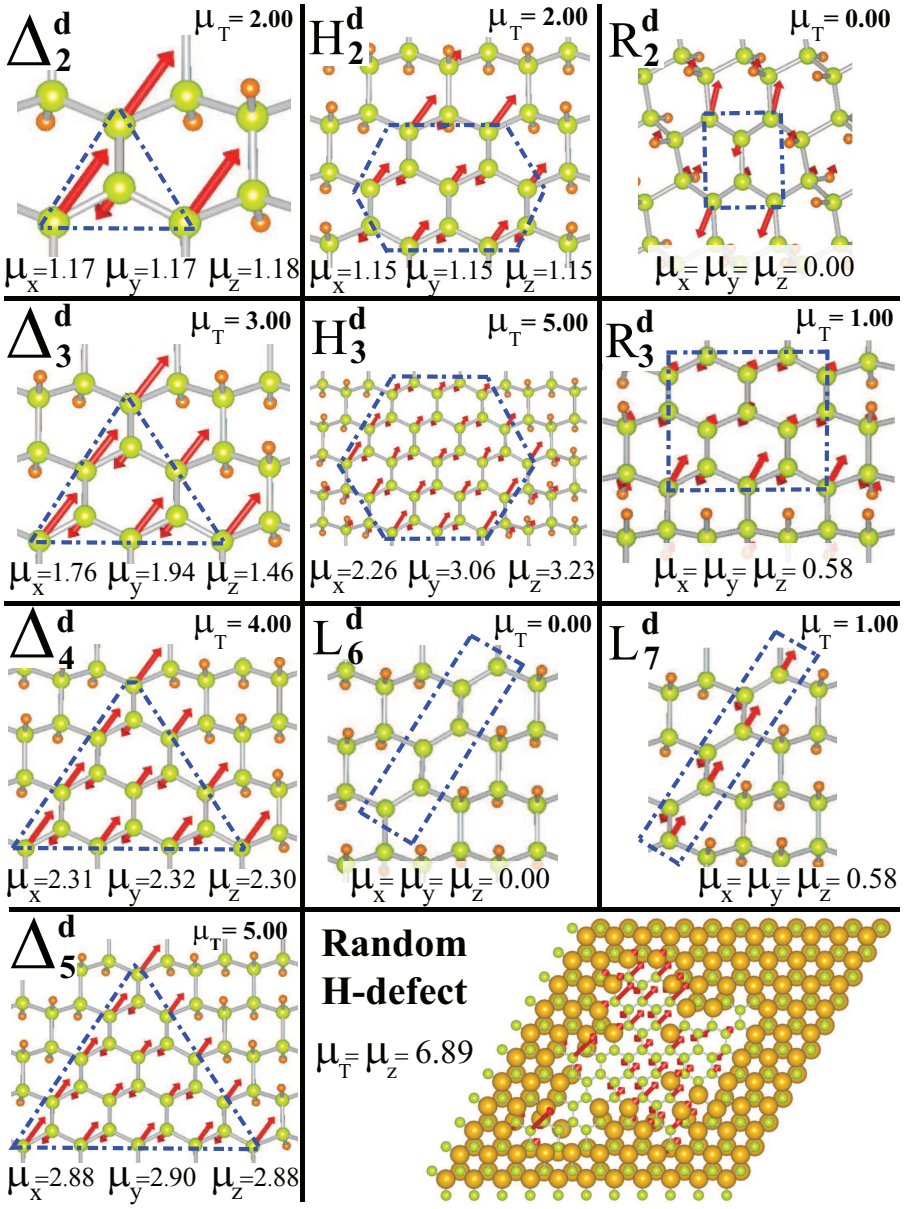


Figure 3.3: (Color online) Net magnetic moments in Bohr magneton within the triangular $\Delta_n^d$, hexagonal $H_n^d$, rectangular $R_n^d$ and lane $L_n^d$ domains, which are delineated by dash-dotted lines and have $n$ carbon atoms at their edges. Here $d$ signifies the double-sided dehydrogenation. Random shaped domain including both one and two-sided H-vacancy parts is also illustrated.

Also, large double-sided domains including lane defects with equal number of $A$- and $B$-type carbon atoms are found to be NM. The resulting net magnetic moment of a double-sided H-vacancy domains can be given by $\mu_T = (N_t - N_b)\mu_B$, where $N_t$ and $N_b$ denote the number of stripped H atoms from the top and bottom sides, respectively. Accordingly, the net magnetic moment induced in $\Delta_2^d$, $\Delta_3^d$, $\Delta_4^d$ and $\Delta_5^d$ domains are 2, 3, 4 and 5 the $\mu_B$ respectively. The same argument can be applied to rectangular $R_n^d$, hexagonal $H_n^d$ and lane $L_n^d$ domains. Even the magnetic moment of a domain having arbitrary shape including various single-sided and double-sided H-vacancy parts, as indicated in Fig.3.3, can be retrieved by the arguments discussed above. Non-integer value of $\mu_T$ occurs due to severe distortion of structure. We also note that our results regarding to the unpaired spin of a domain and their net magnetic moment are in compliance with Lieb's theorem[52], which distinguishes $A$- and $B$-sublattices in honeycomb structure.

In conclusion, we showed that the interaction between unpaired spins associated with H vacancies in graphane gives rise to interesting magnetic structures. We revealed simple physical mechanisms underlying the magnetism of single-sided and double-sided vacancy domains. For single-sided domains, owing to the tendency to pair the spins of $\pi$-orbitals of adjacent C atoms, some of the adsorbed H atoms at the bottom side are relocated. At the end, the net magnetic moments can be attained in vacancy domains depending on their size and shape. For double-sided domains, interactions underlying the generation of net magnetic moment are relatively straightforward and are in good agreement with Lieb's theorem. Since the exchange coupling between different domains are hindered by domain walls, very dense data storage can be achieved through uniform coverage of identical domains. It is also noted that a graphane flake comprising a domain with large magnetic moment can be utilized as a non-toxic marker for imaging purposes. While magnetic 2D systems attract a great deal of attention due to their tunable properties at nanoscale, our results suggest that the size and ordering of magnetic moments of hydrogen vacancy domains with thin walls can be used for future data storage and spintronics applications.

# Chapter 4

# Graphane Nanoribbons

In this part of the thesis, we investigate the electronic and magnetic properties of graphane nanoribbons. We find that zigzag and armchair graphane nanoribbons with H-passivated edges are nonmagnetic semiconductors. While bare armchair ribbons are also nonmagnetic, adjacent dangling bonds of bare zigzag ribbons have antiferromagnetic ordering at the same edge. Band gaps of the H-passivated zigzag and armchair nanoribbons exponentially depend on their width. Detailed analysis of adsorption of C, O, Si, Ti, V, Fe, Ge and Pt atoms on the graphane ribbon surface reveal that functionalization of graphane ribbons is possible via these adatoms. It is found that C, O, V and Pt atoms have tendency to replace H atoms of graphane. We showed that significant spin polarizations in graphane can be achieved through creation of domains of H-vacancies and CH-divacancies. The results pertaining to this chapter are published in Ref.[[53]] and figures are reproduced with permission of the publisher.

## 4.1 Motivation

After the synthesis of two dimensional (2D) graphene[6, 8, 9, 10], its nanoribbons (NRs) have been a subject of interest both experimentally[22, 23] and theoretically.[26, 54, 25, 28, 12] Advances in experimental techniques is paving the

way for integrating the exceptional electrical, optical and magnetic functionalities of these nanometer-sized materials to future electronic technology.

Further to numerous theoretical and experimental works on graphene and its NRs, research efforts have been also devoted to synthesize its various derivatives. Notably, the synthesis of a 2D hydrocarbon in honeycomb structure,[41] namely graphane, followed its prediction through theoretical works.[42] Detailed analysis of hydrogenation processes of graphene leading to graphane and the existence of hydrogen (H) frustrations discussed very recently.[55] Furthermore, it was reported that graphane NRs are having more favorable formation energies than experimentally available graphene ribbons. [56] Recently, we reported the possibility of obtaining magnetization through dehydrogenation of domains on 2D graphane.[36] Modification of electronic structure of graphane by introducing either a hydroxyl group or a H-vacancy was also investigated with GW self-energy calculations. [57] Although there are several recent studies on graphane, electrical and magnetic properties of its NRs have remained unexplored.

Recent advances in graphane have motivated us to explore the properties of zigzag and armchair graphane NRs. In this thesis, using first-principles plane wave method within the density functional theory (DFT) we investigated the electronic and magnetic properties of bare and H- passivated graphane NRs. We also explored the effects of specific imperfections on these properties. These are various foreign atoms adsorbed on the surfaces of graphane NRs, vacancies and edge roughness. We found that these imperfections can attribute interesting functionalities by modifying the electronic and magnetic properties of graphane NRs.

We performed first-principles calculations[58] within DFT using projector augmented wave (PAW) potentials[46] and approximate exchange-correlation functional by spin polarized local density approximation[47] (LDA)as outlined in Chapter 2. Kinetic energy cutoff $\hbar^2|\mathbf{k}+\mathbf{G}|^2/2m$ for plane-wave basis set is taken as 500 eV. In the self-consistent potential and total energy calculations of 2D graphane a set of (35x35x1) $\mathbf{k}$-point sampling is used for Brillouin zone (BZ) integration. The convergence criterion of self consistent calculations for

ionic relaxations is $10^{-5}$ eV between two consecutive steps. By using the conjugate gradient method, all atomic positions and unit cells are optimized until the atomic forces are less than 0.03 eV/Å. Pressures on the lattice unit cell are decreased to values less than 1.0 kBar.

In order to correct the energy bands and band gap values obtained by LDA, frequency-dependent $GW_0$ calculations are carried out.[45] Screened Coulomb potential W, is kept fixed at initial DFT value $W_0$ and Green's function G, is iterated five times. $GW_0$ self-energy calculations are carried out with 15 Å vacuum spacing, default cut-off potential, 160 bands and 64 grid points.

Graphane NRs are treated by the supercell geometry within periodic boundary conditions. To hinder interactions between adjacent graphane NRs at least 15 Å vacuum spacing is placed between them. In specific cases double unit cell is used in our calculations to allow the possible antiferromagnetic (AFM) orderings along the ribbon edges. Reciprocal space integrations are carried out with 1x1x15 Monkhorst-Pack **k**-point grids.

## 4.2 Two Dimensional Graphane

For a better understanding of graphane NRs we start with 2D graphane which is derived from the hydrogenation of graphene, where each carbon atom is saturated by a single hydrogen atom. Accordingly, the primitive cell of graphane consists of two carbon and two hydrogen atoms. Chair like configuration of infinite sheet of 2D graphane is formed, whereby each carbon atoms of A- and B-type sublattices are saturated by hydrogen atoms from above and below, respectively, as described in Fig. 4.1(a). This is known as the most favorable and stable hydrocarbon conformation.[42, 36] The planar graphene honeycomb structure, which is stabilized by planar $sp^2$-hybrid orbitals and $\pi$-bonding between adjacent perpendicular $p_z$-orbitals is puckered (buckled) as a result of the adsorption of H atoms, whereby a single C atom is bound to three adjacent C atoms and a single H atom through 'tetrahedrally coordinated' $sp^3$-like hybrid orbitals. The buckling,

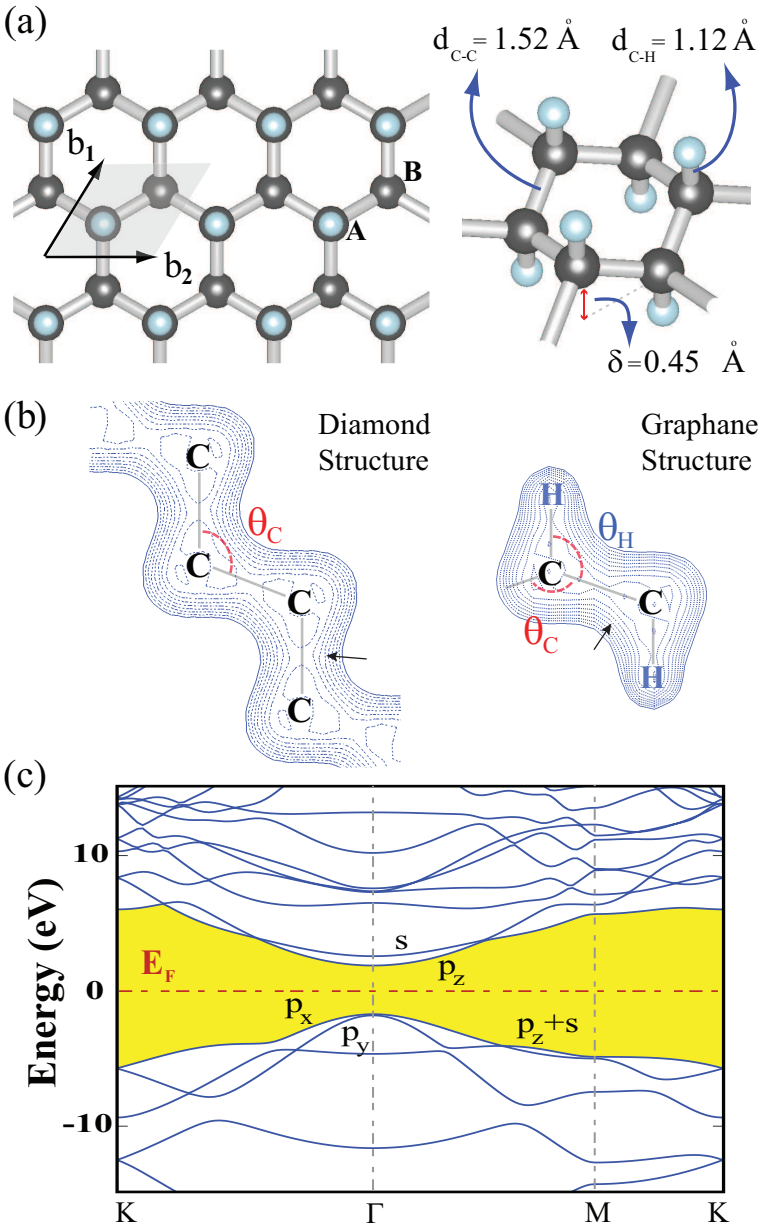


Figure 4.1: (Color online) (a) Top and perspective view of the atomic structure of infinite 2D graphane sheet having honeycomb structure. Two sublattices of graphane are indicated by A and B. Black (dark) and blue (light) balls are for carbon and hydrogen atoms, respectively. (b) Charge density contour plots of diamond and graphane are shown on a plane passing through C-C-C-C and H-C-C-H bonds, respectively. The tetrahedral angle of the diamond $\theta_C = 109.47^o$. Arrows indicate the direction of increasing charge density. The calculated values of $\theta_C$ and $\theta_H$, namely C-C-C and H-C-C bond angles in graphane respectively, are given in Table 4.1. Contour spacings are 0.0286 e/Å$^3$. (c) The LDA energy band structure where the orbital character of specific bands is also given. The band gap is shaded yellow/gray.

$\delta$, i.e. the perpendicular distance between A-type and B-type carbon sublattices, is calculated to be 0.45 Å. As a result, the lattice constant of graphene increases from 2.46 Å to 2.51 Å and hence the C-C and C-H bond distances become 1.52 and 1.12 Å, respectively, as indicated in Fig. 4.1(a). The charge density contour plots given in Fig. 4.1(b) indicates that the charge distribution in graphane especially around the C-C bond is reminiscent of that in tetrahedrally coordinated diamond. In graphane, the angle of $\theta_H$ between H-C and C-C bonds and $\theta_C$ between adjacent C-C bonds are $107.35^o$ and $111.51^o$ respectively. The mean value of these angles is equal to the tetrahedral angle $\theta_C$ of diamond. The maximum of the C-C bond charge in diamond and in graphane are found to be $\sim 0.282$ and $\sim 0.286$ e/Å$^3$, respectively.

The cohesive energy of graphane (per unit cell) relative to free C and H atoms is obtained from $E_c = 2 \times E_T^H + 2 \times E_T^C - E_T^{Gra}$, where $E_T^H$ and $E_T^C$are the total energies of single free C, and free H, whereas $E_T^{Gra}$ is the total energy of graphane. The cohesive energy depends whether the energies of magnetic or nonmagnetic states of free C and free H atoms are considered. Here the cohesive energy per unit cell of graphane is calculated to be 23.57 (27.65) eV by considering the magnetic (nonmagnetic) states of free atoms. As for the average C-H bond energy, one can use the formula $E_{C-H} = (-E_T^{Gra} + E_T^{Gre} + 2 \times E_T^H)/2$ where $E_T^{Gre}$ is the total energy of graphene. The calculated value is 2.84 (3.74 for nonmagnetic case). We reported[36] that the desorption of a single H atom from the graphane is an endothermic reaction with an energy of 4.79 eV. When compared with the energy of C-H bond, the desorption energy of single H is larger, since the single H removal creates reconstruction of nearby atoms which further reduces the total energy of the system.

Due to $sp^3$-saturation of C atoms, 2D graphane is a nonmagnetic semiconductor with a direct band gap of 3.42 eV as shown in Fig. 4.1(c). However, this band gap, which is underestimated within DFT, is corrected by $GW_0$ approximation to become 5.97 eV.[36, 57] While the top of the valence band originates from $p_x$- and $p_y$-orbitals of C atoms, the bottom of the conduction band has C-$p_z$ orbital character. Earlier, we also calculate[36] the phonon modes of infinite 2D graphane, which yield all real frequencies in BZ. Having all frequencies positive

Table 4.1: Comparison of the calculated quantities of graphene and graphane. Lattice constant, $a$; C-C bond distance, $d_{C-C}$; C-H bond distance, $d_{C-H}$; the buckling, $\delta$ [see Fig. 4.1(a)]; angle between adjacent C-C bonds, $\theta_C$ [see Fig. 4.1(b)]; angle between adjacent C-H and C-C bonds, $\theta_H$; energy band gap calculated by LDA, $E_g^{LDA}$; energy band gap corrected by $GW_0$, $E_g^{GW_0}$; cohesive energy $E_c^{nm}$, ($E_c^m$) obtained with respect to nonmagnetic (magnetic) free atom energies; the C-H bond energy, $E_{C-H}^{nm}$ ($E_{C-H}^m$) obtained with respect to nonmagnetic (magnetic) free atom energies; photoelectric threshold (work function), $\Phi$; in-plane stiffness, $C$ and Poison ratio, $\nu$.

| Material (1x1) unit cell | $a$ (Å) | $d_{C-C}$ (Å) | $d_{C-H}$ (Å) | $\delta$ (Å) | $\theta_C$ (deg) | $\theta_H$ (deg) | $E_g^{LDA}$ $(eV)$ | $E_g^{GW_0}$ $(eV)$ | $E_c^{nm}$ $(eV)$ | $E_c^m$ $(eV)$ | $E_{C-H}^{nm}$ ( $eV$ ) | $E_{C-H}^m$ $(eV)$ | $\Phi$ $(eV)$ | $C$ $(J/m^2)$ | $\nu$ |
|---|---|---|---|---|---|---|---|---|---|---|---|---|---|---|---|
| Graphene | 2.46 | 1.42 | - | - | 120 | - | 0.00 | 0.00 | 20.16 | 17.87 | - | - | 4.77 | 335[?] | 0.16 |
| Graphane | 2.51 | 1.52 | 1.12 | 0.45 | 111.51 | 107.35 | 3.42 | 5.97 | 27.65 | 23.57 | 3.74 | 2.84 | 4.97 | 243[?] | 0.07 |

indicate the stability of graphane structure.

An exceptional feature of graphane is related with its interesting charging configuration. While graphene has a covalent bonding, upon the saturation of each C atom by a single H atom, a charge of $\delta Q \sim 0.1$ electrons is transferred from H to C. At the end, the negatively charged bilayer of carbon atoms becomes sandwiched between positively charged H layers. Graphane having this charging has the photoelectric threshold (work function) calculated to be $\Phi$=4.97 eV, which is 0.2 eV larger than that of graphene. In Table 4.1, we presented the calculated values related with structure, energy bands, photoelectric threshold etc. of graphane and graphene for the sake of comparison. To be complete Table 4.1 also includes calculated elastic constants such as in-plane stiffness[59] $C$ [$= \frac{1}{A}(\frac{\partial^2 E_T}{\partial \epsilon^2})$, where $E_T$ is the total energy of the system under strain, $\epsilon$ is the uniaxial strain and $A$ is the area of the unit cell] and Poisson's ratio[20] $\nu$.

## 4.3 Graphane Nanoribbons

The ribbons cut from a 2D graphane are structures providing important features for various technological applications. Two major families of graphane NRs are distinguished depending on their orientations; namely armchair, and zigzag

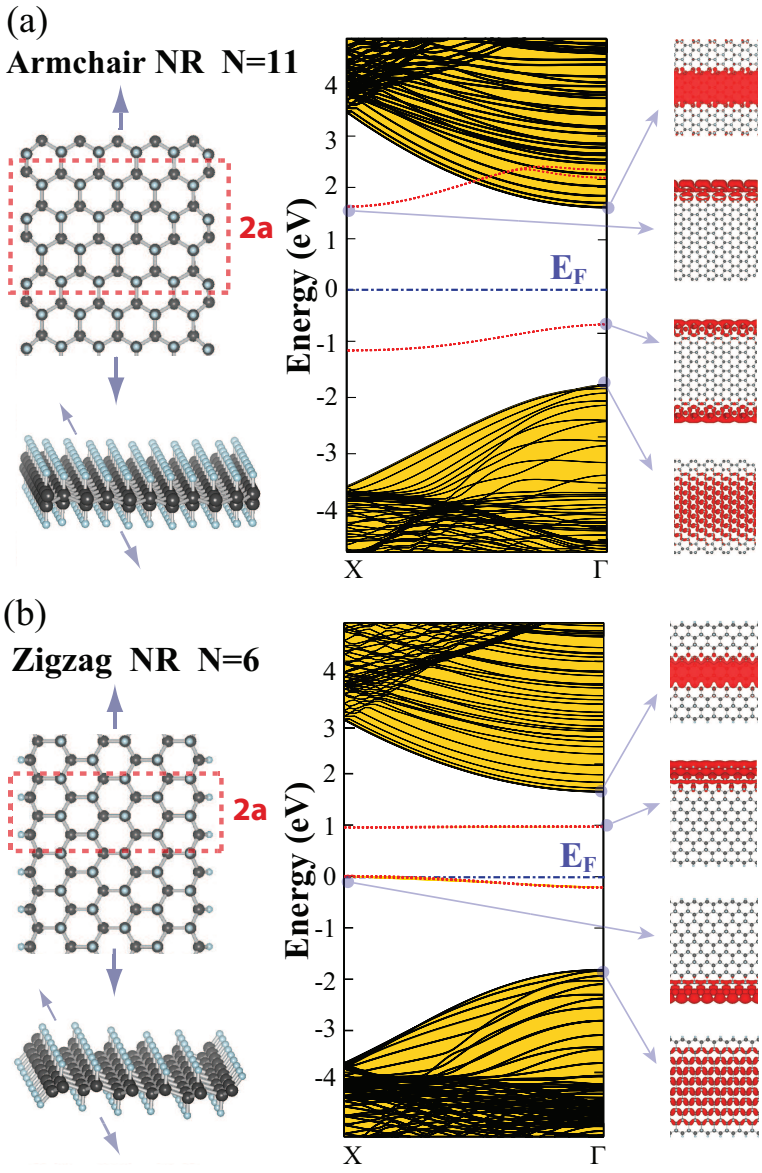


Figure 4.2: (Color online) (a) Atomic structure of bare armchair graphane NR having $N$=11. The double unit cell of the ribbon is delineated by red/dashed lines with the lattice constant $2a$. Large/black and small/light blue balls indicate carbon and hydrogen atoms. Energy band structure corresponding to the armchair NR and charge density of selected bands are shown in the panels at the righthand side. (b) Atomic structure of bare zigzag graphane NR having $N$=6 with double unit cell delineated by red/dashed lines and with lattice constant $2a$. Energy band structure and isosurface charge density of selected states corresponding to zigzag NR are indicated. Bands shown by red/dotted lines are derived from edge states. Zero of energy is set to the Fermi level, shown by dash-dotted lines, of the ribbons with H-passivated edges. In spin polarized calculations double unit cell is used to allow antiferromagnetic order along the edges.

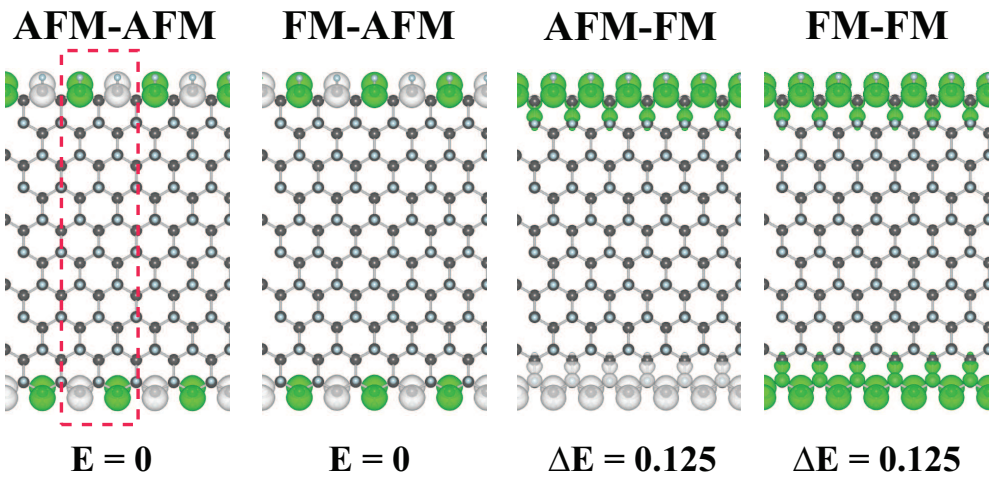


Figure 4.3: (Color online) Total energies of possible magnetic orderings at the edges of bare zigzag graphane ribbons. Calculations are performed in double unit cell delineated by red/dashed lines. Spin up and spin down states are shown by green/dark and grey/light isosurfaces of the difference charge density, $\Delta\rho$.

graphane NRs. Apart from the orientation, graphane NRs are characterized by their widths. For armchair graphane NRs, the width, $N$, is defined by the number of C-C dimers in the unit cell which are parallel to the axis of the ribbon; for zigzag graphane NRs, $N$ denotes the number of zigzag carbon chains along the ribbon axis. The electronic structure changes depending on whether the dangling bonds of carbon atoms at the edge are free (bare) or passivated by single H atoms. In Fig. 4.2(a) and 4.2(b) we show the atomic and electronic structure of armchair and zigzag graphane NRs with $N$=11 and $N$=6, respectively.

Bare armchair NR is a nonmagnetic indirect band gap semiconductor, since the electrons at the dangling orbitals are paired. The band gap of 2D graphane is reduced due to the bands of edge states of dangling bonds occurring in the band gap. The charge density analysis of these edge state bands presented in Fig. 4.2(a) clearly shows that they are localized at the edges of the NR. Upon hydrogen passivation of the threefold coordinated edge atoms, the edge state bands in the gap disappear and the direct band gap opens up.

Similar to armchair graphane NRs, the dangling bonds of the threefold coordinated carbon atoms at both edges of zigzag graphane NRs give rise to edge states in the band gap. Owing to relatively large distance between adjacent dangling bonds and hence their relatively smaller coupling, they have minute dispersion. Charge density isosurfaces of these edge states confirm their localization at the edges. Also, owing to their weak coupling the spins of adjacent dangling bonds cannot be paired. Consequently, each carbon atom at the zigzag edge attains a magnetic moment of 1 Bohr magneton ($\mu_B$). The ordering of these magnetic moments is however dramatically different from that of the zigzag graphene NRs. The significant coupling between two spin states at different edges gives rise to antiferromagnetic (AFM) ordering along the graphene edge.

The physical origin of the magnetic interactions between the edges of graphitic fragments was treated earlier.[60] For zigzag graphene ribbon, collective alignment of the magnetic moments along the same ribbon edge through the ferromagnetic (FM) interaction, but AFM ordering between opposite edges is attributed to magnetic tail interactions. The magnetic ordering of a wide zigzag graphane NRs ($\sim$ 2 nm) are examined in a supercell comprising two unit cells, whereby antiferromagnetic ordering between adjacent dangling bonds at the same edge is allowed. We consider four different orderings, such as AFM-AFM (where, respectively, the ordering of magnetic moments at the atoms located at different and same edge are antiferromagnetic), FM-AFM, AFM-FM and FM-FM as described in Fig. 4.3. Here the difference charge density is defined as the $\Delta\rho = \rho^{(\uparrow)} - \rho^{(\downarrow)}$ where $\rho_{\uparrow(\downarrow)}$ is spin up (down) charge. Since the magnetic interaction between two edges is vanished, AFM-AFM and FM-AFM orderings have the same total energy corresponding to the ground state. These orderings are 125 meV energetically more favorable than the AFM-FM and FM-FM orderings. From this analysis it is revealed that AFM spin alignment between adjacent atoms at the same edge is preferred by the zigzag graphane NRs. FM ordering between two spins has 62.5 meV higher energy. For zigzag NR with $N$=6, the magnetic coupling between two edges is negligible and hence either AFM-AFM or FM-AFM orderings have the same energy and they are ground states. However, when the width of the ribbon is less than 12 Å the degeneracy of AFM-AFM and FM-AFM states is

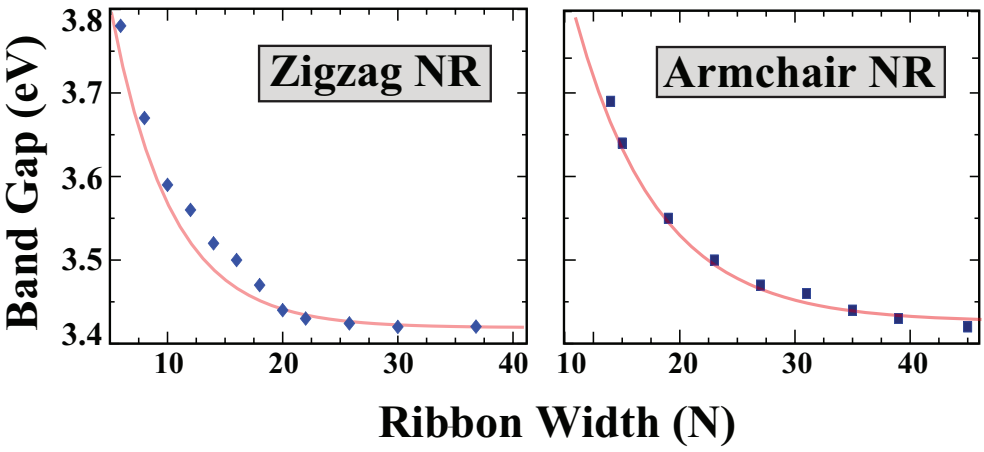


Figure 4.4: (Color online) Variation of the energy band gap of H-passivated zigzag and armchair NRs of graphane as a function of width given by $N$. The variation of the band gap with $N$ is fitted to the curve given by continuous line. (See text)

broken. The bare zigzag NR is an indirect and antiferromagnetic semiconductor with an indirect band gap relatively smaller than that of 2D graphane. However, it becomes nonmagnetic, direct band gap semiconductor upon passivation of the dangling bonds. Also the magnetic edge states disappear and band gap becomes larger.

The value of band gap of graphane NRs can differ from that of parent 2D structure due to a combined effects of quantum confinement, edge state bands as well as folding in the direction perpendicular to the NR axis. Here we examined the variation of the band gap with $N$ and observed that the quantum confinement effect, in fact, occurs in graphane NRs, even if it is not as emphasized as that found in graphene NRs. In Fig. 4.4, H-passivated armchair and zigzag graphane NRs displays a quantum confinement effect, namely the band gap reducing with increasing width or $N$. This behavior is fitted to an expression as:

$$E_{gap}(N) = 3.42\ eV + \alpha \exp(-N\beta) \tag{4.1}$$

Here $\alpha$ and $\beta$ are fitting parameters. The values of $\alpha$ and $\beta$ are found to

Table 4.2: Summary of the calculated quantities for adatoms adsorbed on a H-passivated armchair graphane NR. The first and second lines in each row associated with a given adatom adsorbed to edge site and the sites near the center of the graphane NRs, respectively. $d_H$, the adatom-nearest hydrogen distance; $d_C$, the nearest adatom carbon distance; $E_b$, adatom binding energy; $\mu_T$, magnetic moment per supercell; $\rho^*$, excess charge on the adatom (where negative sign indicates excess electrons); $\Phi$, photoelectric threshold (work function); $p$, dipole moment; $E_i$ energies of localized states associated with adatoms. Localized states are measured from the top of the valence band. The occupied ones are indicated by bold numerals and their spin alignments are denoted by either $\uparrow$ or $\downarrow$. Up to first seven adatom states of $E_i$ are shown.

| *Atom* | *Site* | $d_H$ (Å) | $d_C$ (Å) | $E_b$ ($eV$) | $\mu_T$ ($\mu_B$) | $\rho^*$ (e) | $\Phi$ ($eV$) | p (e×Å) | $E_i$ ↑: Spin-up, ↓: Spin-down States |
|---|---|---|---|---|---|---|---|---|---|
| **C** | $E \rightarrow E1$ | 1.27 | 2.05 | 1.10 | 2.00 | -0.28 | 3.85 | 0.02 | **0.45**↑, **0.88**↑, 2.17↓, 2.88↓, 3.53↑, 3.64↓ |
| | $TH \rightarrow M1$ | 1.12 | 1.45 | 3.99 | 0.00 | -0.18 | 4.02 | 0.34 | **0.72, 1.52** |
| **O** | $E \rightarrow E4$ | 0.98 | 1.42 | 5.67 | 0.00 | -1.23 | 4.63 | 0.19 | **-0.87, -0.50, -0.22, 0.00**, 4.80 |
| | $TH \rightarrow M1$ | 0.98 | 1.43 | 5.89 | 0.00 | -1.27 | 4.59 | 0.11 | **-1.16, -1.02, -0.66**, 4.08 |
| **Si** | $E \rightarrow E3$ | 1.88 | 2.65 | 0.54 | 2.00 | 0.03 | 3.42 | 0.03 | **1.20**↑, **1.34**↑, 2.36↑, 2.43↓, 2.56↓, 2.95↓ |
| | $TH \rightarrow TH$ | 1.84 | 3.00 | 0.68 | 2.00 | -0.02 | 3.59 | 0.42 | **1.23**↑, **1.24**↑, 1.93↑, 2.42↓, 2.45↓, 2.46↓ |
| **Ti** | $E \rightarrow E2$ | 1.97 | 2.16 | 0.81 | 2.00 | 0.19 | 2.65 | 0.27 | **1.77**↑, **2.30**↓, **2.34**↑, **2.43**↑, 2.81↑, 2.89↑, 3.11↑ |
| | $TC \rightarrow TC$ | 1.95 | 2.52 | 0.89 | 3.91 | 0.31 | 2.16 | 0.92 | **2.18**↑, **2.48**↑, **2.49**↑, **2.95**↑, 3.18↓, 3.27↑, 3.28↑ |
| **V** | $E \rightarrow E1$ | 1.99 | 2.40 | 0.54 | 5.00 | 0.14 | 2.56 | 0.22 | **1.49**↑, **2.10**↑, **2.38**↑, **2.43**↑, **2.50**↑, 2.70↑, 3.16↓ |
| | $TC \rightarrow M3$ | 1.71 | 2.07 | 1.24 | 3.00 | 0.93 | 3.13 | 0.43 | **0.10**↑, **0.49**↓, **1.45**↑, **1.60**↑, **1.84**↑, 2.20↑, 3.03↓ |
| **Fe** | $E \rightarrow E2$ | 1.90 | 2.15 | 0.57 | 4.00 | 0.05 | 3.21 | 0.36 | **-0.42**↑, **-0.27**↑, **-0.08**↑, **-0.03**↑, **0.03**↑, 1.48↓, 1.59↑ |
| | $HO \rightarrow HO$ | 1.95 | 2.83 | 0.65 | 4.00 | 0.07 | 2.98 | 0.53 | **-1.15**↓, **-0.75**↑, **-0.57**↑, **-0.41**↑, **-0.34**↑, **0.09**↑ , 1.39↑ |
| **Ge** | $E \rightarrow E3$ | 1.96 | 2.71 | 0.48 | 2.00 | 0.00 | 3.38 | 0.03 | **1.27**↑, **1.38**↑, 2.25↑, 2.41↓, 2.52↓, 2.81↓ |
| | $TH \rightarrow TH$ | 1.91 | 3.06 | 0.62 | 2.00 | -0.02 | 3.55 | 0.36 | **1.30**↑, **1.31**↑, 1.89↑, 2.38↑, 2.42↑, 2.43↑ |
| **Pt** | $E \rightarrow E5$ | 1.56 | 2.00 | 3.79 | 0.00 | -0.13 | 4.57 | -0.09 | **-0.78, -0.36, -0.13**, 0.13, 2.76 |
| | $TH \rightarrow M2$ | 1.54 | 2.04 | 3.50 | 0.00 | -0.18 | 4.30 | 0.34 | **-0.36, -0.21, 0.38**, 2.58, 3.43 |

be 1.18 eV and 0.19 for zigzag graphane NRs (2.15 eV and 0.14 for armchair graphane NRs). The band gaps of both types of graphane NRs go to 3.42 eV as $N \rightarrow \infty$. Considering the $GW_0$ corrected value of the band gap, 5.97 eV, the above fitting can be expressed as $E_{gap}(N) = 5.97 + \alpha \exp(-N\beta)$ assuming that the same scissor operation is applicable for graphane NRs. Apparently, the band gap values of graphane NRs calculated using DFT are underestimated and hence their values are expected to occur $\sim$ 2.5 eV larger than presented in Fig. 4.4. Unfortunately, $GW_0$ self-energy corrections cannot be performed for graphane NRs due to large computational time. We note that the variation of band gap is relevant for $N < 22$ for zigzag graphane NRs and $N < 30$ for armchair graphane NRs.

## 4.4 Functionalization of Graphane NRs by Adatoms

Adsorption of adatoms is widely used and an efficient way to provide new functionalities to structures in nanoscale applications.[19, 40, 61] Adsorption of C, O, Si, Ge, Pt, V, Fe and Ti adatoms on graphane ribbons is investigated by using (1x1x6) supercell of H-passivated armchair NR having $N$=8. Adsorption geometry is determined by calculating the lowest binding energy corresponding to the optimized structures. To this end, the binding energies of adatoms at four initial sites described in Fig. 4.5: These are edge site E; hollow site HO, top site of the carbon TC and top site of the hydrogen atom TH in the middle of NR. The stable binding sites are determined upon structure relaxation. In the same figure the positions of adatoms after relaxation are also shown. Binding energies ($E_b$) of these atoms are calculated by using the expression

$$E_b = -E_T[NR + A] + E_T[NR] + E_T[A] \tag{4.2}$$

in terms of the total energies of the optimized structure of NR with adatom, $E_T[NR + A]$; bare NR, $E_T[NR]$ and free adatom, $E_T[A]$. Owing to the large graphane ribbon unit cell, **k**-point sampling is done only along the axis of the ribbon. All the energies are calculated in the same unit cell and obtained from the lowest ground-state total energies (either magnetic or nonmagnetic). Initially, at least 2 Å distance between adatom and outermost graphane atom is provided to find the relaxation site of adatom on the ribbon.

An atom adsorbed on NR may give rise to resonance states in the valence and conduction bands, and also localized states in the band gap. Owing to the periodic boundary conditions, the energy states associated with these adatoms may form energy bands. Since we consider a supercell consisting of six unit cell of H-passivated armchair NR, the adatom-adatom distance is large and prevents coupling between adjacent adatoms. In this respect, the flat bands associated with adatoms can mimic either resonance or localized states relevant for dilute doping.

In Table 4.2, we present nearest neighbor distances between adatom and H ($d_H$) and C ($d_C$), binding energy ($E_b$), total magnetic moment of the system

($\mu_T$), charge transfer between adatom and adsorbate ($\rho*$). Since the inversion symmetry of graphane can be broken by the adsorption of an atom, a net electric-dipole moment can be induced thereof. Thus electric dipole moment values p, induced by adatom are also listed in Table 4.2. Photoelectric threshold of the adatom+graphane system perpendicular to the plane of NR, $\Phi$, is calculated by the difference of the electrostatic potential at distances where the gradient of it is negligible and the Fermi level of the adsorbed system. It should be noted that both p and $\Phi$ is relevant only for uniform coverage of graphane. For a dilute impurity these calculated values converge to that of armchair graphane. When the width of armchair NR is large enough, one expects the photoelectric threshold, $\Phi$, and dipole moment, p, to converge to 4.97 eV and 0 eÅ, respectively.[36]

We found that some atoms, such as C, O, V and Pt that are adsorbed on the H-passivated armchair NR surface show a tendency to remove H atoms from graphane surface. Since the single atoms of C, O, V and Pt have rather high binding energy, it seems possible to create graphene domains on graphane by striping H atoms but covering the domain by adsorbed atoms. Independent of their initial position, C and O atoms are adsorbed to carbon atoms of graphane by replacing H atoms. A typical binding configuration of C and O is indicated as M1 in Fig. 4.5. Adsorption of C and O atoms occur at the middle of ribbon with strong binding energies of 5.89 and 3.99 eV, respectively. The resulting system is nonmagnetic. Binding structures of Pt and V, which also remove H atom from the host C atom of graphane, are also shown in the same figure.

Although H has very low binding energy (and hence is not shown in Table 4.2), it may be important for striping H atoms from graphane. Upon all geometry relaxations from different initial conditions, single adsorbed H atom prefers to bind on top of H atom of graphane and forms $H_2$ molecule which is weakly bound to the nearest C atom. The binding energy of $H_2$ molecule is calculated to be $\sim 36$ meV.

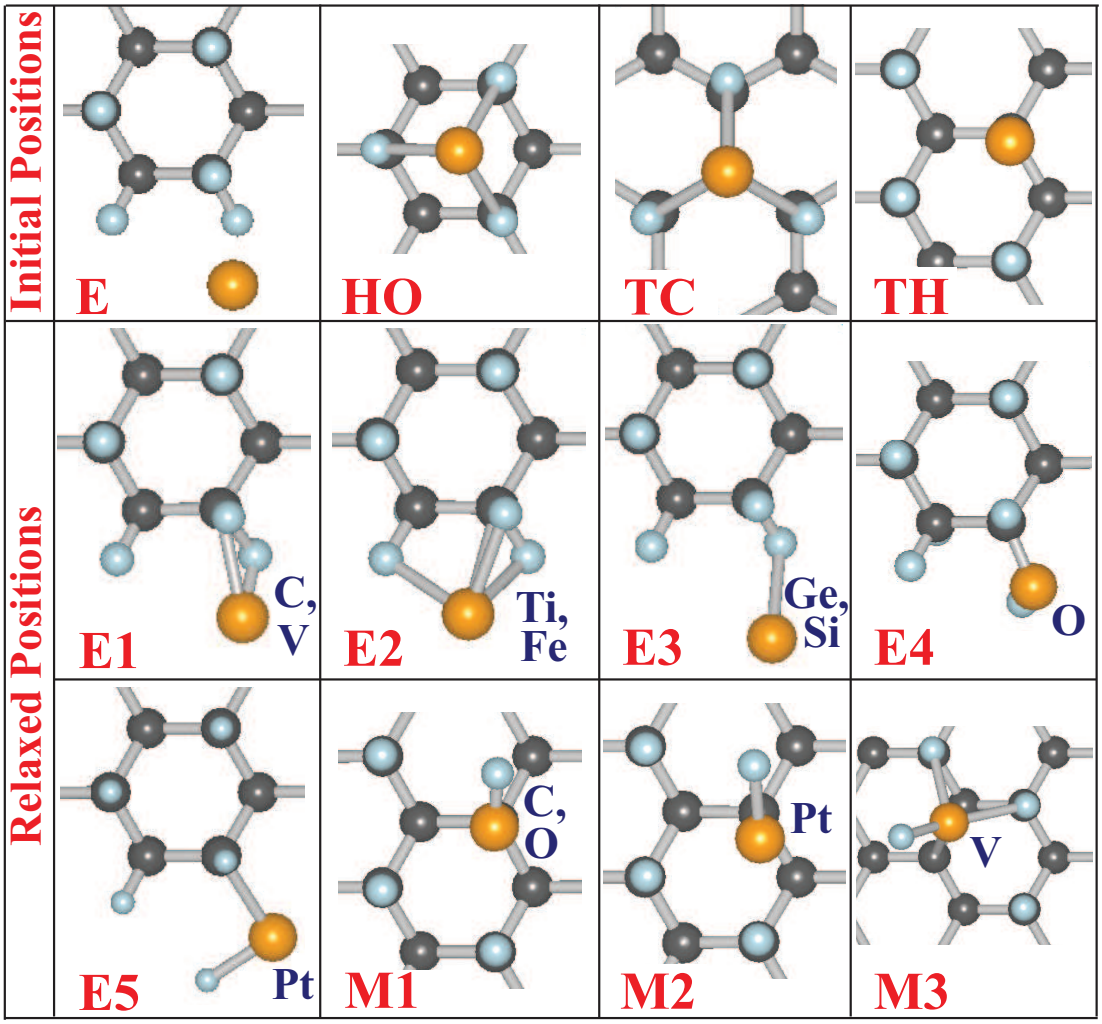


Figure 4.5: (Color online) Schematic representations of possible positions of adatoms on a large H-passivated armchair graphane ribbon. Positions of adatoms obtained after the structure optimization through minimization of total energy and forces exerting on the atoms are also shown.

## 4.5 Vacancies in Graphane NRs

In our recent study[36], we showed that a graphane, which has a nonmagnetic (NM) ground state, can be made magnetic simply by removing hydrogen atoms from the uniform hydrogen layers adsorbed on its both sides. It was found that the magnetization depends on whether the defect region is one-sided or two-sided. It was also shown that in certain circumstances remarkably large magnetic moments can be attained in a small domain on the sheet of graphane. Experimentally, removal of surface hydrogen atoms by using laser beam resonating with surface-atom bond[48] and ionic vapor application[49] are reported before. Since it is revealed that the double-sided vacancies give higher magnetic moments we focus on these type of vacancies on the ribbons.

In this section we consider six different types of vacancies in a bare armchair NR with $N$=15. Upon desorption of a single hydrogen atom, as shown in Fig. 4.6, local bonding through $sp^3$-hybrid orbital is retransformed into planar $sp^2$- and perpendicular $p_z$-orbitals. At the vacancy site one electron accommodated by the dangling $p_z$-orbital becomes unpaired and hence contributes to the magnetization by 1 $\mu_B$. We also calculated that a single H-vacancy located at the center of the NR has 70 meV lower energy than that located near the edge of the ribbon.

The situation is rather intriguing for the magnetization of large domains of hydrogen vacancies. As in the case of single H-vacancy, leading to transformation of $sp^3$-bonding into planar $sp^2$-bonding, triangular $\Delta$, and rectangular *square* shaped large graphene islands can be created by removing H atoms hence by creating H-vacancy domains. As shown in Fig. 4.6, hydrogen desorbed triangle-shaped island consisting of $n$ carbon atom at its each edge is defined as $\Delta$n-type H-vacancy. Therefore, a $\Delta$n-type vacancy domain can be obtained by removing $n(n+1)/2$ H atom from top side and $n(n-1)/2$ H atom from down side of the graphane ribbon. This means that $n(n+1)/2$ $p_z$-orbital electrons freed from A-type and $n(n-1)/2$ $p_z$-orbital electrons freed from B-type sublattice C atoms. According to the Lieb's theorem [52] net magnetic moment of such a system can be calculated from the difference between the sublattice atoms. For triangle vacancies this difference is simply equal to $n$ and thus the $\Delta$n-vacancy domain

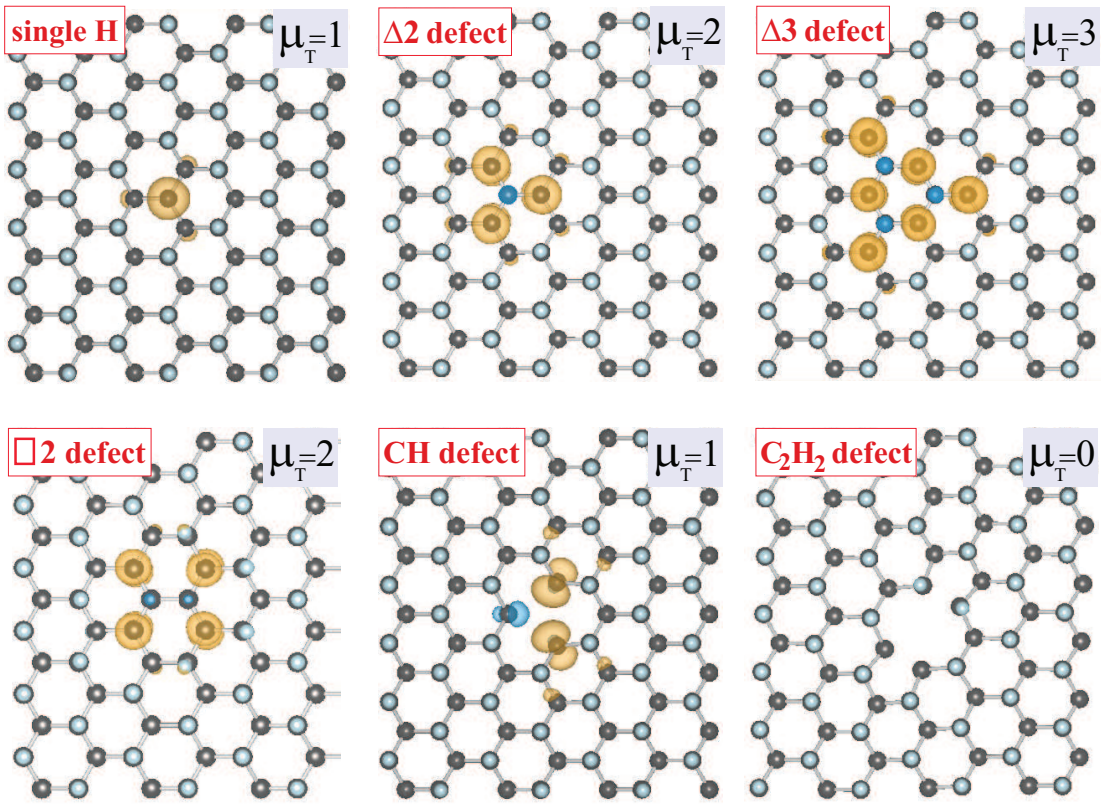


Figure 4.6: (Color online) Atomic structures corresponding to single-H, double-sided triangular shaped $\Delta 2$ and $\Delta 3$, double-sided rectangular shaped, CH and $C_2$ H $_2$ vacancies and resulting difference charge $\Delta\rho = \rho^{(\uparrow)} - \rho^{(\downarrow)}$, surfaces for a bare armchair graphane NR. Large/black and small/light blue-gray balls indicate C and H atoms, respectively. Only a small part which includes vacancy region and its nearby atoms, of the armchair NR with $N$=15 is shown. density.

has net magnetic moment with $n\mu_B$. However, the *square*-type domains does not yield large magnetic moments and have values between 0 and 2 $\mu_B$. It is seen that magnetic interactions in double-sided triangular and square H-vacancy domains resulting in net magnetic moments are relatively straightforward and are in good agreement with Lieb's theorem.

We also consider CH- and $C_2H_2$-vacancies, the synthesis of them are relatively easier than creating only H-vacancies. In our study, these vacancies are first created in a NR by removing involved atoms and subsequently their structures are optimized. Calculated values of magnetic moments of the structure are presented in Fig. 4.6. After the creation of a CH-vacancy on a graphane ribbon, geometric structure rearranges itself via Jahn-Teller-like distortion in the lattice. Charge density plot in Fig. 4.6 shows the unpaired up and down spin electron states located on the region surrounding the vacancy. It is seen that a bare armchair NR, which is nonmagnetic semiconductor when it is defect free, attains permanent magnetic moment in the presence of CH-vacancies. While CH-type vacancy makes small changes in the geometric structure, Stone-Wales type deformation occurs after formation of the $C_2H_2$-vacancy. Since electrons are paired in $C_2H_2$-vacancy, the ground state is again nonmagnetic and thus there is no visible difference charge density in Fig. 4.6. From the point view of Lieb's theorem, removal of a CH couple creates an absence in the number of $p_z$-orbital electron belonging to a A-type (or B-type) sublattice. Upon the creation of $C_2H_2$-vacancy, both the A- and B-type sublattices lose one electron and thus the difference is zero resulting in a nonmagnetic ground state. Our results are consistent with the recently reported values for CH-vacancies in infinite sheets of graphane.[62]

## 4.6 Edge Roughness

Earlier, it was shown that the edge roughness of graphene NRs can affect their electronic and mechanical properties. In particular, it was revealed that periodically repeating edge profiles can be treated within the superlattice structure, which result in confinement of spin states in zigzag NRs.[63] Band alignments of these superlattice structures have been studied both experimentally and theoretically.[64] Here we investigated the effect of periodically repeating edge roughness of a bare zigzag NR. While one edge of NR is kept flat, periodically repeating undulations are carved at the other edge. The same structure can be viewed as periodically repeating heterostructures of wide ($N$=8) and narrow ($N$=6) segments of zigzag graphane NRs. Atomic and electronic band structure of this superlattice, which mimics the edge roughness are shown in Fig. 4.7. Here we note that infinite bare zigzag NR with $N$=8 has a band gap of 0.8 eV, while the band gap of infinite bare zigzag NR with $N$=6 is relatively wider and 0.9 eV. As pointed out in Sec. IV, wide band gap of H-passivated graphane NRs is reduced to 0.8-0.9 eV because of edge states of unpassivated dangling bonds of bare graphane NRs, which appear in the band gap. These edge states in Fig. 4.7 of the superlattice occur as several closely lying flat bands below and above the Fermi level separated by a superlattice band gap of $\sim$0.8 eV. The character of various bands are revealed by plotting the charge density isosurfaces of various states. Charge density isosurfaces of the highest filled spin up and spin down edge state indicates localization at the flat edge. As for the charge distribution of the lower lying valence states is rather uniform along the narrow region. The states of the flat band at the edge of the conduction band is confined in the wide segment of the superlattice since they cannot find a matching state in the narrow region. As a proof of the concept, it is shown that electronic states can be confined at specific regions of periodic edge roughness. Of course, confinement, superlattice band gap etc. depend on the structural parameters of superlattices and need detailed investigation.

Research on recently synthesized graphane revealed interesting electronic and

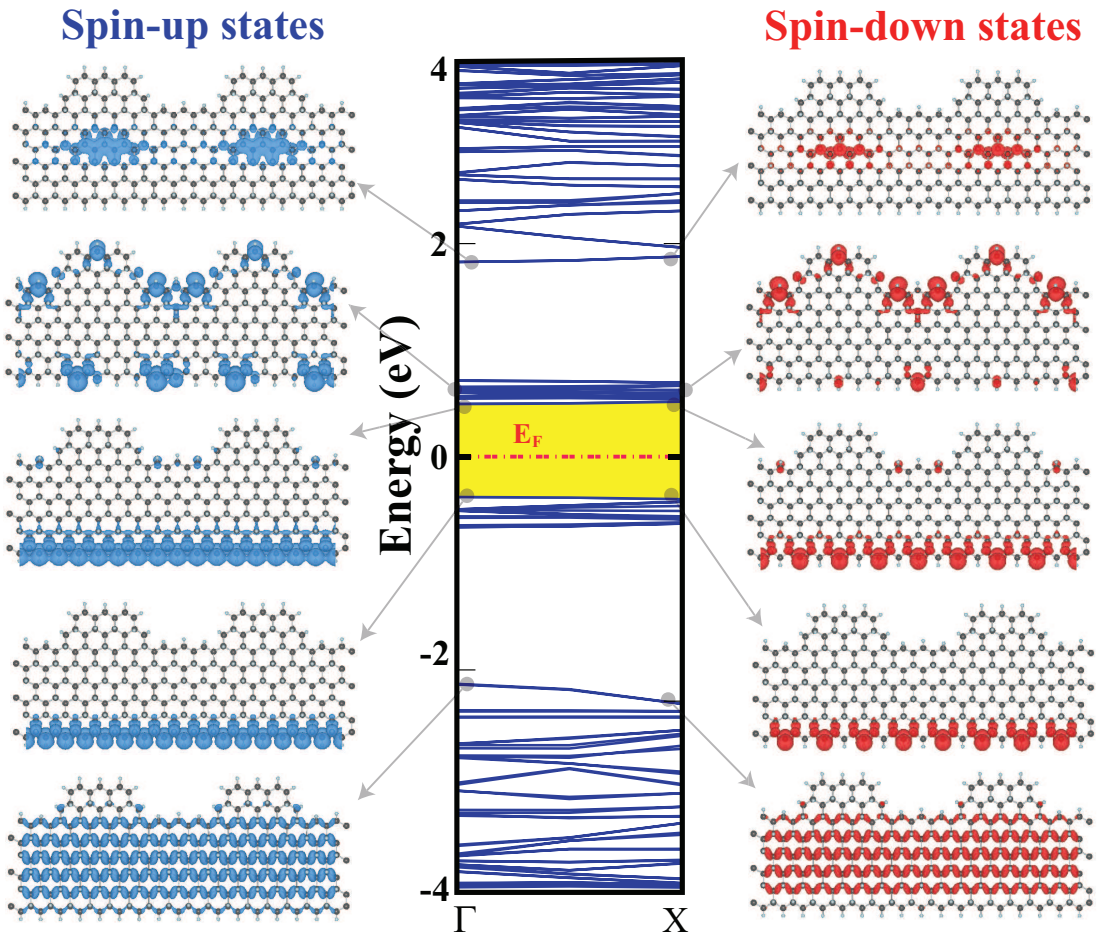


Figure 4.7: (Color online) Energy band diagram and band projected charge density isosurfaces of various states for bare zigzag NR including edge roughness. The band gap between edge states are shaded yellow/gray. Zero of the band energy is set to the Fermi level.

magnetic properties of this two dimensional honeycomb structure. Graphane attains a $sp^3$-like bonding through covering of its both sides by hydrogen atom. This bonding is rather different from the $sp^2$-bonding of graphene and attributes a number of additional properties to graphane. For example, in contrast to semimetallic graphene with linear band crossing at the Fermi level, graphane is a nonmagnetic, wide band semiconductor.

The armchair and zigzag graphane NRs of graphane display important number of properties and hence constitute basic structures to fabricate various devices. Both zigzag and armchair graphane NRs are wide band gap semiconductor when their edges are passivated with hydrogen. The band gaps vary exponentially with their widths. For narrow graphane NRs the band gap is large due to quantum confinement effect, but approaches to the band gap of graphane as the width increases. Unpaired, unpassivated dangling bonds at the edges have 1 Bohr magneton magnetic moment and have antiferromagnetic coupling with adjacent dangling bonds. These graphane NRs can be functionalized to attain additional properties through H-passivation of their edges, adatom adsorption, vacancy creation, edge profiling and superlattice formation. In particular, graphane NRs attain magnetic moment through the creation of H vacancy at the surfaces of graphane. This property can be utilized to achieve interesting functionalities through decoration and patterning of H-vacancies on the graphane NRs. The possibility of generation of large magnetic moments at small domains of H-vacancies makes graphane based structures promising fordata storage and nanospintronics applications. These functionalities can be further extended by adsorbing adatoms to carbon atoms deprived from hydrogen.

In conclusion, the present study demonstrates that graphane NRs can be an important basic nanomaterial and presents interesting properties for future technological applications.

# Chapter 5

# Fluorinated Graphene

## 5.1 Motivation

Recent synthesis of fluorinated graphene introduced interesting stable derivatives of graphene. In particular, fluorographene (CF), namely fully fluorinated chair conformation, is found to display crucial features, such as high mechanical strength, charged surfaces, local magnetic moments due to vacancy defects and a wide band gap rapidly reducing with uniform strain. These properties, as well as structural parameters and electronic densities of states are found to scale with fluorine coverage. However, most of the experimental data reported to date neither for CF, nor for other $C_nF$ structures complies with the results obtained from first-principles calculations. In this study, we attempt to clarify the sources of disagreements. The results pertaining to this chapter are published in Ref.[[65]] and figures are reproduced with permission of the publisher.

Active research on graphene[6] revealed not only numerous exceptional properties [8, 10, 9] but also have prepared a ground for the discovery of several graphene based materials. Preparation of freestanding graphene sheets with nonuniform oxygen coverage have been achieved.[66, 67] More recently the synthesis of two-dimensional hydrocarbon in honeycomb structure, so called *graphane* [41] (CH), showing diverse electronic, magnetic and mechanical properties [42, 36, 53, 68] is

reported.

According to Pauling scale F has electronegativity of 3.98, which is higher than those of C(2.55), H(2.20) and O(3.44), and hence fluorination of graphene is expected to result in a material, which may be even more interesting than both graphene oxide and CH. Before the first synthesis of graphene, fluorinated graphite has been treated theoretically. [69, 70] Owing to promising properties revealed for CH, fluorinated graphene structures are now attracting considerable interest [71, 72, 73, 74, 75, 76, 77] despite uncertainties in their chemical compositions and atomic structures. In an effort to identify the structures of fluorinated samples, previous theoretical models attempted to deduce the lowest energy structures. [69, 71] In addition, band gaps of different structures calculated within Density Functional Theory (DFT) are compared with the values revealed through specific measurements.[73, 74] However, neither the stability of proposed structures are questioned, nor underestimation of band gaps within DFT has been a subject matter. Raman spectrum by itself, has been limited in specifying $C_nF$ structures.[74]

In this part of my thesis, we first determined stable $C_nF$ structures for $n \leq 4$. Then we revealed specific properties (such as internal structural parameters, elastic constants, formation and binding energies, energy band gap and photoelectric threshold) for those stable structures as signatures to identify the derivatives probed experimentally. We placed an emphasis on fully fluorinated graphene or fluorographene (CF), in which D and G Raman peaks of bare graphene disappear after long fluorination period.[73, 74] Present study reveals that the properties, such as structural parameters, binding energy, band gap and phonon modes of various fluorinated structures are strongly dependent on the binding structure of F atoms and their composition. Some of these properties are found to roughly scale with F coverage. While the stable $C_2F$ chair structure is metallic, CF is a nonmagnetic insulator with a band gap, $E_g$, being much larger than 3 eV, i.e. a value attributed experimentally to fully fluorinated graphene. In view of the calculated diffusion constant, Raman active modes and other properties, available experimental data suggest that domains (or grains) of various $C_nF$ structures with extended and imperfect grain boundaries can coexist after fluorination process.

Hence the measured properties are averaged from diverse perfect and imperfect regions.

Our predictions are obtained from first-principles plane wave calculations[43, 44] within DFT, which is demonstrated to yield rather accurate results for carbon based materials. Calculations are performed using spin-polarized local density approximation (LDA)[47] and projector augmented wave (PAW) potentials.[46] Kinetic energy cutoff $\hbar^2|\mathbf{k}+\mathbf{G}|^2/2m$ for plane-wave basis set is taken as 500 eV. In the self-consistent potential and total energy calculations of fluorographene a set of (25x25x1) **k**-point sampling is used for Brillouin zone (BZ) integration. The convergence criterion of self consistent calculations for ionic relaxations is $10^{-5}$ eV between two consecutive steps. By using the conjugate gradient method, all atomic positions and unit cells are optimized until the atomic forces are less than 0.03 eV/Å. Pressures on the lattice unit cell are decreased to values less than 0.5 kBar. The energy band gap, which is usually underestimated in DFT, is corrected by frequency-dependent $GW_0$ calculations.[45] In $GW_0$ corrections screened Coulomb potential, W, is kept fixed to initial DFT value $W_0$ and Green's function, G, is iterated four times. Various tests are performed regarding vacuum spacing, kinetic energy cut-off energy, number of bands, **k**-points and grid points. Finally, the band gap of CF is found 7.49 eV after $GW_0$ correction, which is carried out by using (12x12x1) **k**-points in BZ, 15 Å vacuum spacing, default cut-off potential for $GW_0$, 192 bands and 64 grid points. Phonon frequencies and phonon eigenvectors are calculated using the Density Functional Perturbation Theory (DFPT).[5]

## 5.2 Structures of fluorinated graphene

Each carbon atom of graphene can bind only one F atom and through coverage (or decoration) of one or two sides of graphene, one can achieve diverse $C_nF$ structures. Uniform F coverage is specified by $\Theta = 1/n$ (namely one F adatom per $n$ C atoms), whereby $\Theta = 0.5$ corresponds to half fluorination and $\Theta = 1$ is fluorographene CF. The adsorption of a single F atom to graphene is precursor

for fluorination. When placed at diverse sites of a $(4 \times 4)$ supercell of graphene, simple F atom moves to the top site of a carbon atom and remains adsorbed there. The resulting structure is nonmagnetic and its binding energy is $E_b$=2.71 eV in equilibrium, that is a rather strong binding unlike many other adatoms adsorbed to graphene. An energy barrier, $Q_B$ =$\sim$0.45 eV, occurs along its minimum energy migration path. Our calculations related with the minimum energy path of a single F atom follow hexagons of underlying graphene. Namely, F atom migrates from the highest binding energy site, i.e. top site (on top of carbon atom) to the next top site through bridge site (bridge position between two adjacent carbon atoms of graphene). The corresponding diffusion constant for a single F atom, $D = \nu a e^{-Q_B/k_B T}$ is calculated in terms of the lattice constant, $a$ = 2.55 Å and characteristic jump frequency $\nu$ $\approx$39 THz. Experiments present evidences that energy barriers on the order of 0.5 eV would make the adatoms mobile.[74] Moreover, this energy barrier is further lowered even it is collapsed in the presence of a second F atom at the close proximity. Consequently, this situation together with the tendency towards clustering favors that $C_nF$ grains (or domains) of different $n$ on graphene can form in the course of fluorination. We note that the energy barrier for the diffusion of a single carbon adatom adsorbed on the bridge sites of graphene was calculated to be in the similar energy range. Carbon adatoms on graphene were found to be rather mobile. That energy barrier for single C adatom was found to decrease, even to collapse at the close proximity of a second adatom.[78]

In earlier theoretical studies, [69, 71, 73] the total energies and/or binding energies were taken as criteria for whether a given $C_nF$ structure exists. Even if a $C_nF$ structure seems to be in a minimum on the Born- Oppenheimer surface, its stability is meticulously examined by calculating frequencies of all phonon modes in BZ. Here we calculated phonon dispersions of most of optimized $C_nF$ structures. We found $C_4F$, $C_2F$ boat, $C_2F$ chair (See Fig. 5.1) and CF chair (See Fig. 5.2) structures have positive frequencies throughout the Brillouin zone indicating their stability.

Some of phonon branches of $C_nF$ structures (for example, CF boat) have imaginary frequencies and hence are unstable, in spite of the fact that their

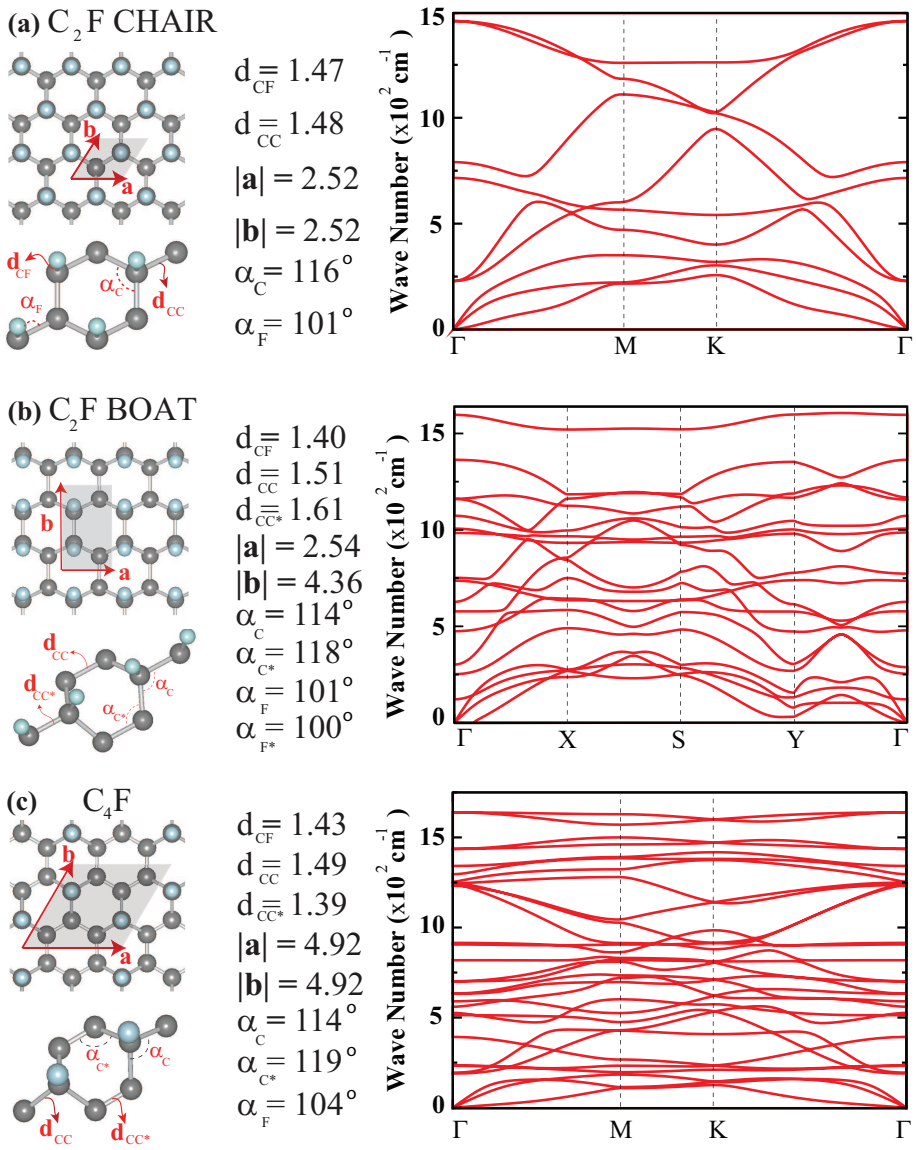


Figure 5.1: (Color online) Atomic structure and calculated phonon bands (i.e. phonon frequencies, $\Omega(\mathbf{k})$ versus wave vector, $\mathbf{k}$) of various optimized $C_nF$ structures calculated along the symmetry directions of BZ. Carbon and fluorine atoms are indicated by black (dark) and blue (light) balls, respectively. (a) $C_2F$ Chair structure. (b) $C_2F$ Boat structure. (c) $C_4F$ structure. Units are Å for structural parameters and $cm^{-1}$ for frequencies.

Table 5.1: Comparison of the calculated properties of four stable, fluorinated graphene structures (namely CF, $C_2F$ chair, $C_2F$ boat and $C_4F$) with those of graphene and CH. Lattice constant, $a = b$ ($a \neq b$ for rectangular lattice); C-C bond distance, $d_{CC}$ (second entries with slash differ from the previous one); C-X bond distance (X indicating H (F) atom for CH (CF)), $d_{CX}$; the buckling, $\delta$; angle between adjacent C-C bonds, $\alpha_C$; angle between adjacent C-X and C-C bonds, $\alpha_X$; total energy per cell comprising 8 carbon atoms $E_T$; formation energy per X atom relative to graphene, $E_f$; binding energy per X atom relative to graphene, $E_b$ (the value in parenthesis $E_{b'}$ excludes the X-X coupling); desorption energy, $E_d$ (see the text for formal definitions); energy band gap calculated by LDA, $E_g^{LDA}$; energy band gap corrected by $GW_0$, $E_g^{GW_0}$; photoelectric threshold, $\Phi$; in-plane stiffness, $C$; Poison ratio, $\nu$. All materials are treated in hexagonal lattice, except $C_2F$ boat having rectangular lattice.

| Material | $a$ ($b$) (Å) | $d_{CC}$ (Å) | $d_{CX}$ (Å) | $\delta$ (Å) | $\alpha_C$ (deg) | $\alpha_X$ (deg) | $E_g^{LDA}$ ($eV$) | $E_g^{GW_0}$ ($eV$) | $E_T$ ($eV$) | $E_f$ ($eV$) | $E_b(E_{b'})$ ($eV$) | $E_d$ ($eV$) | $\Phi$ ($eV$) | $C$ ($J/m^2$) | $\nu$ |
|---|---|---|---|---|---|---|---|---|---|---|---|---|---|---|---|
| Graphene | 2.46 | 1.42 | - | 0.00 | 120 | - | 0.00 | 0.00 | -80.73 | - | - | - | 4.77 | 335 | 0.16 |
| CH | 2.51 | 1.52 | 1.12 | 0.45 | 112 | 107 | 3.42 | 5.97 | -110.56 | 0.39 | 2.8(2.5) | 4.8 | 4.97 | 243 | 0.07 |
| CF | 2.55 | 1.55 | 1.37 | 0.49 | 111 | 108 | 2.96 | 7.49 | -113.32 | 2.04 | 3.6(2.9) | 5.3 | 7.94 | 250 | 0.14 |
| $C_2F$ chair | 2.52 | 1.48 | 1.47 | 0.29 | 116 | 101 | metal | metal | -89.22 | 0.09 | 1.7(0.9) | 1.2 | 8.6/5.6 | 280 | 0.18 |
| $C_2F$ boat | 2.54(4.36) | 1.51/1.61 | 1.40 | 0.42 | 114/118 | 100/101 | 1.57 | 5.68 | -92.48 | 0.91 | 2.5(1.6) | 2.4 | 7.9/5.1 | 286(268) | 0.05 |
| $C_4F$ | 4.92 | 1.49/1.39 | 1.43 | 0.34 | 114/119 | 104 | 2.93 | 5.99 | -87.68 | 1.44 | 3.0(2.7) | 3.5 | 8.1/5.6 | 298 | 0.12 |

structures can be optimized. The possibility that these unstable structures can occur at finite and small sizes is, however, not excluded. For stable structures, the gap between optical and acoustical branches is collapsed, since the optical branches associated with the modes of C-F bonds occur at lower frequencies. This situation is in contrast with the phonon spectrum of graphane, [36] where optical modes related with C-H bonds appear above the acoustical branches at $\sim 2900$ cm$^{-1}$.

The formation energy of fluorination is defined as $E_f = (n_{F_2}E_{T,F_2} + E_{T,Gr} - E_{T,C_nF})/n_F$ in terms of the total ground state energies of optimized structures of graphene and fluorinated graphenes at different composition, respectively, $E_{T,Gr}$, $E_{T,C_nF}$, and the total ground state energy of single carbon atom, $E_{T,C}$, of $F_2$ molecule and F atom, $E_{T,F_2}$ and $E_{T,F}$. Similarly, the binding energy of F atom relative to graphene including F-F coupling is $E_b = (E_{T,Gr} + n_F E_{T,F} - E_{T,C_nF})/n_F$ and without F-F coupling $E_{b'} = (E_{T,Gr} + E_{T,n_FF} - E_{T,C_nF})/n_F$. Here $E_{T,n_FF}$ is

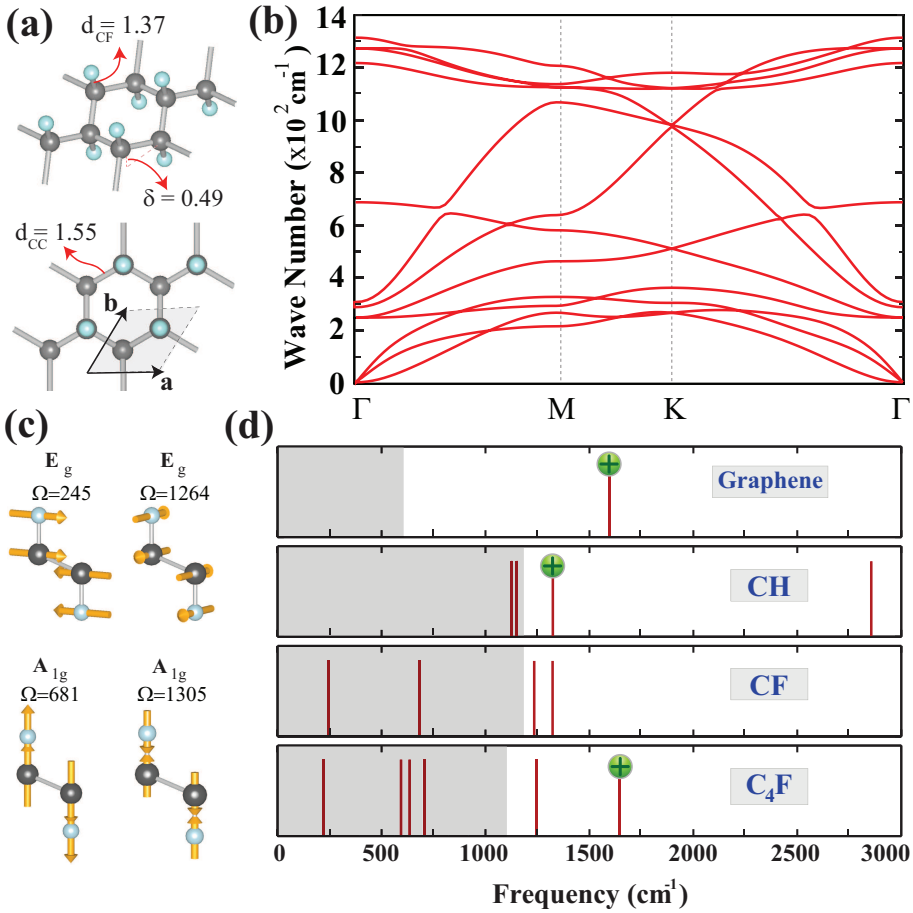


Figure 5.2: (Color online) (a) Atomic structure of fluorographene CF. $a$ and $b$ are the lattice vectors ($|a| = |b|$) of hexagonal structure; $d_{CC}$ ($d_{CF}$) is the C-C (C-F) bond distance; $\delta$ is the buckling. (b) Phonon frequencies versus wave vector $\mathbf{k}$, i.e. $\Omega(\mathbf{k})$ of optimized CF calculated along symmetry directions in BZ. (c) Symmetries, frequencies and descriptions of Raman active modes of CF. (d) Calculated Raman active modes of graphene, CH, CF and $C_4F$ are indicated on the frequency axis. Those modes indicated by "+" are observed experimentally. There is no experimental Raman data in the shaded regions. Units are Å for structural parameters and $cm^{-1}$ for frequencies.

the total energy of suspended single or double layers of F occupying the same positions as in $C_nF$. The desorption energy, $E_d$ is the energy required to remove one single F atom from the surface of $C_nF$. $n_{F_2}$ and $n_F$ are numbers of $F_2$ molecules and F atoms, respectively. The total energies are calculated in periodically repeating supercells comprising 8 carbon atoms and keeping all the parameters of calculations described above using spin-polarized as well as spin unpolarized LDA. Lowest (magnetic or nonmagnetic) total energy is used as ground state total energy.

Fluorographene (CF), where F atoms are bound to each C atom of graphene alternatingly from top and bottom sides is energetically most favorable structure. Upon full fluorination, the planar honeycomb structure of C atoms becomes buckled (puckered) and C-C bond length increases by ∼10%. At the end, while planar $sp^2$-bonding of graphene is dehybridized, the buckled configuration is maintained by $sp^3$-like rehybridization. In Table 5.1, the calculated lattice constants, internal structural parameters, relevant binding energies and energy band gaps of stable $C_nF$ structures are compared with those of bare graphene and CH.[36] Notably, internal parameters (such as $\delta$, C-C bond length) as well as lattice constants of various $C_nF$ structures vary with F coverage, $\Theta$. CF, has highest values for $E_f$, $E_b$, $E_{b'}$ and $E_d$ given in Table 5.1; those of $C_4F$ are second highest among stable $C_nF$ structures.

Since Raman spectrum can convey information for a particular structure and hence can set its signature, calculated Raman active modes of stable $C_4F$ and CF structures together with those of graphene and CH are also indicated in Fig. 5.2 (c) and (d). It is known that the only characteristic Raman active mode of graphene at 1594 $cm^{-1}$ is observed so far. [34, 35] Similarly, for CH the mode at ∼1342 $cm^{-1}$ is observed.[41] One of two Raman active modes of $C_4F$ at 1645 $cm^{-1}$ seems to be observed.[73] In compliance with the theory, [35] phonon branches of all these observed modes exhibit a kink structure. However, none of the Raman active modes of CF revealed in Fig. 5.2 has been observed yet. Raman spectroscopy in the low frequency range may be useful in identifying experimental structures.

## 5.3 Electronic Structures

Energy bands, which are calculated for the optimized $C_4F$, $C_2F$ boat, $C_2F$ chair and CF chair structures are presented in Fig. 5.3 and Fig. 5.4 structures, respectively. The orbital projected densities of states (PDOS) together with the total densities of states of these optimized structures are also presented. Analysis of the electronic structure can also provide data to reveal the observed structure of fluorinated graphene. As seen in Table 5.1, stable $C_nF$ structures have LDA band gaps ranging from 0 eV to 2.96 eV. Surprisingly, $C_2F$ chair structure is found to be a metal owing to the odd number of valance electrons in the primitive unit cell. Even if various measurements on the band gap of fluorinated graphene lie in the energy range from 68 meV[72] to 3 eV,[74] these calculated band gaps are underestimated by LDA. Incidentally, the band gaps change significantly after they are corrected by various self-energy methods. In fact, the correction using $GW_0$ self-energy method predicts a rather wide band gap of 7.49 eV for CF. The corrected band gaps for $C_2F$ boat structure and $C_4F$ are 5.68 eV and 5.99 eV, respectively. It should be noted that the $GW_0$ self-energy method has been successful in predicting the band gaps of 3D semiconductors.[79]

While predicting much larger band gap for CF, the measured band gap of $\sim$3 eV reported by Nair et al.[74] marks the serious discrepancy between theory and experiment. The character of the band structure of CF are revealed from the analysis of projected density of states as well as charge densities of specific bands in Fig. 5.4 (b). Conduction band edge consists of the antibonding combination of $p_z$-orbitals of F and C atoms. The $p_z$-orbitals of C atoms by themselves, are combined to form $\pi$-bands. The bands at the edge of the valence band are derived from the combination of C-$p_x + p_y$ and F-$p_x + p_y$ orbitals. The total contribution of C orbitals to the valence band can be viewed as the contribution of four tetrahedrally coordinated $sp^3$-like hybrid orbitals of $s$- and $p$-orbitals of C atoms. However, the deviation from tetrahedral coordination increases when $n$ increases or single side is fluorinated. As a matter of fact, the total density of states presented in Fig. 5.3 and Fig. 5.4 mark crucial differences. In this respect, spectroscopy data is expected to yield significant information regarding

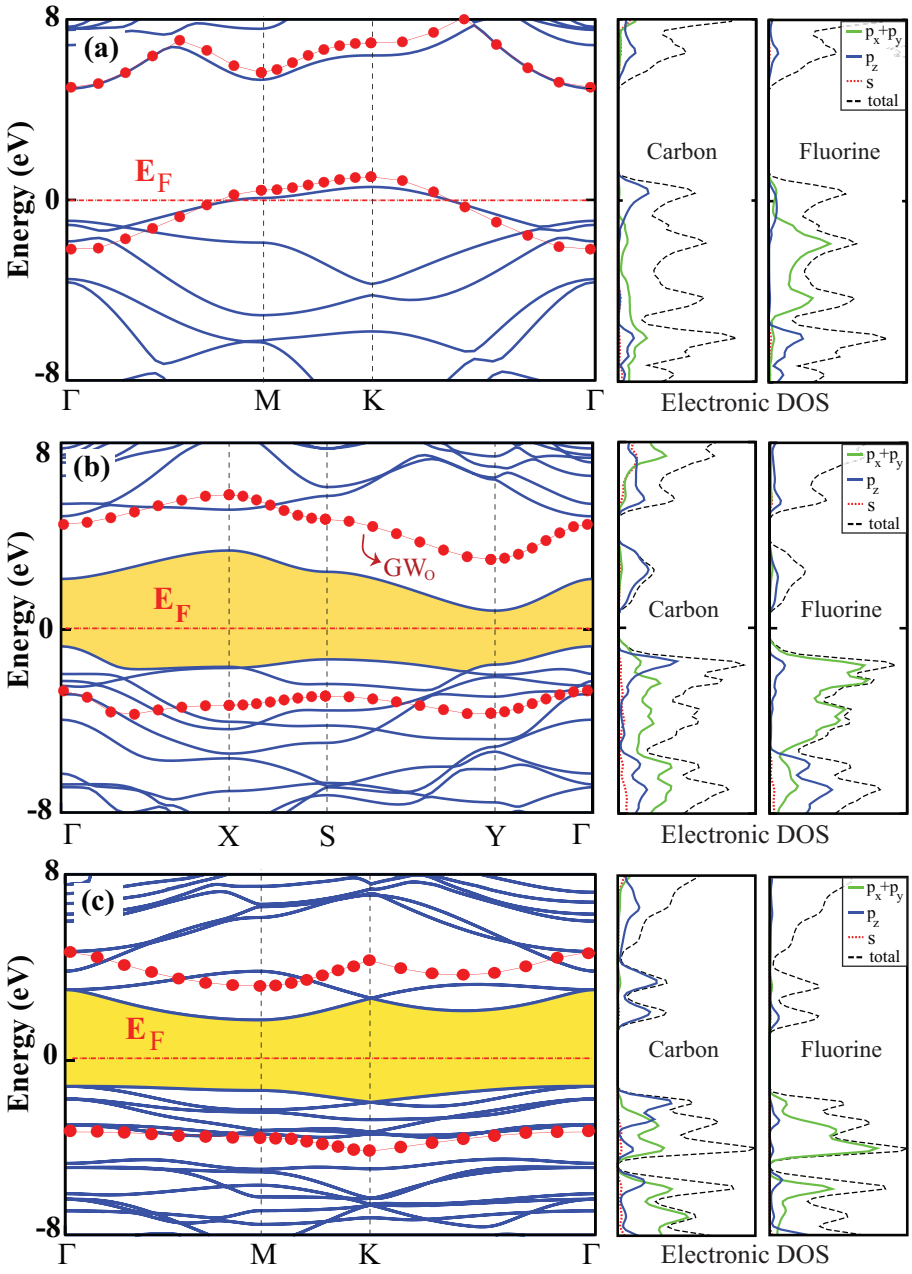


Figure 5.3: (Color online) Energy band structures of various stable $C_nF$ structures together with the orbital projected densities of states and the total densities of states (DOS). The LDA band gaps are shaded and the zero of energy is set to the Fermi level $E_F$. Total DOS is scaled to 45%. Valence and conduction band edges after $GW_0$ correction are indicated by filled/red circles. (a) $C_2F$ chair structure. (b) $C_2F$ Boat structure. (c) $C_4F$ structure.

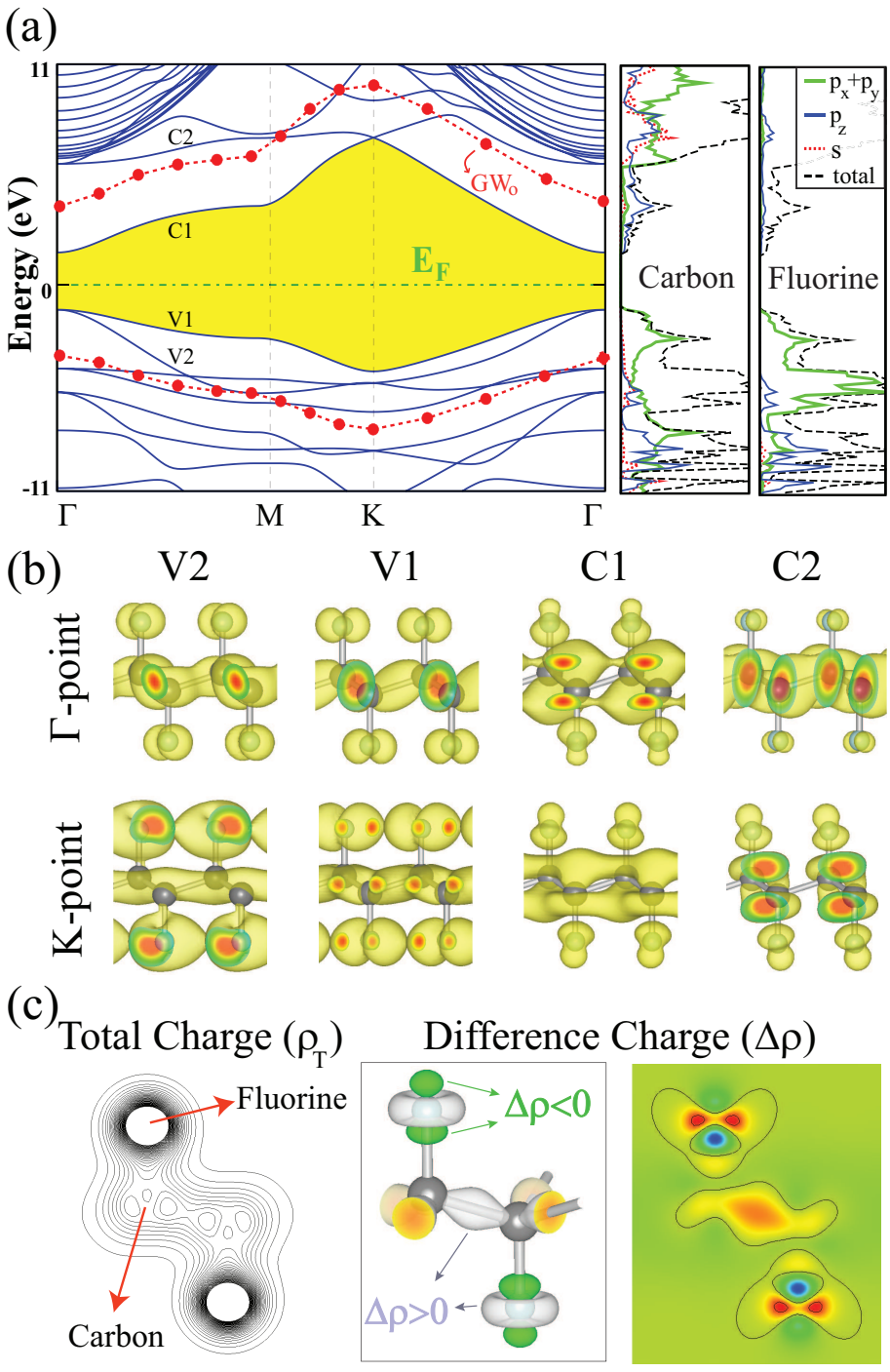


Figure 5.4: (Color online) (a) Energy band structure of CF together with the orbital projected DOS and total densities of states. The LDA band gap is shaded and the zero of energy is set to the Fermi level, $E_F$. Valence and conduction band edges after $GW_0$ correction are indicated by filled/red circles. (b) Isosurfaces of charge densities of states corresponds to first (V1), second (V2) valance and first (C1) and second (C2) conduction bands at the Γ- and $K$-points. (c) Contour plots of the total charge density $\rho_T$ and difference charge density $\Delta\rho$ in the plane passing through F-C-C-F atoms. Contour spacings are 0.03 e/Å$^3$.

the observed structures of fluorinated graphenes.

The contour plots of the total charge density, $\rho_T$, in the F-C-C-F plane suggests the formation of strong covalent C-C bonds from the bonding combination of two C-$sp^3$ hybrid orbitals. The difference charge density, $\Delta\rho$ (which is obtained by subtracting the charges of free C and free F atoms situated at their respective positions in CF), indicates charge transfer to the middle of C-C bond and to F atom, revealing the bond charge between C atoms and ionic character of C-F bond. However, the value of charge transfer is not unique, but diversifies among different methods of analysis.[80, 81] Nevertheless, the direction of calculated charge transfer is in compliance with the Pauling ionicity scale and is corroborated by calculated Born effective charges, which have in-plane ($\|$) and out-of-plane ($\perp$) components on C atoms, $Z^*_{C,\|} = 0.30$, $Z^*_{C,\perp} = 0.35$ and on F atoms $Z^*_{F,\|} = -0.30$, $Z^*_{F,\perp} = -0.35$.

Finally, we note that perfect CF is a nonmagnetic insulator. However, a single isolated F vacancy attains a net magnetic moment of 1 Bohr magneton ($\mu_B$) and localized defect states in the band gap. Creation of an unpaired $\pi$- electron upon F vacancy is the source of magnetic moment. However, the exchange interaction between two F-vacancies calculated in a (7x7x1) supercell is found to be nonmagnetic for the first nearest neighbor distances due to spin pairings. Similar to graphane,[36, 53] it is also possible to attain large magnetic moments on F-vacant domains in CF structures.

## 5.4 Elastic Properties of CF

Having analyzed the stability of various $C_nF$ structures with $n$ =1,2 and 4, we next investigate their mechanical properties. The elastic properties of this structure can conveniently be characterized by its Young's modulus and Poison's ratio. However, the in-plane stiffness $C$ is known to be a better measure of the strength of single layer honeycomb structures, since the thickness of the layer $h$ cannot be defined unambiguously. Defining $A_0$ as the equilibrium area of a $C_nF$ structures,

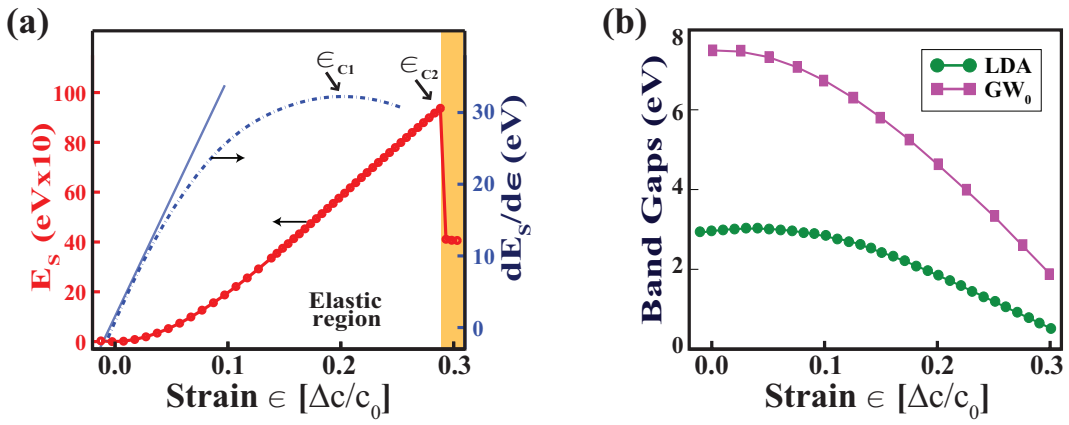


Figure 5.5: (Color online) (a) Variation of strain energy and its first derivative with respect to the uniform strain $\epsilon$. Orange/gray shaded region indicates the plastic range. Two critical strains in the elastic range are labeled as $\epsilon_{c1}$ and $\epsilon_{c2}$. (b) Variation of the band gaps with $\epsilon$. LDA and $GW_0$ calculations are carried out using 5x5 supercell having the lattice parameter of $c_0$=5a, and $\Delta c$ is its stretching

the in-plane stiffness is obtained as $C = (\delta E_s^2/\delta\epsilon^2)/A_0$, in terms of strain energy $E_s$ and uniaxial strain $\epsilon$.[68] The values of in-plane stiffness $C$, and Poisson's ratio $\nu$, calculated for stable $C_nF$ structures are given in Table 5.1 together with the values calculated for graphene and graphane. For example, the calculated values of CF are $C$=250 J/m$^2$ and $\nu$=0.14. It is noted that $C$ increases with $n$. For CF (i.e. $n = 1$), the in-plane stiffness is close to that calculated for CH. It appears that either the interaction between C-F bonds in CF (or the interaction between C-H bonds in CH) does not have significant contribution to the in-plane stiffness. The main effect occurs through dehybridization of $sp^2$ bonds of graphene through the formation C-F bonds (or C-H bonds).

A value of Young's modulus around 0.77 $TPa$ can be calculated by estimating the thickness of CF as $h$=3.84 Å, namely the sum of the thickness of graphene (3.35 Å) and buckling, $\delta$ (0.49 Å). This value is smaller, but comparable with the value proposed for graphene, i.e. $\sim$ 1 $TPa$. Here the contribution of C-F bonds to the thickness of CF is neglected, since the interaction between C-F bonds has only negligible effects on the strength of CF.

In Fig. 5.5 the variation of strain energy $E_s$ and its derivative, $\delta E_s/\delta\epsilon$, with strain, $\epsilon$ are presented in both elastic and plastic regions. Two critical strain

values, $\epsilon_{c_1}$ and $\epsilon_{c_2}$, are deduced. The first one, $\epsilon_{c_1}$, is the point where the derivative curve attains its maximum value. This means that the structure can be expanded under smaller tension for higher values of strain. This point also corresponds to phonon instability[68] where the longitudinal acoustic modes start to become imaginary for $\epsilon > \epsilon_{c_1}$. The second critical point, $\epsilon_{c_2}$ ($\simeq 0.29$), corresponds to the yielding point. Until this point the honeycomb like structure is preserved, but beyond it the plastic deformation sets in. We note that for $\epsilon_{c_1} < \epsilon < \epsilon_{c_2}$ the system is actually in a metastable state, where the plastic deformation is delayed. Under the long wavelength perturbations, vacancy defects and high ambient temperature $\epsilon_{c_2}$ approaches to $\epsilon_{c_1}$. In fact, our further molecular dynamics simulations show that $\epsilon_{c_2} \rightarrow 0.17$ at 300K and to 0.16 at 600K. In the presence of periodically repeating F-vacancy and C+F-divacancy, the value of $\epsilon_{c_2}$ is also lowered to 0.21 and 0.14, respectively. Apart from phonon instability occurring at high $\epsilon$, the band gap is strongly affected under uniform expansion. In Fig. 5.5(b) we show the variation of LDA and $GW_0$- corrected band gaps under uniform expansion. The LDA gap slightly increases until $\epsilon = 0.05$ and then decreases steadily with increasing $\epsilon$. The $GW_0$-corrected band gap essentially decreases with increasing strain. For example, its value decreases by 38% for $\epsilon = 0.20$.

Present analysis of fluorinated graphenes shows that different $C_nF$ structures can form at different level of F coverage. Calculated properties of these structures, such as lattice parameter, $d_{CC}$ distance, band gap, density of states, work function, in plane stiffness $C$, Poisson's ratio and surface charge, are shown to depend on $n$ or coverage $\Theta$. Relevant data reported in various experiments do not appear to agree with the properties calculated any one of the stable $C_nF$ structures. This finding lets us to conclude that domains of various $C_nF$ structures can form in the course of the fluorination of graphene. Therefore, the experimental data may reflect a weighted average of diverse $C_nF$ structures together with extended defects in grain boundaries. In this respect, imaging of fluorinated graphene surfaces by scanning tunneling and atomic force microscopy, as well as x-ray photoemission spectroscopy is expected to shed light on the puzzling inconsistency between theory and experiment.

Finally, our results show a wide range of interesting features of $C_nF$ structures. For example, a perfect CF structure as described in Fig. 5.2 is a stiff, nonmagnetic wide band gap nanomaterial having substantial surface charge, but attains significant local magnetic moment through F-vacancy defects. Moreover, unlike graphane, half fluorinated graphene with only one side fluorinated is found to be stable, which can be further functionalized by the adsorption of adatoms to other side. For example, hydrogen atoms adsorbed to other side attain positive charge and hence permanent transversal electric field, which can be utilized to engineer electronic properties.

# Chapter 6

# Chlorinated Graphene

In this part of the thesis, first principles calculations performed to study the interaction of chlorine atoms with graphene and to predict the existence of possible chlorinated graphene derivatives. Differing from hydrogen and fluorine adatoms, while the binding of single chlorine atom to graphene is significant, its migration on the surface of perfect graphene takes place almost without barrier. We also found that strong Cl-Cl coupling in one sided high chlorine coverage of graphene hinders the formation of boat, armchair and zigzag configuration. While the bonding of single chlorine atom leads to ionic bonding and negligible local distortion in the planar graphene, full chlorine coverage (chlorographene) where one chlorine atom is bonded alternatingly to each carbon atom from different sides gives rise to the buckling and covalent $sp^3$-bonding. We found chlorographene a graphene derivative, whose phonon and electronic energy structure largely deviate from those of graphene. Energy optimization and phonon calculations indicate that the chair configuration of fully chlorinated graphene (chloragraphene) is energetically most favorable and stable structure. It is a semiconductor with 1.2 eV direct band gap, which can be tuned by applied uniform strain. The results pertaining to this chapter submitted for publication in Physical Review B in Ref.[[82]].

## 6.1 Motivation

The discovery of graphene[6, 8] has started enormous research activity in the field of graphene-based nanoscale devices. Although graphene is one of the most mechanically strong material having a wide range of extraordinary properties, [6, 8, 10] practical device applications are limited by it's metallic behavior and extreme sensitivity to surface adsorbates.

Efforts to manufacture chemically modified graphene composites with tailored electronic, optical, and chemical properties present an exciting new direction in graphene research. In particular, band gap engineering of graphene through chemical modification such as oxygenation,[66] and hydrogenation[41, 55, 36, 53, 68, 83] is appealing for electronic applications, since the scalable fabrication of graphene-based devices without disturbing the strong honeycomb lattice is made possible. However, due to the complex atomic structure of grapheneoxides (GOs) and thermal instabilities of hydrogenated graphenes (CHs) even at low temperatures,[41, 55, 36] search for the novel graphene-based materials is still continuing.

Over the past three years experimental[74, 72, 84, 76] and theoretical[75, 77, 65] studies have demonstrated that chemical conversion of graphene to fluorographene (CF) is possible. In addition to early studies on the atomic composition and band structure of fluorocarbon materials,[69, 70] it was reported that the monolayer CF has quite different vibrational spectra and Raman characteristics as compared to hydrogenated graphene analogues.[75] We also investigated the electronic and elastic properties of possible fluorinated graphene materials and attempted to clarify the discrepancy between theoretical and experimental results.[65] Easy synthesis, high-quality insulating behavior and extraordinary mechanical strength of fluorographene (CF) have inspired intense research on other halogen decorated graphene derivatives.

In addition to three known derivatives of graphene: GO, CH and CF, the successful synthesis of chlorinated graphene was also achieved very recently.[85] It is experimentally demonstrated that nondestructive and patternable conversion of graphene is possible by using photochemical chlorination technique.[85] To our

knowledge there is only a few studies[85, 77, 86, 87] on the chlorinated graphene and comprehensive research on its characteristic properties is sparse.

In this thesis we present a detailed analysis of chlorination of graphene. Although the possibility of covering graphene surfaces with chlorine atoms has been reported, analysis of structural, electronic and magnetic properties as a function of Cl coverage is lacking. Our main motivation is to reveal how the properties of graphene are modified with Cl coverage. To this end we investigated the chlorination of graphene starting from single Cl adsorption to full coverage leading to chlorographene, namely CCl. At low coverage with diminishing Cl-Cl coupling, the binding of Cl to graphene is significant, but adsorbed Cl atoms migrate on the surface of graphene practically without an energy barrier. We found the non bonding chair conformation of chlorographene (CCl), which were examined earlier[77, 86] unstable. On the other hand, the chair conformation of the chlorographene, which is found to be most favorable energetically among various structures, is stabilized upon the buckling of graphene. It is a non-magnetic semiconductor with 1.2 eV direct band gap. Our results reconcile the discrepancy between earlier an experimental study[85] obtaining semiconducting properties upon the chlorination of graphene and theoretical studies predicting metallic state.[77]

To investigate mechanical, electronic magnetic properties of chlorinated graphene chlorographene we carried out first-principles density functional theory (DFT) calculations within the local density approximation (LDA)[47] for the exchange-correlation functional using projector augmented wave (PAW) potentials.[46] For the sake of comparison, we also performed calculations with Generalized Gradient Approximation[88](GGA) together with Van der Waals (vdW) correction, (GGA+vdW)[89] Numerical calculations are performed using VASP,[43, 44] Kinetic energy cutoff, $E_{cut} = \hbar^2|\mathbf{k}+\mathbf{G}|^2/2m$, for plane-wave basis set is taken as 500 eV. A vacuum spacing of at least 15 Å is placed between adjacent layers to hinder the layer-layer interactions. The convergence criterion of self consistent calculations for ionic relaxations is $10^{-5}$ eV between two consecutive steps. Structural optimizations were performed using a conjugate gradient algorithm until the Hellmann-Feynman forces on all atoms are less than 0.03 eV/Å.

Pressures on the lattice unit cell are decreased to values less than 1.0 kBar. The adsorption of a single Cl atom to graphene surface is treated using the supercell geometry, where single Cl is adsorbed to each (4x4) supercell. To minimize vacancy-vacancy interaction in the study of defects, relatively larger supercells, namely (6x6) graphene supercell is used. In the self-consistent potential and total energy calculations using a (4x4) supercell of clorographene, a set of (13x13x1) **k**-point sampling is used for Brillouin zone (BZ) integration. The sampling of BZ is then scaled according to the size of the supercell. Ground state electronic structures are calculated by applying a dipole correction to eliminate the artificial electrostatic field between periodic supercells. For the charge transfer analysis, the effective charge on atoms are obtained by Bader method.[80]

The stabilities of structures having various Cl coverage are examined by the calculation of phonon frequencies for **q**-wave vectors over BZ by using both small displacement method (SDM)[4] and density functional perturbation theory (DFPT).[5] We used 196-atom supercell of chlorographene, **q**-point sampling grid of 3x3x1 and 0.01 Å displacements in calculations using SDM. DFPT part of the phonon calculations were performed by using 6x6x1 grid of **q**-points for chlorographene unitcell. A given structure considered stable, if vibration frequencies are positive for all **q**-points.

The energy band gap, which is usually underestimated by DFT, is corrected by frequency-dependent $GW_0$ calculations.[45] In $GW_o$ corrections screened Coulomb potential W, is kept fixed to initial DFT value $W_o$ and Green's function G, is iterated four times. Finally, the band gap of CCl is calculated by using (12x12x1) **k**-points in BZ, 20 Å vacuum spacing, default cut-off potential for $GW_o$, 160 bands and 64 grid points.

The binding energy of a single adatom X (X=H, F, Cl) to the graphene supercell is calculated according to the expression, $E_b = E_T[Gr] + E_T[X] - E_T[Gr+X]$, in terms of the ground state total energies of bare graphene $E_T[Gr]$, free X atom $E_T[X]$, and X adsorbed to graphen $E_T[Gr+X]$. Accordingly, $E_b > 0$ for a bound state. Similarly the formation energy per adatom for the coverage of graphene

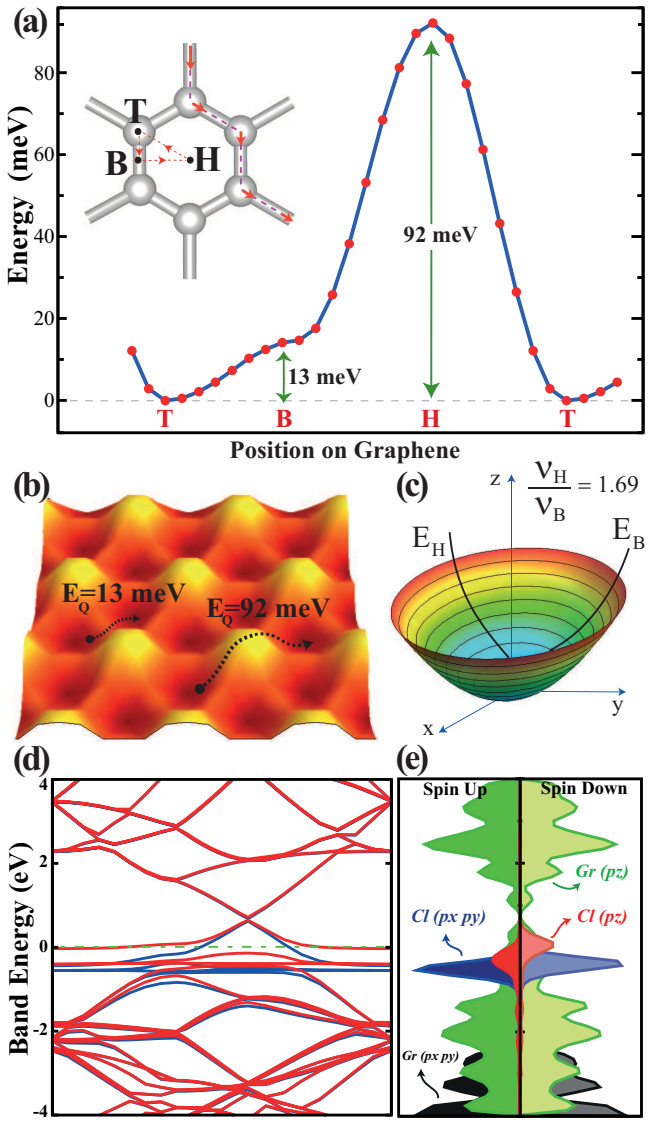


Figure 6.1: (Color online) (a) Variation in energy for a single Cl adatom migrating along the path Top(T)- Bridge(B)-Hollow(H)-Top sites on a hexagon graphene in a (4x4) supercell. At each point on the energy curve, $x$- and $y$-positions adsorbed Cl atom are fixed, its $z$-height, as well as positions of all C atoms in the (4x4) supercell are optimized by minimizing total energy and atomic forces. Zero of energy is set to the energy of T-site. The diffusion path with the lowest energy barrier of $Q$=13 meV between two adjacent T-sites are marked with thick red/ dashed lines. (b) Energy landscape of a single Cl adatom adsorbed to graphene. Dark (light) colors represents the top (hollow) sites. (c) Potential energy contour plots of Cl atom adsorbed to the T-site. The calculation of jump frequency of Cl atom $\nu$, is obtained from this plot. (d) Band structure of a single Cl adsorbed to each (4x4) supercell of graphene and corresponding total (TDOS) and orbital decomposed (PDOS) densities of states. The zero of band energy is set to the Fermi level. Up-spin and down-spin bands are colored with blue and red, respectively.

by adatom X (i.e. X=H hydrogenation; X=fluorination; X=Cl chlorination processes) relative to $X_2$ molecule is defined as $E_f = (n_{X_2}E_T[X_2]+E_T[Gr]-E_T[Gr+X]/n_X$, where $E_T[X_2]$ is the ground state total energy of $X_2$ molecule. $n_{Cl}$ ($n_{Cl_2}$) is the number of Cl atoms ($Cl_2$ molecules) per supercell. For an exothermic process $E_f > 0$. The cohesive energy of graphene fully covered with X, CX relative to free C and X atoms is defined as $E_{coh} = 2E_T[X] + 2E_T[C] - E_T[CX]$, where $E_T[CX]$ is the total ground state energy (per unit cell) of CX. By definition $E_{coh} > 0$ indicates binding relative to individual constituent atoms.

## 6.2 Adsorption of Single Chlorine

Understanding of the adsorption process of a single Cl adatom on graphene is essential for the investigation of its chlorinated graphene derivatives. A single Cl atom adsorbed to graphene is represented by a system where a single Cl adsorbed to each (4x4) supercell. Based on the analysis discussed in the next section we found the size of (4x4) supercell is sufficient to approximately discard the Cl-Cl coupling. According to the Pauling scale of electronegativity (H: 2.20, C: 2.55, Cl: 3.16 and F: 3.98) the binding of Cl atoms to graphene can be expected to be stronger than that of hydrogen adatoms (0.98 eV) and weaker than the fluorine adatoms (2.71 eV). Three different adsorption sites can be foreseen for the adsorption of Cl on graphene as described in Fig. 6.1. These are the hollow (H) site above the center of hexagon, the top (T) site on top of C atoms, the bridge (B) site above the center of C-C bonds. Among these sites, the strongest binding of single Cl to graphene is attained at T-site with a binding energy of $E_b$=1.10 eV (GGA+vDW value 1.16 eV). The length of Cl-C bond is found to be $d_Cl - C$=2.54 Å. The binding energy of an isolated $Cl_2$ molecule is calculated to be 3.58 eV. Then the adsorption of chlorine on graphene is an endothermic process and hence it can be achieved by, for example, the assistance of light absorption.[85]

The variation of the energy of adsorbed Cl atom at the symmetry points and along the symmetry directions are shown in Fig. 6.1 (a). Using this energy

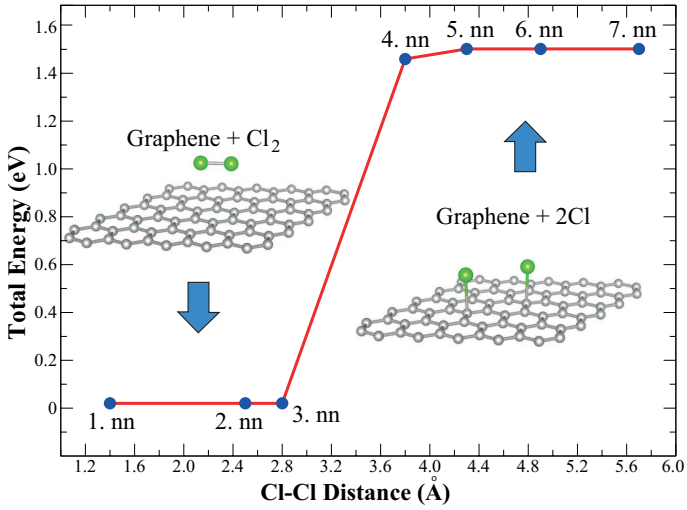


Figure 6.2: (Color online) The interaction energy between two Cl atoms adsorbed to the same side of a (6x6) supercell of graphene. The zero of energy is set to the energy of $Cl_2$ plus graphene. nn denotes the neatrest neighbor in graphene lattice

curve we reveal the energy barriers to be overcame by the adsorbate migrating or diffusing on the surface of graphene. The minimum energy barrier occurs at B-site between two adjacent T-site. The relevant energy barriers are shown on the calculated energy landscaping presented in Fig. 6.1. This analysis suggests that a diffusing Cl atom can take a path of minimum energy barrier above the edges of hexagon from T-site to T-site through the barrier of $Q$=13 meV at B-site. We note that this barrier is very low and allows Cl atom to migrate on the surface of graphene as if it rolls along the edges of hexagon. This is a remarkable situation, where the migration or diffusion of Cl occurs with almost no barrier, but it remains bound to the surface. This property of Cl adatom on graphene heralds number of possible applications, such as superlow sliding friction, sensors and devices for energy harvesting.[90] The binding energy of an isolated $Cl_2$ molecule is calculated to be 3.58 eV. Then the adsorption of chlorine on graphene is an endothermic process and hence it can be achieved by, for example, the assistance of light absorption.[85]

The diffusion constant at a given temperature can be obtained from a simple

expression, $D = \nu a^2 exp(-Q/k_B T)$ in terms of energy barrier $Q$, lattice constant $a$ and the characteristic jump frequency $\nu$. The characteristic jump frequency can be deduced from the potential energy plot in Fig. 6.1 (c) to be $\nu_{T\to B}$=0.97 and $\nu_{T\to H}$=1.68 THz. Using these values the diffusion constant at T=300 K (600 K) is calculated for the barrier $Q$=13 meV to be $D$=3.57 (4.57) $cm^2/s$.

When single Cl is adsorbed to graphene, 0.44 $e$ is transferred from graphene to Cl adatom according to Bader analysis.[80] Analysis of charge density indicates an ionic character for the Cl-C bond. However, As we will discuss in the next section, charge transfer from C to Cl and hence the character of the bonding changes in two sided adsorption. The negative charge on Cl induces a dipole moment of $\mathbf{p}$=0.67 $e\cdot$ Å between for graphene uniformly covered with Cl. Work function of bare graphene which is 4.49 eV increases to 6.53 eV upon Cl adsorption.

While single Cl adatom on the surface of graphene can be viewed as an impurity leading to localized (or resonance) states, our model representing the adsorption using a (4x4) superlattice gives rise to an energy band structure, where dispersion of bands related with adsorbate can be taken as the measure of adsorbate-adsorbate coupling. The band structure of a single Cl adsorbed to each (4x4) supercell of graphene presented in Fig. 6.1 (d) has filled chlorine states appearing as flat bands. Because of 7 valence electrons and hence a single unfilled $3p$ orbital occurring below the Fermi level $E_F$ of graphene, Cl adsorbed graphene is metallized and becomes magnetic with $\mu$=0.56 $\mu_B$ due to broken spin degeneracy. The linearly crossing bands of bare graphene is raised above $E_F$. Since the trigonal symmetry is conserved even after the adsorption of Cl, the crossing bands do not open a gap. The orbital decomposed density of states in Fig. 6.1 (e) show that the flat bands below $E_F$ are derived mainly from Cl-$3p_x$ and Cl-$3p_y$ orbitals. We also examined the band structure of single Cl adsorbed to (5x5) and (6x6) supercells. Except the band folding and slightly enhanced flatness of bands originating from adsorbate, the overall features, in particular the magnetic moments were unchanged. We therefore conclude that a Cl adsorbed to each (4x4) supercell can mimic successfully the single Cl adsorbate on a graphene surface.

## 6.3 Coverage of Graphene by Chlorine Adatoms

The Cl coverage is defined as the ratio of the number of Cl atoms $N_{Cl}$ to the number of carbon atoms $N_C$ in a supercell; namely $\Theta = N_{Cl}/N_C$. The interaction between two adsorbed Cl as a function of their separation is important to understand the coverage dependent properties and stability of Cl covered graphene. To this end we consider two Cl atoms adsorbed to the (6x6) supercell of graphene and calculate the total energies as a function of the separation between them. Chlorine atoms are placed at specific adsorption sites by fixing their $x$- and $y$-coordinates, but their $z$-coordinates, as well as the positions of other C atoms in the supercell are relaxed. In Fig. 6.2 we show how the Cl-Cl interaction changes with their separation. The Cl-Cl coupling is practically negligible when their separation greater or equal to 3.6 Å corresponding to fourth nearest neighbor. For smaller separations corresponding to third nearest neighbor separation of graphene, they form $Cl_2$ molecule and desorb from graphene surface, since Cl-Cl interaction energy becomes stronger than the sum of the binding energies of two Cl atoms to graphene (2.20 eV). Accordingly, the gain of energy through the formation of $Cl_2$ is 1.26 eV per molecule. This explains also why chlorination of graphene is endothermic. There is a weak VdW interaction between bare graphene and $Cl_2$ molecule. The maximum interaction of 144 meV occurs when the molecule is parallel to a C-C bond and 3 Å above it.

Next we examine how the electronic structure changes with one sided uniform coverage. In Fig. 6.3 we show the band structures calculated for single Cl atom adsorbed to ($nxn$) supercell for $n$=2,3,5 and 6. Here $n$=2 and $n$=3 correspond to $\Theta$=0.125 and 0.056. The phonon calculations for these two coverage values are found stable, since the frequencies phonon modes are positive for any **k**-point in BZ. The smallest separation between Cl atoms is larger than the threshold distance of 2.8 Å even for $\Theta$=0.125. We see that with increasing $\Theta$ the dispersion of Cl bands increases and the linearly crossing bands start to split due to increasing Cl-Cl coupling and breaking of trigonal symmetry. The magnetic moments also increases with coverage, since the splitting of spin-up and spin down bands increases. We found $\mu$=0.68 $\mu_B$ and $\mu$=0.64 $\mu_B$ for $\Theta$=0.125 and 0.556,

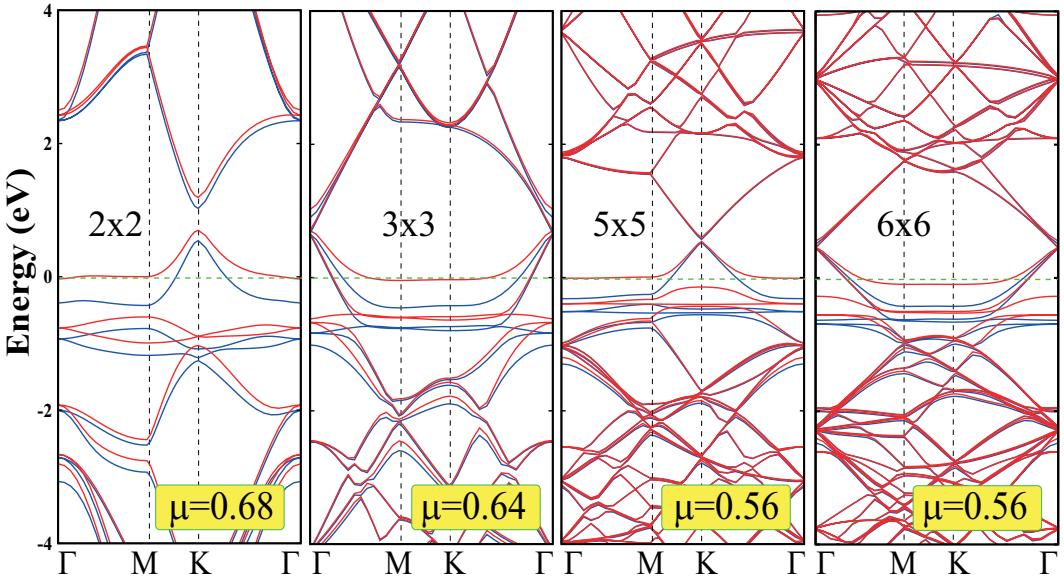


Figure 6.3: (Color online) Energy band structure of a single Cl atom adsorbed to each ($n$x$n$) supercell of graphene for $n$=2,3,5 and 6, which correspond to the one-sided uniform coverage $\Theta = 1/2n^2$. For $n \geq 2$ the coupling between adjacent adsorbates is not sufficient to form $Cl_2$ molecule. Whereas for $n = 1$ (or $\Theta$=0.5) the coupling is significant and form $Cl_2$. The units of magnetic moments $\mu$ is Bohr magneton per ($n$x$n$) supercell.

respectively. On the other hand, a single Cl adsorption to each (1x1) unit cell of graphene (which corresponds to $\Theta$=0.5) is unstable due to Cl-Cl distance smaller than 2.86 Å. Since the uniformly chlorinated graphene is found to be metallic for any coverage studied here, the experimental studies measuring a band gap of ∼0.05 eV should correspond to two sided coverage.

To understand the formation of chlorinated domains on graphene, and hence to analyze the kinetics of Cl coverage, we examined the adsorption of second Cl atom at different sites at the close proximity of the first one in (4x4) supercell. When a Cl is placed on top of a carbon atom, second Cl can be adsorbed on six relevant sites on the hexagonal carbon ring as shown in Fig. 6.4.

Among the various possible cases, the ortho top-bottom arrangement is the most favorable one. While adsorption of a single Cl atom yields 0.05 Å buckling

of graphene lattice, in ortho top-bottom configuration, $sp^3$ type bonding occurs with 0.46 Å buckling between nearest C atoms. In Fig. 6.4(b) the contour plots of total charge density on the planes passing through the bonds clearly explain the ionic Cl-C bond formed by the adsorption of single Cl and mainly covalent $sp^3$-bonding of ortho top-bottom configuration. While the charge density between Cl and C atoms is very low in the former, the bond charge is enhanced in the latter. As a manifestation of the differences between two types of bonds we compare their binding energies and lengths. While the bond length and binding energy of the single Cl-C bond are $d$=2.54 Å and $E_b$=1.10 eV, respectively, the bond length and binding energy are $d$=1.90 Å and $E_b$=1.71 eV per bond, respectively. The binding energies per bond in the case of para and meta top-bottom configurations are $E_b$=1.29 eV and $E_b$=1.41 eV, respectively.

The situation is however different for one sided (top-top) configurations. For the three one sided configuration, namely ortho, para and meta top-top configurations in Fig. 6.2 the Cl-Cl distances are within the third neighbors. Owing to the strong Cl-Cl coupling, formation of $Cl_2$ molecule is favorable energetically. Accordingly, unlike the half fluorinated graphene[65] ($C_2F$), densely one-sided chlorinated graphene with the coverage $\Theta$=0.5, namely $CCl_2$ cannot be realized.

Next, we concentrate on the chemical conversion of graphene to a fully chlorinated graphene structure ($\Theta$=1.0), called chlorographene. In addition to well-known boat and non bonding chair conformations one can also consider zigzag and armchair stoichiometric chlorographene configurations shown in Fig. 6.5. Here, boat, nonbonding chair and zigzag conformations are treated using (2x2) supercell; a (4x4) supercell is required for the armchair conformations. As a consequence of the strong Cl-Cl interaction, boat, zigzag and armchair configurations of Cl atoms cannot remain stable on graphene. As for the nonbonding conformations, where Cl atoms are placed at the T-site alternatingly at both side of graphene, earlier theoretical studies[77, 86] have reported metallic behavior and high cohesive energy. Even if the structure optimization using conjugate gradient method using the unit cell of graphene finds the nonbonding chair structure stable, present study reveals a large expansion of lattice from 2.46 Å to 2.53 Å weak attractive interaction of 50 meV per cell between graphene and Cl

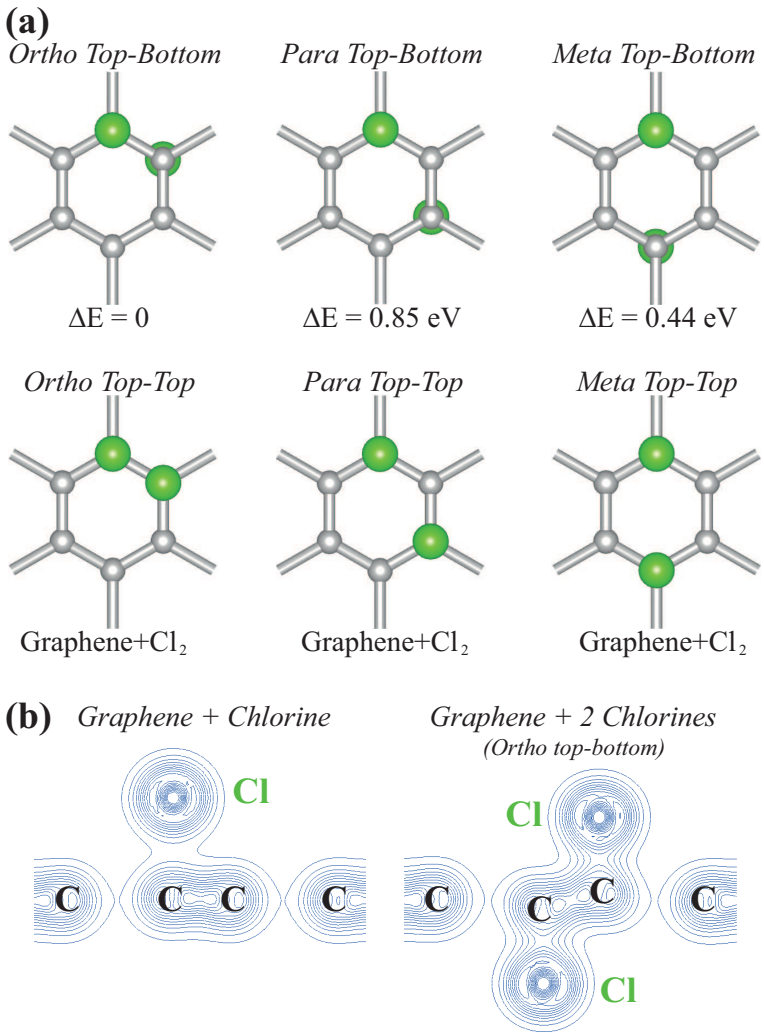


Figure 6.4: (Color online) (a) The atomic structure two Cl atoms adsorbed to a (4x4) supercell of graphene. In three different configuration illustrated by top panels, namely ortho top-bottom, para top-bottom and meta top-bottom two adsorbed Cl atoms are stable. $\Delta E$ indicates their energies relative to the total energy of the ortho top-bottom configuration. Double sided adsorption imposes a local buckling in planar graphene. Three one-sided configurations, ortho top-top, para top- top and meta top-top are not allowed; Cl atoms cannot be bound to graphene, they rather form $Cl_2$ molecule. (b) Contour plot of the total charge density of a single Cl-C bond and two Cl-C bonds in ortho top-bottom configuration. Contours spacings between $0.025e/Å^3$ and 1.0 $e/Å^3$ are 0.025 $e/Å^3$. The Cl-C bonds of ortho top-bottom configuration is reminiscent of the bonds formed from $sp^3$ hybridization, where C atoms are locally buckled and bond charges are accumulated between Cl and C atoms indicating a covalent character. Whereas the single Cl-C bond is ionic with minute local buckling of graphene.

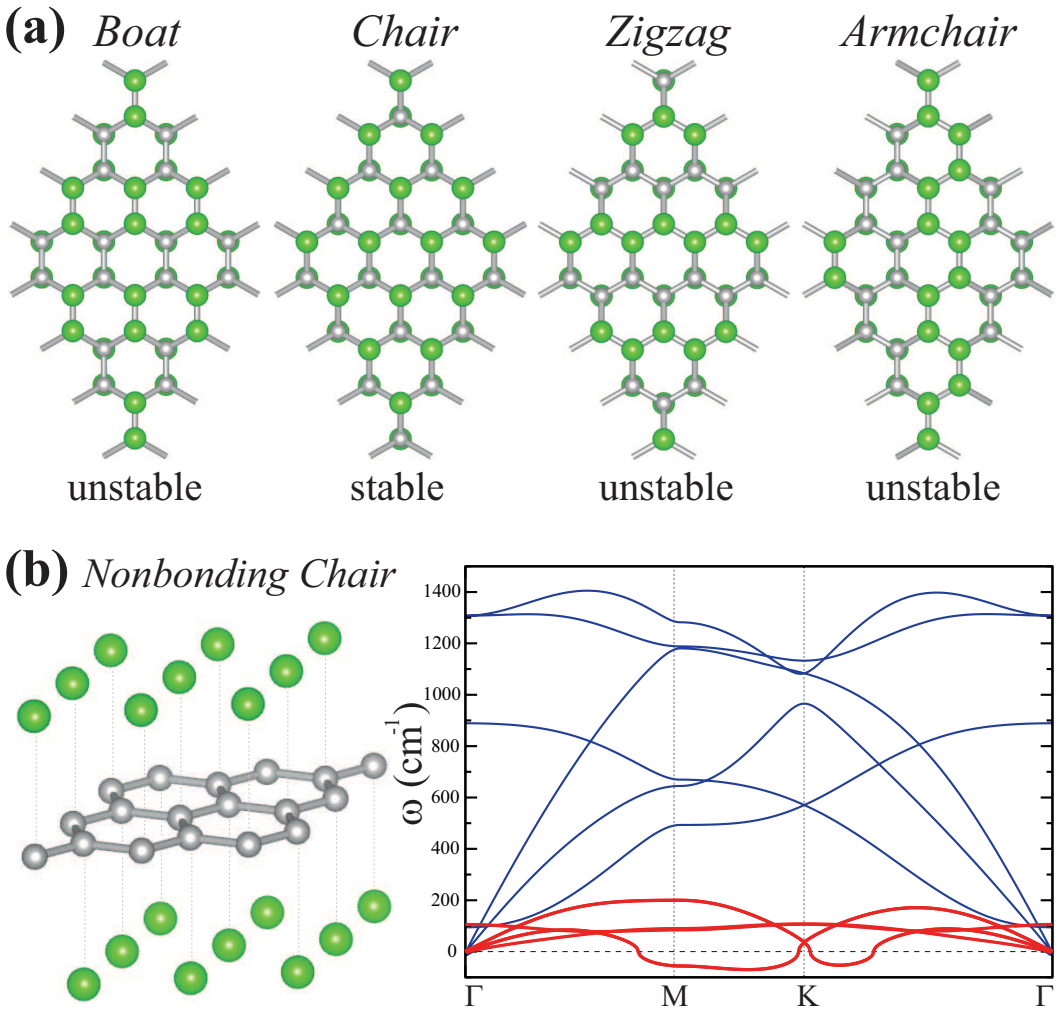


Figure 6.5: (Color online) (a) Atomic structures of boat, nonbonding chair, zigzag and armchair conformations. Large green and small gay balls represent Cl and C atoms. (b) Side view of nonbonding chair conformation and its calculated phonon dispersion curves. Low frequency phonon modes shown by red lines are related to adsorbed Cl atoms. These modes have imaginary frequencies and hence they are unstable.

Table 6.1: Calculated values for CX structures (where X=H,F,Cl); lattice constant ($a$), C-C distance ($d_{CC}$), C-X distance ($d_{CX}$), thickness of the layer ($t$), photoelectric threshold ($\Phi$), charge transfer from C to X ($\Delta\rho$), cohesive energy per unit cell ($E_{coh}$), formation energy ($E_f$), desorption energy of a single X atom from the CX surface ($E_{des}$), direct band gap ($E_g$), band gap corrected with $GW_o$ $E_g^{GW_o}$ , in-plane stiffness ($C$), Raman active modes.

| Material (CX) | $a$ Å | $d_{CC}$ Å | $d_{CX}$ Å | $t$ Å | $\Phi$ $eV$ | $\Delta\rho$ $e$ | $E_{coh}$ $eV$ | $E_f$ $eV$ | $E_{des}^X$ $eV$ | $E_g$ $eV$ | $E_g^{GW_o}$ $eV$ | $C$ $J/m^2$ | **R**-*active Modes* $cm^{-1}$ |
|---|---|---|---|---|---|---|---|---|---|---|---|---|---|
| Graphene | 2.46 | 1.42 | - | - | 4.49 | - | -17.87 | - | - | - | - | 335 | 1600 |
| CH | 2.51 | 1.52 | 1.12 | 2.68 | 4.79 | 0.06 | 23.60 | +0.39 | 4.79 | 3.42 | 5.97 | 243 | 1162, 1164, 1341, 2806 |
| CF | 2.55 | 1.55 | 1.37 | 3.22 | 7.93 | -0.61 | 25.31 | +2.04 | 5.46 | 2.96 | 7.49 | 250 | 245, 681, 1264, 1305 |
| CCl | 2.84 | 1.72 | 1.73 | 3.96 | 3.67 | -0.13 | 19.60 | -0.95 | 1.28 | 1.21 | 4.33 | 186 | 105, 398, 715, 1042 |

monolayers in Fig. 6.5 (b). Moreover, the calculated phonon dispersions having imaginary frequencies (near $M$ and $K$ high symmetry points of BZ) of Cl in-plane and out-of-plane modes practically isolated from graphene modes indicate that nonbonding chair structure is unstable. In fact, a minute displacement or perturbation of atoms in Cl plane results in the clustering of Cl atoms, if nonbonding chair structure is treated in a (4x4) supercell. It appears that structure optimization in earlier studies carried out in single cell resulted in an erroneous stability.

## 6.4 Stable Fully Chlorinationated Graphene: Chlorographene

### 6.4.1 Structural Properties

Our analysis indicates that like graphane and fluorographene, the chair structure chlorographene CCl, where one chlorine atom is attached to each carbon atom alternatingly from top and bottom sides is energetically most favorable and stable structure. The atomic structure together with structural parameters obtained after structure optimization are given in Fig. 6.6 (a). In the rest of thesis we name this stable structure as chlorographene or CCl. It has hexagonal lattice

with the space group $P-3m1$. The remarkable situation is that the planar and $sp^2$-bonded graphene is buckled by $\delta$=0.49 Å. This way the local configuration of three folded $sp^2$-bonding has changed to four folded $sp^3$-bonding, reminiscent of tetrahedrally coordinated diamond structures. Formation of four folded $sp^3$-bonding through buckling is essential for the stabilization of CCl, despite the C-C distance increased from 1.42 Å to 1.72 Å. While the C-Cl ionic bond in the adsorption of single Cl adatom is 2.54 Å, it transforms to a covalent bond by contracting to 1.73 Åin chlorographene. The latter bond can be contrasted with the Cl-graphene distance in nonbonding chair structure.

In Table 6.1 we compare the structural parameters, relevant energies like cohesive energy, formation energy and desorption energy of graphene, CH, CF and CCl, all calculated by using LDA. Cohesive energy ($E_{coh}$) is an indication of the stability of a material with respect to similar structures. It is seen that Chlorographene has CCl has lowest $E_{coh}$ per unit cell among other possible graphene derivatives. Whether the synthesis of chlorographene from graphene and $Cl_2$ molecule can be achieved spontaneously is deduced from the formation energy $E_f$. By definition the negative formation energy calculated for CCl indicates that the synthesis is endothermic and cannot take place spontaneously. However, once CCl is synthesized a desorption energy of 1.28 eV is required to take a single Cl atom out.

### 6.4.2 Vibrational Properties and Raman Spectra

Chair configuration of chlorographene (CCl) posses $D_{3d}$ point group symmetry. Phonon dispersion for CCl is shown in Fig. 6.6(b). It is seen that all the phonon modes have positive frequencies and hence the predicted structure of chlorographene is stable. Though the chlorographene belongs to the same space group with CH and CF,[65, 75] the phonon frequencies are lowered (softened) due to the saturation of C atoms with heavy Cl atoms. Both Cl and C atoms contributes almost equally to the acoustic modes. Unlike the phonons of nonbonding chair structure, Cl contributes to all phonon branches. Therefore, the phonon spectrum of chlorgraphene differs from the spectrum of graphene. While LA and TA

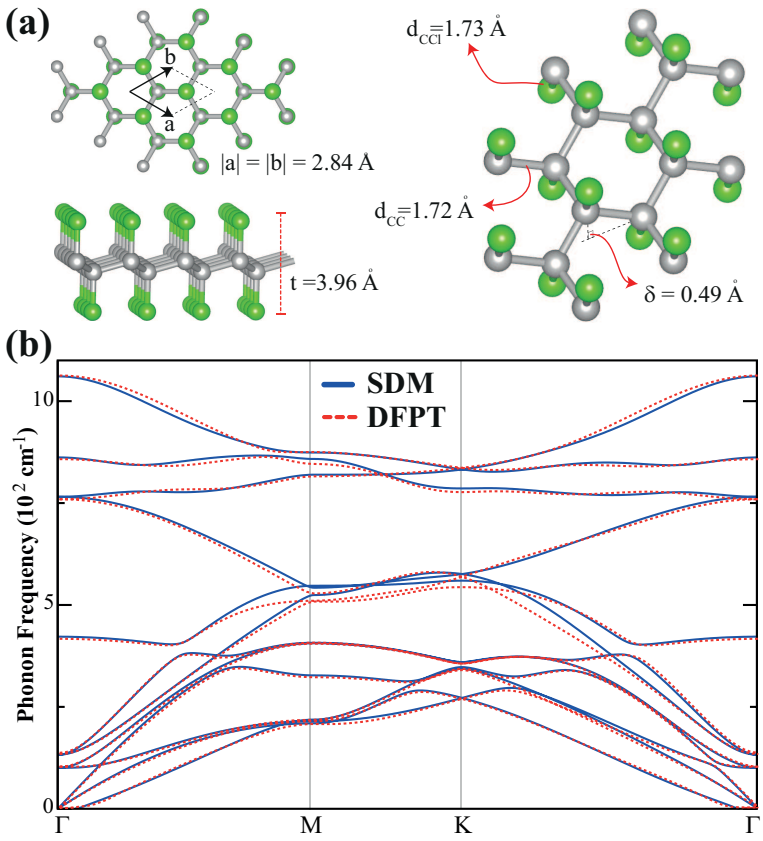


Figure 6.6: (Color online) (a) Top, side and tilted views for the atomic structure of chlorographene layer having hexagonal lattice and honeycomb structure. Carbon and chlorine atoms are indicated by gray (dark) and green (light) balls, respectively. Calculated structural parameters are indicated. (b) Phonon bands of chlorographene calculated using by SDM[4] and DFTPT[5] methods are presented.

modes have linearly dependent to phonon wave vector, ZA mode has a quadratic dispersion in the vicinity of Γ-point.[65, 75] As compared to single layer graphene, LO and TO (ZO) optical modes are softened from 1600 (900) to 1061 (421) $cm^{-1}$ due the existence of surrounding Cl layers. It appears both that SDM and DFPT agree and only slightly differ at M and K point for optical phonon branches near at 500 $cm^{-1}$.

Group theory analysis shows that the decomposition of the vibration representation at the Γ- point is $\Gamma = 2A_{1g}+2A_{2u}+4E_g+4E_u$. Among these, the modes at 105, 398, 715 and 1042 $cm^{-1}$ are bond stretching modes and are Raman-active. Raman mode $A_{1g}$ at 1042 (398) is entirely due to the out-of-plane vibration of C and Cl atoms moving in the same (opposite) direction with respect to each other. The observation of these Raman active modes are expected to shed light on the Cl coverage and the structure of chlorinated graphene. The observation of characteristic D-peak at 1330, G-peak at 1587 and 2D-peak at 2654 $cm^{-1}$ from chlorinated graphene indicates low coverage of Cl.[85] Since the Raman measurements were performed in the range of 1250-3500 $cm^{-1}$, possible Raman-active peaks originating from chlorine atoms may not have been observed.

Phonon frequencies, which are calculated to be positive at all **k**-points of BZ indicate that CCl is stable at T=0K. Our MD calculations at T=500 K indicate that CCl is also stable at room temperature. However, the structure dissociates into $Cl_2$ and graphene at 1000 K.

### 6.4.3 Electronic Properties

We present the band structure and orbital decomposed density of states of fully chlorinated graphene CCl in Fig. 6.7. As a consequence transition from $sp^2$- to of $sp^3$-type bonding and dramatic mixing with Cl orbitals through Cl-C covalent bonds, linearly crossing semimetallic bands of graphene changes dramatically and turn to a nonmagnetic semiconductor with a direct band gap of 1.21 eV (GGA+vdW value: 1.55 eV) at the center of BZ. The two-fold degenerate bands at the top of valence band are mainly composed of the $p_{xy}$ valence orbitals of

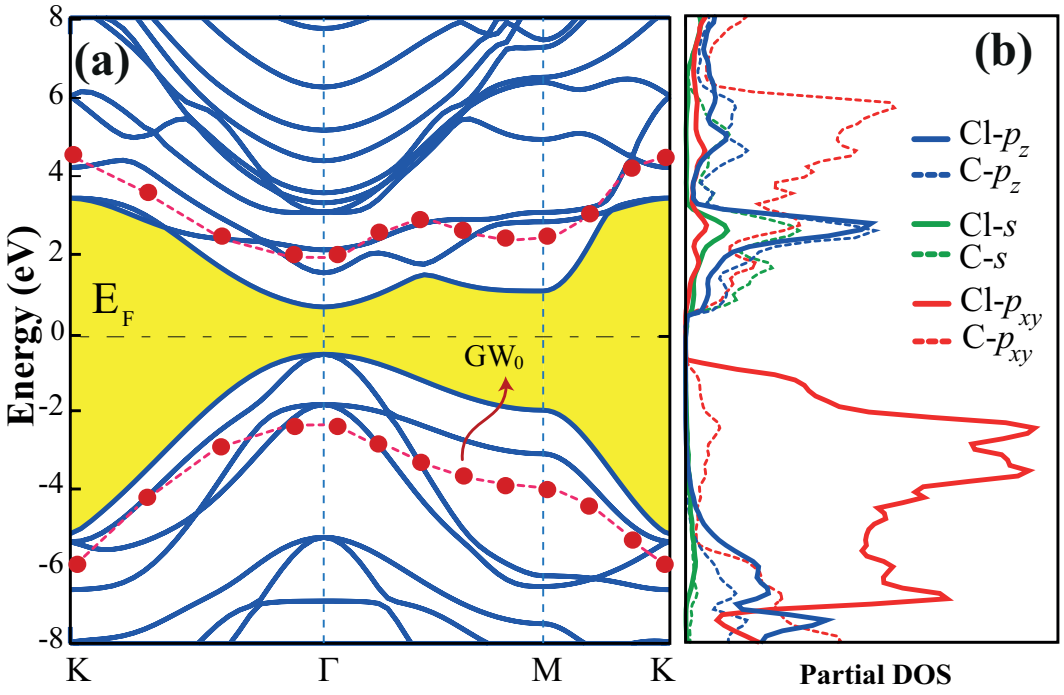


Figure 6.7: (Color online) (a) Electronic band structure of cholorographene CCl. The band gap is shaded yellow. The $GW_o$ corrected valance and conduction bands are shown by dashed line and red balls. The zero of energy set to the Fermi level $E_F$. (b) Density of states projected to various orbitals (PDOS).

Cl and C atoms and belong to the $E_g$ irreducible representation. However, non-degenerate conduction band edge is formed by the hybridization of C-$p_{xy}$, C-$p_z$, C-$s$ and Cl-$p_z$ and belongs to the $A_{2u}$ irreducible representation. Calculated values relevant for the electronic properties of CCl are given together with those of graphene, CH and CF in Table 6.1. CCl has the lowest band gap (1.21 eV) among graphene derivatives, i.e. graphane (3.42 eV) and fluorographane (2.96 eV). Our calculations also reveals that the experimentally observed energy gap of 0.045 eV may arise from the partially chlorinated regions. While graphane have a positively charged surface due to the electron transferred from H to C atoms, Cl layers of CCl are negatively charged since 0.13 electrons (GGA+vdW value: 0.10 electrons) are transferred from C to Cl atoms. We note that the effective charge is reduced from 0.42 to 013 electrons by going from ionic C-Cl bond in single Cl adsorption to the covalent C-Cl bond of chlorographene. This corroborates our arguments related with the change of character of bonding in CCl.

Since DFT usually underestimates the band gaps, the band gap of 3D bulk crystals are successfully corrected by $GW_o$ self-energy method. In the present thesis we apply $GW_o$ method to correct valance and conduction bands and hence the band gap of CCl. We found the corrected band gap 4.33 eV. This is a dramatic increase. Similar situation occurred for the correction of band gaps carried out for single layer structures, such as BN[91], CF[65] and $MoS_2$[92]. In particular, while LDA predicted band gap of single layer $MoS_2$ agrees with experiment, $GW_o$ correction yielded very large band gap. This situation led us to question whether $GW_o$ correction is suitable for single layer structures. Nevertheless, we hope that the paradoxical situation and hence the suitability of $GW_o$ correction will be resolved with new experimental data on the band gap. It is also found that it is possible to lower the photoelectric threshold of graphene from 4.49 eV to 3.67 eV by covering its surfaces with chlorine atoms. In contrast, as one notices in Table 6.1, both fluorinated[65] and hydrogenated[36, 75] derivatives of graphene have photoelectric thresholds higher than graphene and CCl. The lower photoelectric threshold provide materials highly emissive surfaces and this facile photoemission feature is desirable for fast laser applications.[93, 94]

### 6.4.4 Mechanical Properties

Earlier studies have shown that graphane[68, 53] and fluorographene[65, 75] derivatives are strong materials comparable with graphene. Among the three graphene derivatives chlorographene is the thickest one and we can expect some different mechanical properties. We will discuss the structural rigidity of chlorographene within the harmonic range of the elastic deformation, where the structure responded to strain $\epsilon$ linearly and reversibly. Under elastic range, in-plane stiffness $C$ would be a good measure of the response of material. Here we use the expression to calculate in-plane stiffness, $C = (1/A_0) \cdot (d^2E_S/d\epsilon^2)$, where $A_0$ is the equilibrium area of the supercell and the strain energy is defined as the total energy at a given uniform strain minus the total energy at zero strain, namely $E_s = E_T(\epsilon) - E_T(\epsilon = 0)$. Here the strain in one direction is $\epsilon = \Delta c/c_o$, where $c_0$ is the equilibrium lattice constant of supercell and $\Delta c$ is its stretching. For CCl we calculated $C$ as 186 $J/m^2$ which identifies it as strong as CH and CF.

In Fig. 6.8(a) we show the variation of the strain energy $E_s$ and the derivative of strain energy $dE_s/d\epsilon$ with the applied uniform strain. It is linear for small $\epsilon$ in the harmonic range. The elastic deformation occurs until the maximum, whereby the structure attains its initial state when the applied strain is lifted. Beyond the maximum the structural instabilities sets in with irreversible deformations. The region beyond the maximum is called plastic region. This region It seen that CCl undergoes instability, under 0.15 expansion of the lattice. Whereas, the critical expansion values are 0.20 and 0.24 for CF and CH, respectively.

We also calculated the effect of elastic strain on the band gap of CCl, CF and CH. It is obvious that the CH and CCl have similar response to elastic strain. Their band gap increase first, then decreases. In contrast, initially the band gap of CF does not show any significant increase with increasing strain; for small strain it is almost unaltered, but decreases rapidly for large strain. Because of its smaller band gap, the metallization of CCl occurs earlier in the course of expansion.

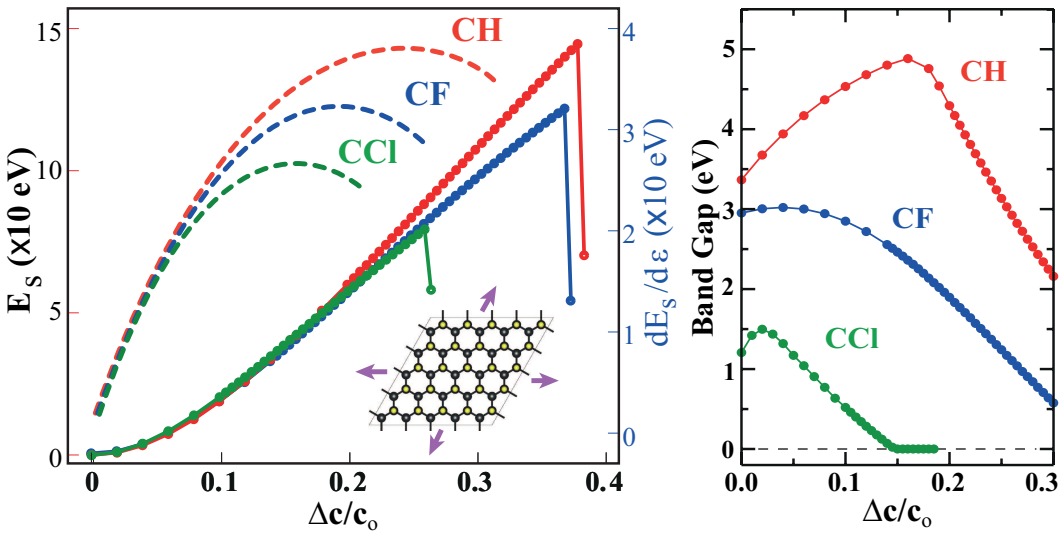


Figure 6.8: (Color online) (a) The variation of the strain energy and its derivative of with applied uniform strain $\epsilon$ calculated for CCl, CH and CF. The structure of $dE_s/d\epsilon$ is enhanced due to the scale of the plot. After the maxima indicated by arrows structures become unstable and undergoes a plastic deformation. Calculations performed in (5x5) supercells. The strain in one direction is $\epsilon = \Delta c/c_o$. $c_0$ is the equilibrium lattice constant of supercell and $\Delta c$ is its stretching. (b) Variation of the band gap with uniform strain.

### 6.4.5 Defects

Depending on the synthesis techniques and laboratory conditions diverse defects and vacancies can be formed on the crystal structure. In our previous works on CF and CH, we have found that the various types of vacancies can also be utilized to modify the electronic and magnetic properties of graphene derivatives.[65, 36, 95] In particular, one can attain magnetic moments by creating vacancies of X in CX conformers. In the case of CCl, the desorption of a single Cl atom requires 1.28 eV energy and hence the vacancy of Cl creation is easier with respect to CH and CF. In this thesis we investigated various vacancies in CCl as illustrated in Fig. 6.9

In the top panels of Fig. 6.9 we show $Cl_N$) vacancies for $N$=1-4. The ground state of a single Cl vacancy of CCl, Cl(1) is found to be nonmagnetic. The magnetic state with $\mu$=1.0 $\mu_B$ magnetic moment occurs only 40 meV above the ground state. In contrast, the single vacancies of CF and CH are known to be magnetic and have magnetic moment $\mu$=1.00 $\mu_B$. However, for the $Cl_2$ vacancy, Cl-free carbon atoms are dimerized and make $sp^2$-type bonding and therefore the ground state is nonmagnetic as in CF and CH. Similar to single Cl vacancy case, $Cl_3$ vacancy has a nonmagnetic ground state. Finally we calculated 0.44 $\mu_B$ for $Cl_4$ vacancy. In the present case, the deviations from the Lieb's theorem occurs due to strong coupling between Cl adatoms.

In the middle panels of Fig. 6.9 $(CCl)_N$ vacancies or holes with $N$=1-4 are shown. These type of vacancies may be obtained in single layer structures at the grain boundaries by irradiation with heavy atoms. The optimized structure of $(CCl)_1$ vacancy has a magnetic ground state of $\mu$= 1.0 $\mu_B$. This situation is in compliance with the Lieb's theorem[52] due to unpaired electron of missing C atom. However the fragmentation for $(CCl)_2$, $(CCl)_3$ and $(CCl)_4$ vacancies in even 6x6 supercells, also calculated. Such an easy fragmentation process may permit the synthesis of narrow nanoribbons with suitably tailored edges.

While the energy optimization based on conjugate gradient indicates that the above types of vacancies and holes are stable, the ab-initio MD calculations result

in dissociation of $Cl_2$ from the holes or the domains of CCl. Moreover, if a single Cl vacancy is found at one side of CCl, another Cl vacancy can also formed at the other side. Interestingly, a pair of Cl vacancies at different sites and above adjacent carbon atoms appear to be stable at 500K.

In summary, this chapter, interaction of chlorine atoms with graphene and the possible chllorinated graphene derivatives are investigated. It is found that while the binding of single chlorine atom to graphene is significant, its migration on the surface of perfect graphene takes place almost without barrier. However, it is easy for two Cl atoms at close proximity to form $Cl_2$ molecule and to desorb form the surface. The energy optimization and phonon calculations indicate that the chair configuration of fully chlorinated graphene (chloragraphene) is energetically favorable and stable structure. Electronic properties of the chlorographene a semiconductor with 1.2 eV bandgap can be tuned rapidly via applied strain. However, the vacancy defects in fully chlorinated graphene give rise to structural instabilities.

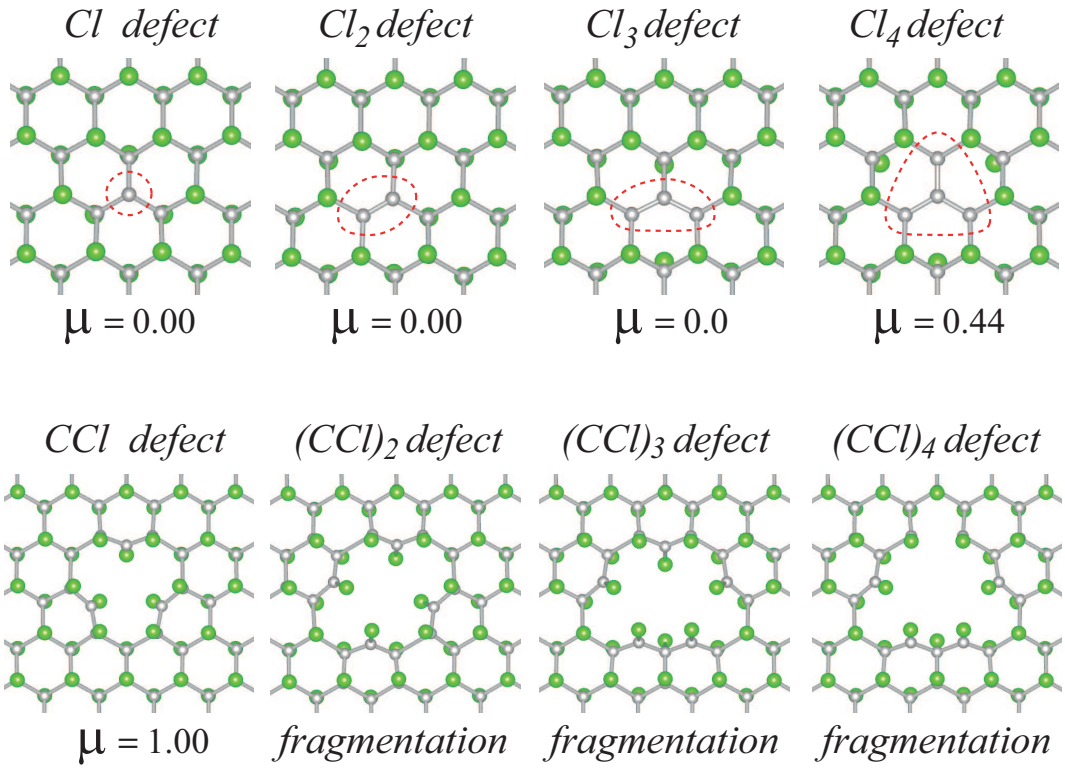


Figure 6.9: (Color online) Top Panels: Atomic structure of various types of defects, $Cl_N$ $N$=1-4 and their calculated magnetic moments. Middle Panels: $(CCl)_N$ defects with $N$=1-4 and their calculated magnetic moments. (c) Bottom Panels: Fragmentation of the structure CCl having a single $(CCl)_N$ hole in the supercell.

# Chapter 7

# Graphene Nanocoatings

In this chapter, it is demonstrated that graphene coating can provide an efficient protection from oxidation by posing a high energy barrier to the path of oxygen atom, which could have penetrated from the top of graphene to the reactive surface underneath. Graphene bilayer, which blocks the diffusion of oxygen with a relatively higher energy barrier provides even better protection from oxidation. While an oxygen molecule is weakly bound to bare graphene surface and hence becomes rather inactive, it can easily dissociates into two oxygen atoms adsorbed to low coordinated carbon atoms at the edges of a vacancy. For these oxygen atoms the oxidation barrier is reduced and hence the protection from oxidation provided by graphene coatings is weakened. Our predictions obtained from the state of the art first-principles calculations of electronic structure, phonon density of states and reaction path will unravel how a graphene can be used as a corrosion resistant coating and guide further studies aiming at developing more efficient nanocoatings.

## 7.1 Motivation

The reaction of material surfaces with oxygen and controlling damages from corrosion have been the subject of intensive research for decades. While protective macroscale coatings give rise to the modification of the sizes and some other physical properties of reactive surfaces, progress made to date has revealed several advantages of nanoscale coatings in protection from corrosion and wear. Graphene,[6] being not only the thinnest ever but also the strongest material, has the potential for nano-coating applications.[96] When sticks to or grown on various surfaces, graphene adds only negligible thickness to the size of the underlying sample and forms an electrically and thermally conductive coating on it.[96] Moreover, graphene has exceptional mechanical, thermal and chemical stability. Experimentally, the graphene coatings on Cu, Cu/Ni alloy, Pt and Ir surfaces have been exploited.[96, 97] XPS and SEM images presented evidences that Cu and Cu/Ni surfaces can be protected from oxidation through graphene coating.[96] However, despite these recent progresses, very little is known how and why graphene layer constitutes a protective coating on reactive surfaces and what are its limitations.

In this study we show that graphene can easily be oxidized by oxygen atoms which form strong chemical bonds on its surface. Despite that the graphene coating can protect solid surfaces from oxidation by posing a high energy barrier to any adsorbed oxygen atom diffusing from the top of graphene to the interface between graphene and the reactive surface underneath. Because of this barrier perpendicular diffusivity of oxygen atom is practically zero as compared to its lateral diffusivity. Although an oxygen molecule is weakly bound to graphene and does not have any direct role in the oxidation, it can be indirectly involved by dissociating into two atomic oxygens. These oxygen atoms form relatively stronger chemical bonds with twofold coordinated carbons but encounter much lower oxidation barrier when diffuse towards the reactive surface. Poor protection from oxidation at defect sites can be circumvented by multilayer graphene coating. In contrast, BN, an ionic single layer honeycomb structure does provide protection not as good as graphene.

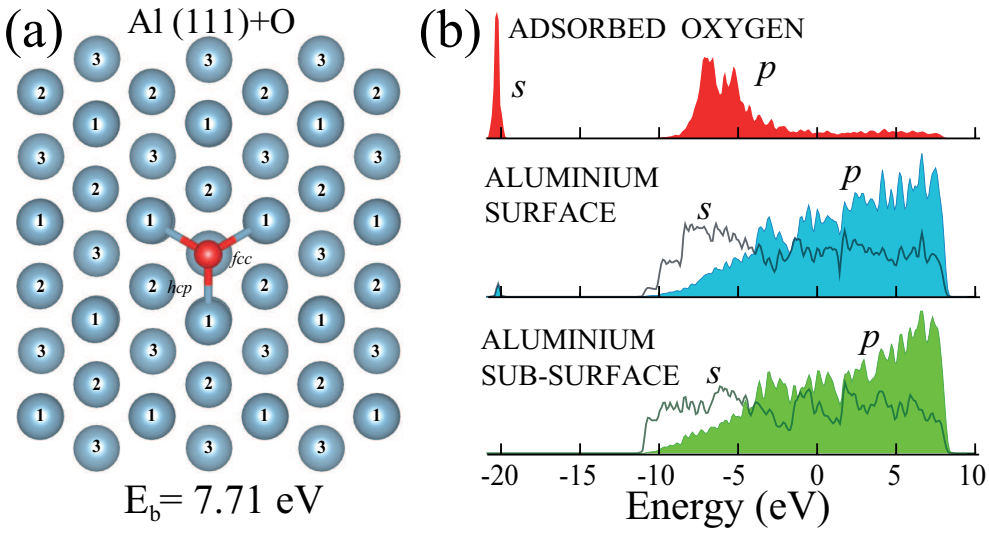


Figure 7.1: Oxidation of the Al(111) surface: (a) Atomic configuration of an oxygen atom adsorbed to Al(111) surface, which is represented by a 4-layer slab. Oxygen and Al atoms are illustrated by small-red and large-blue balls with numerals indicating their layer numbers from the top. Al atoms at the fourth layer are hidden below the first layer atoms. (b) Density of states (DOS) projected to $s$- and $p$-orbitals of adsorbed O, surface and subsurface layers of Al(111) slab. Zero of energy is set to Fermi energy.

Our study proceeds in three complimentary and sequential steps: In the first step we examine the interaction of $O_2$ and O atoms with a bare reactive metal surface and with a bare pristine graphene, where importnt features are discovered. Second step deals with the sticking of graphene to a flat, unoxidized surface, which is vulnerable to oxidation. In the third step, we show how graphene coating hinders oxygen atoms from diffusion towards the protected surface. Our results are obtained by performing first-principles, spin-polarized calculations[43, 44] within Density Functional Theory. We used Generalized Gradient Approximation[88] including Van der Waals (vdW) correction[89] and PAW potentials.[46] To minimize the coupling between adsorbed atoms or molecules, the binding energies and reaction paths are calculated using large (4x4) or (6x6) supercells. For the coated surfaces a grid of 25x25x1 **k**-points is used. The convergence criterion of self consistent calculations for ionic relaxations is taken $10^{-5}$ eV between two consecutive steps. By using the conjugate gradient method, atomic positions and lattice constants are optimized until the atomic forces are less than 0.05 eV/Å. The energetics of various paths of O or $O_2$ are calculated by forcing them to displace from above to below. The amount of displacement is specified as *indentation* in the figures. In some cases, the reaction paths of O are fixed, but the rest of atoms are relaxed to estimate the associated energy barriers. The path of minimum energy barrier is determined by relaxing carbon atoms, as well as lateral $x$- and $y$-coordinates of O or $O_2$ at each step of indentation.

## 7.2 Oxidation of Al Surface and Graphene

Since we are not concerned with sample specific details of oxidation behaviors of the protected surfaces, Al(111) surface is taken here only as a prototype metal surface vulnerable to oxidation when exposed to atmosphere, but is protected by placing a graphene sheet between its surface and atmosphere. Al(111) surface alone is represented by a 4-layer Al(111) slab as described in Fig. 7.1. It has metallic and nonmagnetic ground state, and its states at the Fermi level are composed of mainly $3p_{xy}$- and partially $3s$-orbitals of Al atoms. The work function for this slab is calculated to be 4.06 eV, which is comparable to the experimental

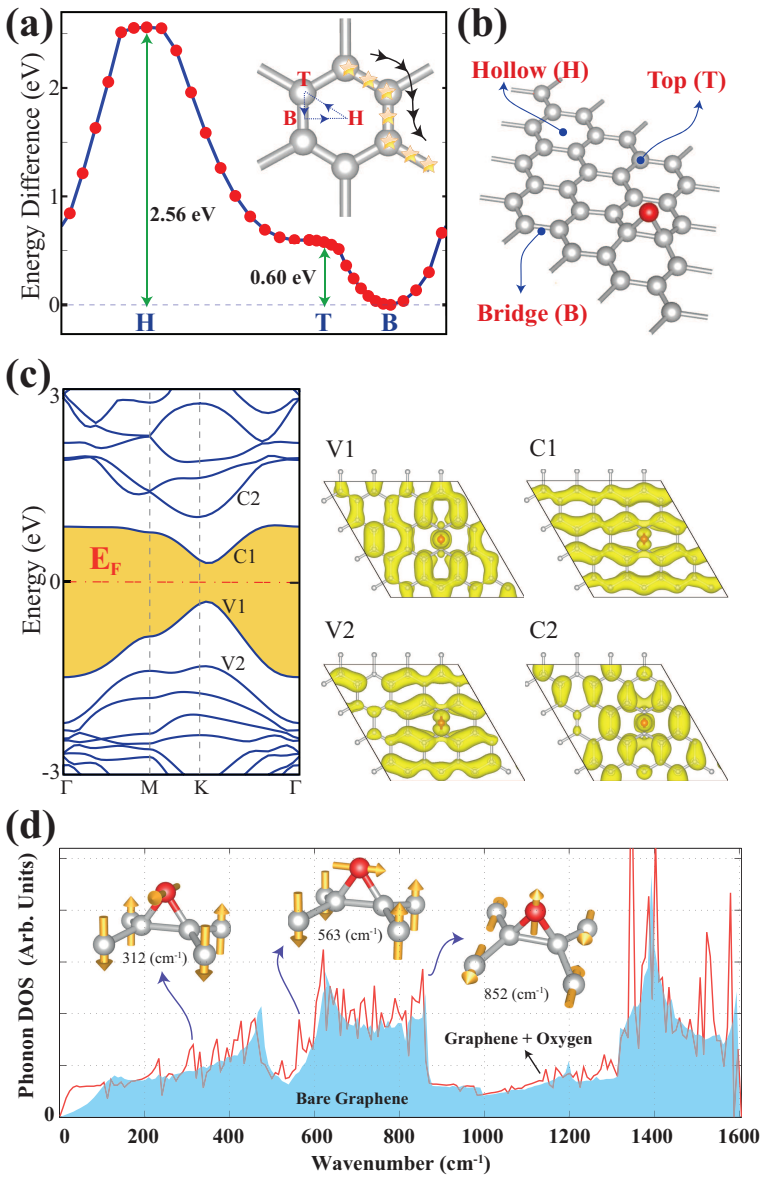


Figure 7.2: Oxidation of bare graphene: (a) Variation of the energy of adsorbed oxygen atom along T(top)-H(hollow)-B(bridge) site directions of a hexagon showing that B-site is energetically most favorable. Stars indicate favorable path for the diffusion of oxygen atom on the graphene surface. (b) Oxygen atom adsorbed at the bridge site of a (4x4) supercell of graphene consisting of 32 carbon atoms. (c) Electronic energy band structure corresponding to (b) together with the charge densities of specific conduction and valence band states. Upon oxidation the linearly crossing $\pi$ and $\pi^*$ states of semimetallic bare graphene are modified and opened a band gap of 0.58 eV. (d) Density of phonon modes of a pristine graphene (shaded area) and those of oxygen adsorbed to the bridge site of the (4x4) supercell of graphene (red line) are calculated from the first principles.[98] Relevant localized phonon modes are indicated by insets.

value of 4.24 eV measured experimentally[99] for Al(111) surface. We calculate that an oxygen atom strongly bound to the Al(111) surface with 7.71 eV binding energy at the fcc site and 7.24 eV for hcp site. Fig. 7.1 (b) presents the densities of electronic states projected to adsorbate O, surface and subsurface layers of Al(111) slab. Apparently, $2p$-orbitals of adsorbed O mix with the $3p$ and $3s$-orbitals of Al substrate in a wide energy range to form a strong bond. Oxygen molecule by itself interact strongly with Al(111) surface; it dissociates into atomic oxygens, which in turn are adsorbed at fcc and hcp sites.

Bare graphene can also be easily oxidized, whereby oxygen atoms are adsorbed at the bridge site positions above any C-C bond of graphene and become negatively charged. The binding energy is calculated to be 2.56 eV at the bridge site, hence O atoms at the top- or hollow- (i.e. center of hexagon) site in Fig. 7.2 move favorably to the bridge site. In Fig. 7.2 (c) single O adatom adsorbed to a (4x4) graphene supercell opens a gap of 0.58 eV. This explains why domains of dark (metallic) graphene surface becomes reflecting (insulator) upon oxidation.[100] Adsorbed oxygen atom give rise to several localized phonon modes shown in Fig. 7.2 (d), which will be used in estimating the characterized frequency and the diffusivity thereof. Reversible oxidation-deoxidation of graphene through heating or charging has been pointed out as potential electronic device application.[100, 101] Reversibility is a strong evidence that graphene surface remain chemically stable in the course of oxidation-deoxidation; neither bond breaking nor modification of honeycomb structure does occur. However, the situation is dramatically different for several other surfaces, such as Si, Fe, Te, Al, Cu etc, where the chemical stability is destroyed upon oxidation.[102, 103, 104, 96]

In contrast to oxygen atom, an oxygen molecule has a weak binding with graphene. We calculated its binding energy to be 115 meV, and magnetic moment 1.90 $\mu_B$, slightly smaller than the magnetic moment of free $O_2$. Hence, an $O_2$ molecule with such a weak binding energy to bare graphene cannot have any significant effect on the oxidation of the protected surface, though the situation can be different for the defected graphene as we will show later. On the other hand, a free O atom approaching another O atom already adsorbed on graphene forms a strong bond with the latter releasing $\sim$ 4.13 eV energy, and eventually

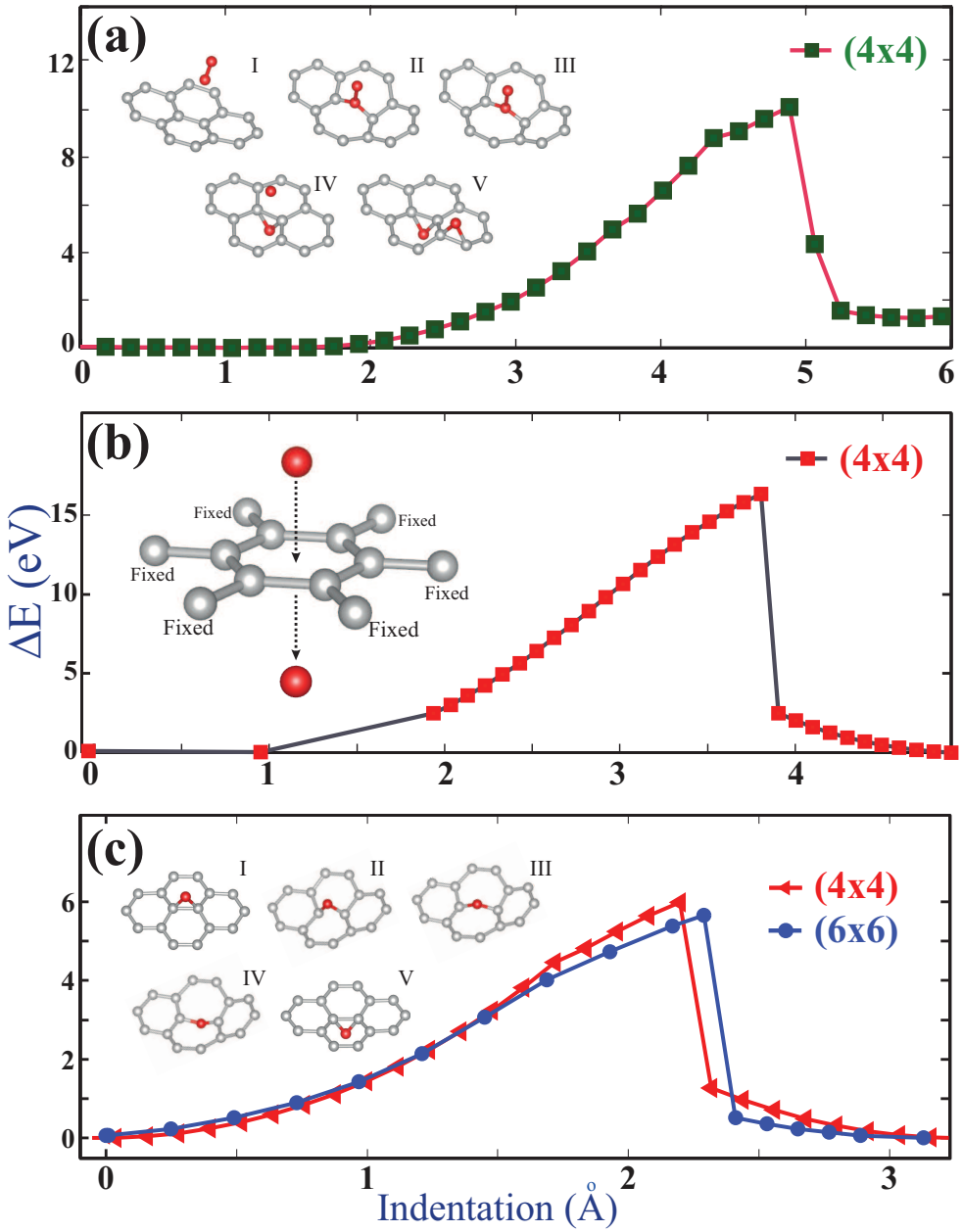


Figure 7.3: Calculation of energy barriers in various paths of $O_2$ and O moving from the top to bottom side of a suspended graphene, which may be relevant for the oxidation: (a) $O_2$, which moves perpendicular to graphene surface and is forced to pass from the top to bottom side of graphene along a vertical line through the hole at the center of a hexagon. (b) The energy barrier for a single oxygen atom forced to pass from the top to bottom side of graphene along a vertical line through the hole at the center of a hexagon. (c) An oxygen atom adsorbed at the bridge site above the graphene plane is forced to pass to the bottom side. Positions of carbon atoms as well as the lateral $x$- and $y$-coordinates of oxygen are optimized for each value of indentation. The path followed in (c) appears to have lowest energy barrier.

an $O_2$ molecule is formed thereof. This may explain why deoxidation of graphene occurs so easily[100] at the STM tip at 100° C, despite the strong binding energy of O atom. Note that two adsorbed O at close proximity can also form an $O_2$ molecule by releasing an energy of 1.6 eV, if they can overcome an energy barrier.

## 7.3 Protection of Al Surface by Graphene Coating

Next we explore the protection of a reactive surface, such as Al(111) by sticking or growing graphene on it. Sticking of graphene on various metals surfaces including Al(111) surface has been studied earlier.[105] Even though Al(111) surface are not in registry with graphene honeycomb structure and has hexagonal lattice constants $\sim$ 10% larger than those of graphene, sticking of graphene on this surface can be achieved. In order to present an estimation value for the sticking energy of graphene to Al(111) surface one has to compress Al(111) slab laterally and expand graphene lattice in order to achieve the registry for the optimization of final structures using periodic boundary condition. Despite the strain energy spent to obtain the lattice registry, the sticking occurs with a significant binding energy of 2.67 eV per (4x4) supercell or ($\sim$166 meV per cell). The sticking of graphene patches to the Al(111) surface in random orientation is a complex and stochastic process, and can even lead to the formation of bubbles, since low coordinated edge atoms have stronger binding with Al(111) surface. Even if the average binding energy per carbon atom is small, it would require significant energy to peal off the strong but flexible graphene layer from the surface.

If graphene patches are placed randomly on Al(111), they may not be severely strained to maintain the lattice registry. Therefore, we rather consider unstrained graphene and compensate the lattice misfit by laterally compressing Al(111) slab. This way we achieve the lattice registry and use the periodic boundary conditions. Under these circumstances, the sticking energy of graphene to this compressed Al(111) slab, which is calculated to be 2.38 eV per (4x4) super cell (or $\sim$ 148 meV per cell) is not significantly affected. Additionally, the binding energy of O atom to the compressed Al(111) surface (7.15 eV) is still very high. Thus, despite

the compression dictated by the periodic boundary conditions, the compressed Al(111) slab is still sufficiently reactive to mimic a surface to be protected by graphene coating.

Now we address the main issue pertaining to how a graphene coating, which by itself is also vulnerable to oxidation can protect a reactive metal surface. To clarify the mechanism of protection from oxidation we first examine how an $O_2$ molecule or O atom can pass from one side of bare and suspended graphene to the other side. The energetics and energy barriers involved in the course of these processes are calculated in a (4x4) supercell of bare graphene with specific carbon atoms are fixed to prevent the suspended layer from displacement. Energy variations on different reaction paths are summarized in Fig. 7.3. An oxygen molecule following the minimum energy path needs to overcome a barrier of 10.12 eV in Fig. 7.3 (a). However, once $O_2$ overcome this barrier, it dissociates into two O atoms; one O adsorbed above, the other adsorbed below at the bridge sites. Apparently, graphene acts as a membrane, that blocks the passage of $O_2$. If an O atom were forced to move along a fixed vertical path passing through the hole at the center of hexagon (i.e. a seemingly possible diffusion path) the energy barrier would be even higher, i.e. 16.34 eV in Fig. 7.3 (b). The path shown in Fig. 7.3 (c) starts from the adsorbed oxygen atom at the top bridge side, i.e. the minimum energy configuration of O atom adsorbed on pristine graphene. At each stage of indentation, carbon atoms, as well as $x$- and $y$-lateral coordinates of O atom are optimized to minimize the energy. As seen from the snapshots of atomic configuration corresponding to various stages, the passage of O take place around the same bridge bond, whereby O atom switches from top to bottom side of graphene by gradually flattening C-O-C bridge bond. The energy barrier, which is overcame by an O atom to pass from the top side to the bottom is calculated to be $Q$ =5.98 eV. To reveal whether the (4x4) supercell may impose constraints on the calculated energy barrier, we calculated the barrier in a relatively larger, (6x6) graphene supercell to be 5.65 eV. The calculated energy barrier is not affected from the size of the supercell and is high enough to block diffusion and hence to hinder oxidation of the surface underneath. This path is identified as the path of minimum energy barrier for O atom passing from the

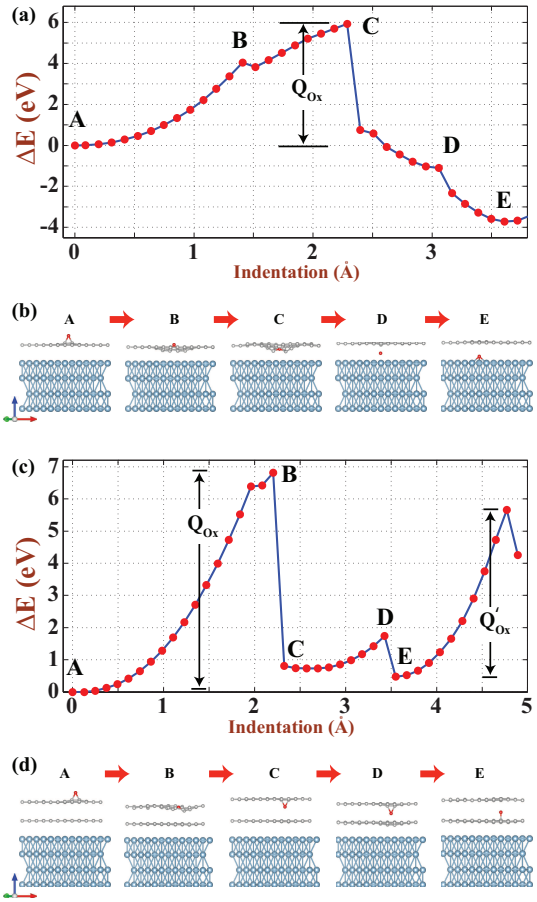


Figure 7.4: (a) Variation of energy of an oxygen atom passing (indenting) from the top side of single graphene layer to its bottom side and eventually adsorbing to Al(111) surface underneath. Oxygen atom is initially adsorbed at the bridge site above graphene surface and follows the path of minimum energy barrier $Q_{ox}$. Various stages from A (which corresponds to an oxygen atom adsorbed to graphene at the bridge site above) through C (i.e. the point of maximum energy where O passes from above to bottom part of graphene) and E (eventually oxygen adsorbed to Al(111) surface) show that the surface of the metal is oxidized if an energy barrier of $Q_{ox}$ =5.93 eV is overcame. (b) Protection of Al(111) surface from oxidation by a graphene bilayer and the variation of energy of oxygen adsorbed at the bridge site of first graphene layer corresponding to the stage A. Diffusing O has to overcome $Q_{ox}$ =6.81 eV at B. At C oxygen atom is switched to the bridge site at the bottom side of first graphene. At E the diffusing O switches to second graphene layer and is adsorbed its bridge site. A second energy barrier of $Q^{'}_{ox}$ = 5.20 eV is needed to be overcome for O atom to oxidize the metal surface.

top to bottom of bare suspended graphene.

In the presence of the Al(111) slab underneath the protective graphene coating, we elaborate and further optimize the reaction path in Fig. 7.3 (c) as the most likely pathway of oxidation. The variation of the energy of an O atom moving along the reaction path is shown in Fig. 7.4 (a). The energy barrier along this reaction path is $Q_{ox} \sim 5.93$ eV and occurs as O is switching from top side to bottom side of graphene. Once the diffusing O atom overcomes this barrier, it goes to Al(111) surface via the bridge site below without almost any barrier and oxidizes the metal surface. This energy barrier $Q_{ox}$, to be overcame by the diffusing O atom is rather high and hence the protection of graphene against oxidation appears to be very robust. The significance of high $Q_{ox}$ can be deduced by comparing the diffusivity of O moving on graphene surface $D_{\parallel}$ with that of O atom penetrating the graphene coating to oxidize the Al(111) surface, $D_{\perp}$. $D_{\parallel} = a^2 \nu e^{Q/k_B T}$ can be estimated in terms of the energy barrier $Q$ =0.60 eV in Fig. 7.2, lattice constant $a$=1.43 Åand the characteristic vibration frequency extracted from the calculated localized phonon modes of O in 7.2 to be $\nu = \sim 22$ terahertz. Accordingly, the diffusivity of O penetrating the graphene coating is estimated to be $D_{\perp} = D_{\parallel} \times 10^{-87}$, which is really negligible.

### 7.3.1 Bilayer Graphene Coating

The effectiveness of the protection can be further increased by coating with graphene bilayer. In Fig. 7.4 (b) the variation of energy of diffusing O atom from outermost graphene layer to the metal surface via second graphene layer following the minimum energy reaction path is shown. Apparently, the oxidation barrier is raised by 0.88 eV due to to the coating by graphene bilayer. Relevant stages in the course of diffusion of O starting above the first graphene layer through the second graphene layer and eventually ending at the surface of Al(111) surface are also indicated in Fig. 7.4 (b). While the oxidation barrier $Q_{ox}$ =6.81 eV occurs when the diffusing O switches from the top to the bottom side of first graphene layer, there are additional barriers blocking the diffusion of O atoms. For example, the energy barriers for switching from the bottom bridge site of

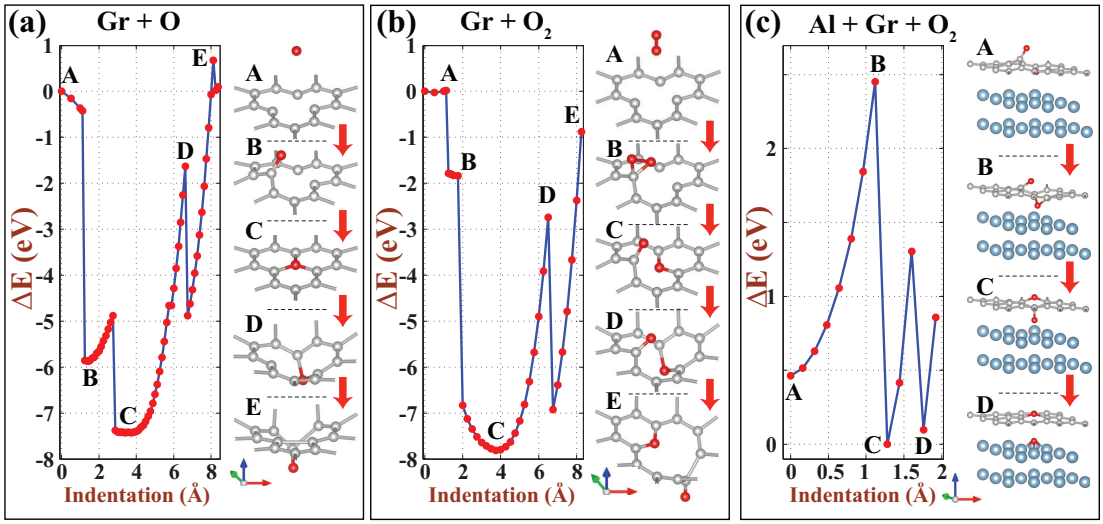


Figure 7.5: (a) Evolutions of energetics and atomic structure with the indentation of the oxygen atom, which is initially adsorbed at the edge of a single vacancy. (b) Evolutions of energetics and atomic structure of two oxygen atoms resulting from the dissociation of $O_2$ molecule at the edge of a single vacancy and the indentation of one of oxygen atoms from the top to bottom site of a suspended graphene. (c) The diffusion of one of adsorbed oxygen atoms in (b) towards the Al(111) surface resulting in its oxidation. Red, gray and blue balls indicate, respectively O, C and Al atoms.

first layer graphene to the top bridge site of second graphene layer is $\sim$ 1 eV. If this small barrier is overcame, the adsorbed O atom becomes attached to the second graphene layer and is still separated from reactive surface. To proceed with diffusion to reach at the Al(111) surface one follows similar course as in Fig. 7.4 (a).

Clearly, the coating of reactive surfaces by sheets comprising more than two layers of graphene will further increase the effectiveness of protection. Sequential barriers posed at each graphene layer increase the chance that the diffusing O can be trapped between any two barriers. On the other hand, the size of the protected sample will be modified by each additional graphene layer adding $\sim 3$ distance between O and Al surface, even if this may be considered negligible. Protection by graphene sheets comprising a few layers are expected to be effective also to suppress the effects of any local heating or energy transfer to the outermost graphene. For example, as pointed out at the beginning a free oxygen at the close proximity of an adsorbed oxygen on graphene can form $O_2$, whereby an energy of $\sim 4.13$ eV is released. When deposited to the graphene, this energy may create a local, nonequilibrium phonon distribution, which was shown to dissipate within pico seconds.[106, 38] Such a short time interval is enough to accommodate several jumps of atoms. Hence a local heating due to a chemical process may promote the diffusion of other adsorbed oxygen atoms from the protective coating towards the reactive surface. Under these circumstances while single layer graphene coating fails to hinder oxidation, multilayer graphene coating can block the diffusing hot oxygen atoms.

### 7.3.2 Vacancy Effect

The above arguments related with the protection against oxidation relies on the fact that graphene coating is continuous and defect free. If coating consists of graphene patches, reactive surfaces cannot be covered at the zones between patches, where they become directly exposed to atomic oxygens.[96] The holes or vacancies[107, 108] of graphene are also spots, where oxygen atoms would penetrate the metal surface without or relatively smaller energy barrier. In fact, the

etching of graphite following the dissociation of $O_2$ by producing CO and $CO_2$ have been pointed out.[26, 109] Here we consider the penetration of oxygen atom near a vacancy in graphene. Three important features of our work are schematically summarized in Fig. 7.5. An oxygen atom can favorably bound to carbon atoms at the edge of single vacancy in Fig. 7.5 (a). The ground state is exothermic and releases 7.65 eV, whereby O atom substitute the vacant carbon atom. In Fig. 7.5 (b) an $O_2$ molecule can dissociate in two O atoms at the close proximity of a vacancy in graphene. Subsequently, while one O atom is attached to one of three twofold coordinated carbon atoms at the edge of the vacancy, the other one bridges between the remaining two and hence completes the hexagon. In this exothermic process 7.83 eV energy is released in addition to the energy spent in dissociation process. This shows that vacancies of graphene are active sites to catalyze the dissociation of $O_2$ molecules. Fig. 7.5 (c) shows that the barrier in the diffusion of a specific O atom adsorbed at the edge of a vacancy is dramatically lowered ($Q_{ox} \sim 2$ eV) and hence the protection from oxidation is weakened. Such a situation shall occur at the grain boundaries and holes of graphene and confirms the experiment[96] that defects or discontinuities in covering a reactive surface by graphene may result in the weakening of the oxidation protection. Similar processes have been also confirmed at the edges of relatively larger holes. This serious limitation caused by defects can be avoided by multilayer coatings.

Finally, BN single layer, another ionic honeycomb structure almost lattice matched to graphene can be used also as a protective coating against oxidation, but owing to relatively smaller barrier of $Q_{ox}$ =4.80 eV it can provide protection not as good as graphene.

In conclusion, we demonstrated that continuous coating of pristine graphene on reactive surfaces can provide for an excellent protection from oxidation of reactive surfaces at nanoscale. The binding of oxygen atom at low coordinated carbon atoms is rather high, but their barrier to penetrate to the reactive surface under graphene is low. Therefore discontinuities in graphene coating or defects, such as vacancies or holes weaken the protection from oxidation by creating spots on the coating with low oxidation barrier. This limitation can be circumvented by coating of bilayer or preferably graphene sheets comprising a few graphene

layers, which provides even more effective protection. At macroscale, our results suggests that graphene additives can improve the strength of antioxidant paints. Graphene coating, which is thin at the atomic scale can also serve as a natural barrier between environment and solid surfaces for other atoms.

# Chapter 8

# Graphene Nanomeshes

In this chapter the structural, mechanical and electronic properties of defect-patterned graphene nanomeshes including diverse morphologies of adatoms and holes are investigated by means of first-principles calculations within density functional theory. It is found that various patterns of adatom groups yield metallic or semimetallic, even semiconducting behavior and specific patterns can be in a magnetic state. Even though the patterns of single adatoms dramatically alter the electronic structure of graphene, adatom groups of specific symmetry can maintain the Dirac fermion behavior. Nanoholes forming nanomesh are also investigated. Depending on the interplay between the repeat periodicity and the geometry of the hole, the nanomesh can be in different states ranging from metallic to semiconducting including semimetallic state with the bands crossing linearly at the Fermi level. We showed that forming periodically repeating superstructures in graphene matrix can develop a promising technique to engineer nanomaterials with desired electronic and magnetic properties. The results pertaining to this chapter are published in Ref.[[95]] and figures are reproduced with permission of the publisher.

## 8.1 Motivation

Propagation of electron waves through the honeycomb lattice attributes exceptional features to graphene.[11] Conduction of electrons within one-atom-thick layer with minute scattering makes the observation of quantum effects possible even at room temperature.[10] Experimental investigations have reported the observation of half-integer quantum Hall effect for carriers in graphene and possible magneto-electronic device applications.[9] Most of the unique properties of graphene are related to its monolayer lattice structure, linearly crossed $\pi$ bands at Fermi level with electron-hole symmetry. Recently, we showed that the honeycomb structure with linear band crossings at Dirac points is also common to Si and Ge.[21, 20]

In an effort to make semimetallic graphene suitable for electronic applications, it has been functionalized to generate band gaps. It was theoretically shown that it is possible to induce band-gap opening produced by the adsorption of atomic hydrogen on graphene by choosing specific adsorption periodicity. [110] It was also experimentally shown that B- and N-doped graphenes can be synthesized to exhibit p- and n-type semiconducting properties that can be systematically tuned with the dopant concentration.[111] Effect of hydrogenation and the transition metal atom adsorption on the transport properties of graphene was also investigated theoretically.[19, 31] Using symmetry arguments and tight binding calculations it was shown that the periodic structure of defects (such as B and N impurities) on graphene can exhibit semimetallic and semiconductor behavior.[112] Moreover, weak perturbation potential forming a large hexagonal lattice in a two dimensional electron gas was shown to lead a massless Dirac fermion Hamiltonian with linearly crossing bands at Dirac points.[113, 114, 115]

A majority of the current studies on graphene is devoted to its chemical modification to create derivatives with different structures and properties. So far three known derivatives of graphene have been successfully achieved in chemical reactions: graphene oxide (GO), [66] graphane (CH)[41, 42, 36, 55] and recently fluorographene (CF).[74, 72, 65] Although GO is a wide band gap material that is important for device applications, its atomic structure, wherein the carbon atoms

are decorated with epoxides, alcohols and carboxylic acid groups, is not suitable for nanoscale manipulations. CH obtained by exposing carbon honeycomb structure to hydrogen plasma, is another example of the graphene-based chemical derivative. Upon the hydrogenation, semimetallic graphene is converted into an insulator. CF, the two dimensional counterpart of teflon, is the most recent focus of graphene research.

Much recently, the fabrication of large graphene sheets having high-density array of nanoscale holes, called graphene nanomeshes (GNMs),[116] has been the landmark in controlling the electronic properties at nanoscale. Additionally, the formation of one-dimensional periodic Stone-Wales type defects producing metallic nanowires on graphene matrix has also been reported.[117] These recent advances have made mesh configuration a controllable parameters to monitor physical properties of nanostructures. [116, 117, 118] Earlier, interesting effects of periodically repeating holes in the electronic and mechanical properties of graphene nanoribbons were predicted from the first-principles calculations.[107]

In this part of the thesis, we apply supercell method to reveal the electronic, magnetic and mechanical properties of graphene which is patterned by various adsorbates or holes. The atomic structure of all adsorbates and holes are obtained after extensive structure optimization. These periodically repeating superstructures or nanomeshes display properties which are rather different from those of graphene. We showed that not all patterns of adsorbates or hole with a 2D hexagonal lattice on graphene have linear band crossing, but only those which have a specific rotation symmetries. However, depending on the size of patterns or holes and the repeat periodicity, a GNM can be in different states ranging from to semiconducting including semimetallic with linear band crossing at the Fermi level.

## 8.2 Tight Binding Approximation and DFT

The present study revealed crucial effects of the point group symmetry of nanomesh on the resulting properties. Here, we start with a brief discussion of hexagonal symmetry and apply simple tight binding model of $\pi$-orbitals to reveal the effect of lattice symmetry on the band crossing.[119, 7] Graphene has the space group P6/mmm and point group symmetry $D_{6h}$. At the-$\Gamma$ point, the group of the wave vector is isomorphic to the point group $D_{6h}$.[120] However, irreducible representation of the wave vector point group turns into $D_{2h}$ and $D_{3h}$ at high symmetry points $M$ and $K$ (or $K'$), respectively. It was shown that the tight binding Hamiltonian with nearest neighbor hopping parameter, $t = 2.7$ eV

$$H = \sum_i \epsilon_i c_i^\dagger c_i + t \sum_{i,j} (c_i^\dagger c_j + H.c). \tag{8.1}$$

well approximates the $\pi$-bands of perfect graphene.[119, 7] Here $c_i^\dagger$ ($c_i$) is the creation (annihilation) operator of a $\pi$ electron at the lattice site $i$. The first term is the on-site energy of each carbon atom and equals to energy of the $2p_z$ orbital. Energy eigenvalues of graphene and other two hypothetical crystal having square and hexagonal lattices with single atom in the cell are calculated and the contour plots their energy band gap in BZ are shown in Fig.8.1. For graphene, energy dispersion is linear at the vicinity of the $K$- symmetry (Dirac) points and the Fermi velocity, which is linearly dependent to nearest neighbor interaction parameter, can be given by the expression $v_F = 3td/2\hbar$. [11]

Hypothetical square lattice has semimetallic band structure as in Fig. 8.1(b). In the reciprocal space the band gap is closed along the boundaries of squares. However, differing from graphene, these bands do not have linear dispersion. The structure having hexagonal lattice with single $\pi$-orbital per unitcell is shown in Fig.8.1(c). Such a structure having a single $\pi$-orbital in each unitcell may also be realized by adatom saturation of one type (A- or B-type) carbon atoms of graphene. In this case, structure has three-fold rotation symmetry and hence six nearest neighbors. In this case, while saturation yields a dramatic change in

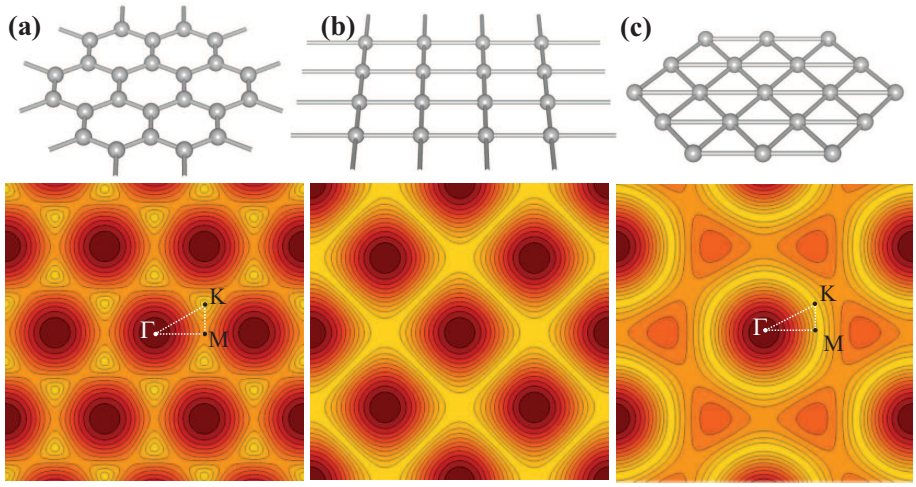


Figure 8.1: Contour plots for band gap. (a) Perfect graphene. (b) A crystal having square lattice with single atom in the unit cell. (c) A crystal having hexagonal lattice with a single atom in the unit cell. Band crossing occurs along the yellow/light contours on which the band gap becomes zero. Band gap takes its maximum value at brown/dark contours.

the electronic structure, linear band crossings at Fermi level still occur at the points on a circle of radius $R = \frac{4\pi}{3\sqrt{3}}$ in BZ. As shown in Fig. 8.1(c), this circle passes through the corners of hexagonal BZ of graphene. The Fermi velocity is calculated to be in the order of $10^6$ $m/s$ in the vicinity of band crossing points.

While the tight binding model allowed us to understand the general features of the band gap in different lattices, it fails to account for the reconstruction and rebonding near the defect. In the rest of the thesis we perform calculations from the first-principles to investigate various types of defects. To this end we carried out spin-polarized plane wave calculations[43, 44] using local density approximation (LDA)[47] and projector augmented wave (PAW)[46] potential. Patterns of defects are treated using supercell geometry, where a minimum of 10 Å vacuum spacing is kept between the adjacent graphene layers. Kinetic energy cutoff, Brillouin zone (BZ) sampling are determined after extensive convergence analysis. For the plane-wave basis set, the kinetic energy cutoff is taken to be $\hbar^2|\mathbf{k}+\mathbf{G}|^2/2m = 500$ eV. For partial occupancies Methfessel-Paxton smearing

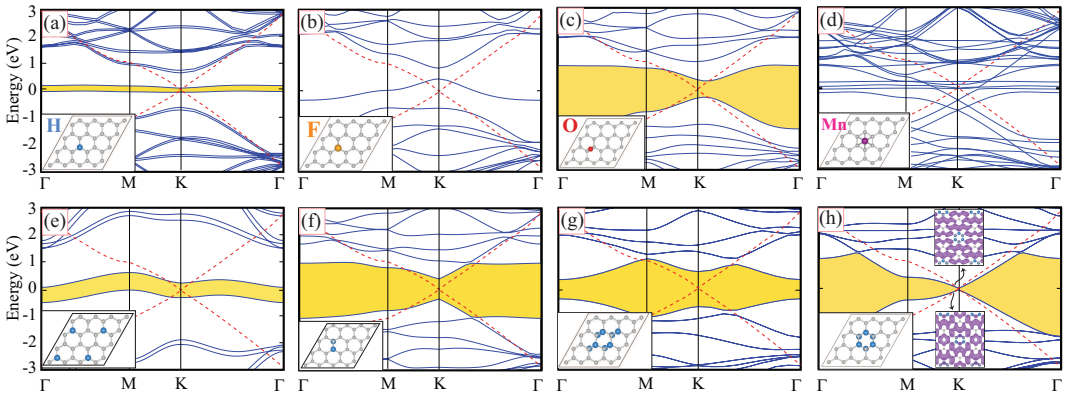


Figure 8.2: Spin-polarized energy band structure of a periodic patterns consisting of the (4x4) supercells each having a single (a) hydrogen; (b) fluorine; (c) oxygen; (d) manganese adatom. (e) A similar hydrogen pattern forming the (2x2) supercell on graphene host matrix allowing significant coupling between adatoms. (f-h) Periodic patterns of two, eight and six hydrogen atoms in the (4x4) graphene supercell, respectively. Isosurface of charge density of bands crossing near the $K$-point are shown by insets. For the sake of comparison, linearly crossing $\pi$ and $\pi^*$-bands of perfect graphene host matrix are also superimposed in the band structures. The zero of energy is set at the Fermi level $E_F$. The band gaps are shaded in yellow. All the bands presented in BZ corresponding to the (4x4) supercell.

method[121] is used. The convergence criterion of self-consistent field calculations is $10^{-5}$ eV for total energy values. By using the conjugate gradient method, all atomic positions and the size of unitcell were optimized until the atomic forces were less than 0.05 eV/Å. Pressures on the lattice unit cell are decreased to values less than 1 kB.

## 8.3 Adatom Patterned Graphene Nanomeshes

In this section we show how a periodic decoration of graphene by adatoms modifies the electronic structure. Here we considered H, F, O and Mn adatoms, which are adsorbed at different sites and form a (4x4) supercells on graphene host matrix as shown in Fig.8.2(a)-(d). We did not consider the interstitial or substitutional decoration, since experimental studies treating various foreign atoms, such as N,

O,H, F, C, Co, Fe and Gd, Au and Pt, revealed that these atoms prefer to be adsorbed at various sites on the surface of graphene, but none of them is adsorbed at the interstitial sites, nor is substituted for carbon atom [111, 66, 74, 41]

Owing to the unpaired electron, a single hydrogen adatom adsorbed to the (4x4) supercell has a spin polarized, semiconducting ground state with a net magnetic moment of $\mu$=1 $\mu_B$. Upon the adsorption of a hydrogen atom band structure of graphene changes dramatically. Instead of linear crossing of $\pi$ and $\pi^*$-bands at Fermi level, dispersionless impurity bands occurs with 0.1 eV indirect band gap. Similar to hydrogen atom, the most favorable adsorption site for a F atom on graphene is the top site of carbon atoms. Upon the adsorption of a F atom, $sp^2$ bondings of three C-C bonds below F atom are dehybridized and form tetrahedrally coordinated four $sp^3$ type bondings. Differing from the decoration of H adatom, ground state is nonmagnetic and as a result of odd number of electrons F decorated graphene becomes metalized as shown in Fig. 8.2(b). The band crossing at the K-points does not occur, since F adsorbed at the top of C atom changes the sixfold rotation symmetry to the threefold rotation symmetry.

Oxygen atom favors the bridge site between two underlying C atoms. Upon the adsorption of an oxygen at the bridge site two underlying C atoms become buckled by 0.36 Å. C-C and C-O bonds are calculated to be 1.51 and 1.44 Å, respectively. Resulting structure is a nonmagnetic semiconductor with 0.63 eV direct band gap (Fig. 8.2(c)). Valence and conduction band edges occurs between the $K$- and $\Gamma$-points. The adatom at the bridge site breaks the six fold rotation symmetry and hence hinders the linear band crossing.

The situation is different in the case of Mn, which is adsorbed above the center of a hexagon in graphene matrix and induces negligible deformation. Only six nearest C atoms raise slightly to higher (0.02 Å) position relative to the plane. Localized, non-bonding Mn-3$d$ orbitals form flat bands near the Fermi level. On the other hand, the sixfold rotation symmetry is maintained even after Mn atom adsorbed at the hollow site above the center of hexagon. Accordingly, the metallic structure with a net magnetic moment of 5 $\mu_B$ per cell allows linear crossing of graphene bands at the $K$-points in Fig. 8.2(d).

Having discussed the effect of periodic decoration by single adatoms, we next consider the periodic patterns of adatom groups. In Fig. 8.2(e) we show electronic band structure corresponding to relatively denser hydrogen coverage (C:H=8). Such a nanomesh created by one-sided decoration of four hydrogen atoms in the (4x4) supercell gives rise to a relatively dispersive bands and a net magnetic moment of 4 $\mu_B$ per supercell. Since the six fold rotation symmetry of graphene is broken by adsorbed H atoms, linear crossing of bands do not occur. In a decoration involving two sides of graphene, where two adjacent C atoms of different sublattices are saturated from different sides as shown in Fig. 8.2 (f). Since an equal number of A- and B-sublattice atoms are saturated, the structure is nonmagnetic semiconductor with a band gap of 0.8 eV. Another pattern derived from a graphane like domain consisting of 8 H atoms in Fig. 8.2(g) results in a band gap of 0.7 eV at Γ-point, but larger gap of 1 eV at the $K$-point. This nanomesh presents an electronic structure rather different both from graphene and graphane. The electronic structure is, however, different for a pattern of six H atoms, which saturate six carbon atoms at the corner a hexagon alternatingly from different sites; namely three of them adsorbed to A-sublattice from one side, remaining three adsorbed to B-sublattice from the other side. Even though sixfold rotation symmetry has changed to $S_6$ symmetry, both point group symmetries allow linear band crossing as seen in Fig. 8.2(h). This case demonstrates the crucial role played by the intrinsic symmetry of the pattern in determining the electronic structure. [114, 112, 113]

Let us now take a closer look at the triangular patterns of adatom groups that have hexagonal symmetry. In Fig. 8.3, we plot these $\pi$- and $\pi^*$-bands in the vicinity ($\Delta$k=0.03 Å$^{-1}$) of $K$-symmetry point for different patterns on supercells of different sizes; namely the (4x4) and (8x8) ($C_{128}$ and $C_{32}$) supercells. $H_6$ and $H_{12}$ patterns which have 0.06 and 0.09 eV band gap at $K$-point, indicates that the band gap opening increases with increasing pattern size and hence increasing coupling. In the (8x8) supercell the interaction between periodically repeating $H_6$ patterns is hindered and hence linear crossing of $\pi$- and $\pi^*$-bands at $K$-symmetry point similar to bare graphene is attained. By expressing these bands as $\mathbf{k} = \mathbf{K}+\mathbf{q}$ and by neglecting the second order terms with respect to $q^2$, the dispersion of

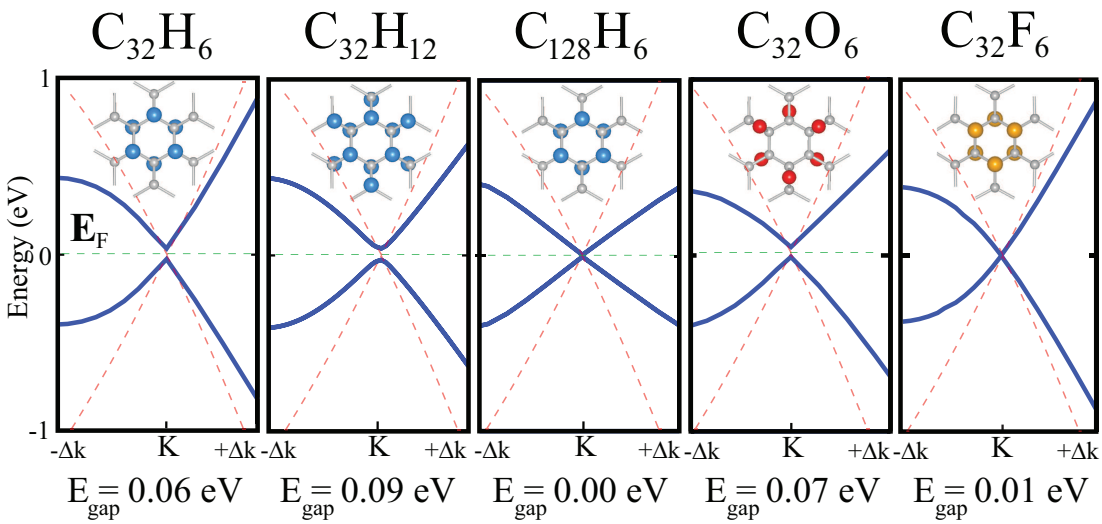


Figure 8.3: Band structures showing the effects of the coupling between various patterns as a function of their size and the size of mesh (supercell). The linearly crossing of $\pi$- and $\pi^*$-bands of graphene are shown by red/dashed lines.

the energy bands can be given as $E(\mathbf{q}) \simeq \mathbf{v_F}\hbar|\mathbf{q}|$. Here the Fermi velocity $v_F$ is calculated as 0.7x10$^6$ m/s (i.e. $\sim$ 0.6 of the Fermi velocity calculated for Dirac Fermions in perfect graphene).

We also present an example of $O_6$ pattern analogous to $H_{12}$ decoration of (4x4) supercell ($C_{32}H_{12}$) of graphene in Fig. 8.3. In this pattern three O atoms are bound alternatingly to bridge site at one site, the remaining three to other site. Here it is seen that denser O patterns are not favored due to strong O-O repulsion. Linear crossing of bands at $K$-point can also be achieved by O adatoms forming a periodically repeating $O_6$ pattern. Small band gap in Fig. 8.3 can be closed if the supercell size is increased to hinder coupling between them. This example implies that the patterns similar to that done by using H atoms can be created by the passivation of $p$-orbital electrons with O atoms. In the case of fluorination of (4x4) graphene by $F_6$ decoration, similar to $H_6$, linear $\pi$ and $\pi^*$-bands gets closer with very small (0.01 eV) band gap at $K$-point. Finally, the isosurface charge densities of these linearly crossing bands near $K$-point indicates that they mainly originate from graphene $\pi$-orbitals with small mixing from the adatom (see Fig. 8.2 (h)).

## 8.4 Hole Patterned Graphene Nanomeshes

Similar to adatom patterns on graphene, nanomeshes generated from the holes periodically patterned on graphene matrix exhibit also interesting features. This conclusion drawn from theoretical calculations are in line with the findings obtained from the fabrication of GNMs by means of block-copolymer assisted nanopatterning process. It has been shown that GNMs having high-density periodic array of holes display promising advantages relative to existing graphene devices.[116, 117] Thanks to the advances in the preparation of high quality nanoscale hard masks[116, 117] in laboratory conditions, theoretical studies in this field become more relevant for applications. Here we carry out calculations for the holes having 1-2 nm repeat period and 2-10 Å diameter. In Fig. 8.4(a) we describe the geometric parameters of $C_n$ hole defects forming a hexagonal lattice, where $n$ denotes number of C atoms removed from graphene matrix to make a hole. For nanoholes, we define the hole size as the maximum diameter of the $C_n$ hole defected region. After the creation of a $C_1$ defect (i.e. single C vacancy), Jahn-Teller type distortion changes the positions of surrounding C atoms slightly. The resulting structure attains a net magnetic moment of 1 $\mu_B$. The origin of magnetism in defected graphene sheets and the character of electronic states induced by the vacancy resulting in flat bands around Fermi level have been investigated by some recent studies.[52, 122] Upon the removal of C atoms ($n$>1) graphene is reconstructed to result in a significant modification in atomic configuration around the hole. For example, after the relaxation of atomic structure, $C_2$ defected region becomes an octagon-shaped hole surrounded by 2 pentagons and 6 hexagons. Similarly, as a result of Stone-Wales type transformation, each $C_4$ defect region also turns into a nonagon-shaped hole. As it was reported experimentally,[123] a hole region is surrounded by pentagonal and hexagonal rings of C atoms to keep the flatness of the sheet. While the honeycomb lattice symmetry of the graphene matrix does not change considerably for larger defects $C_6$ and $C_{24}$, hole region of $C_{12}$ takes almost a circular shape surrounded by regular pentagons and hexagons. Apparently, the trend in the shape of the hole region is determined by whether the edges of domain are zigzag or armchair shaped.

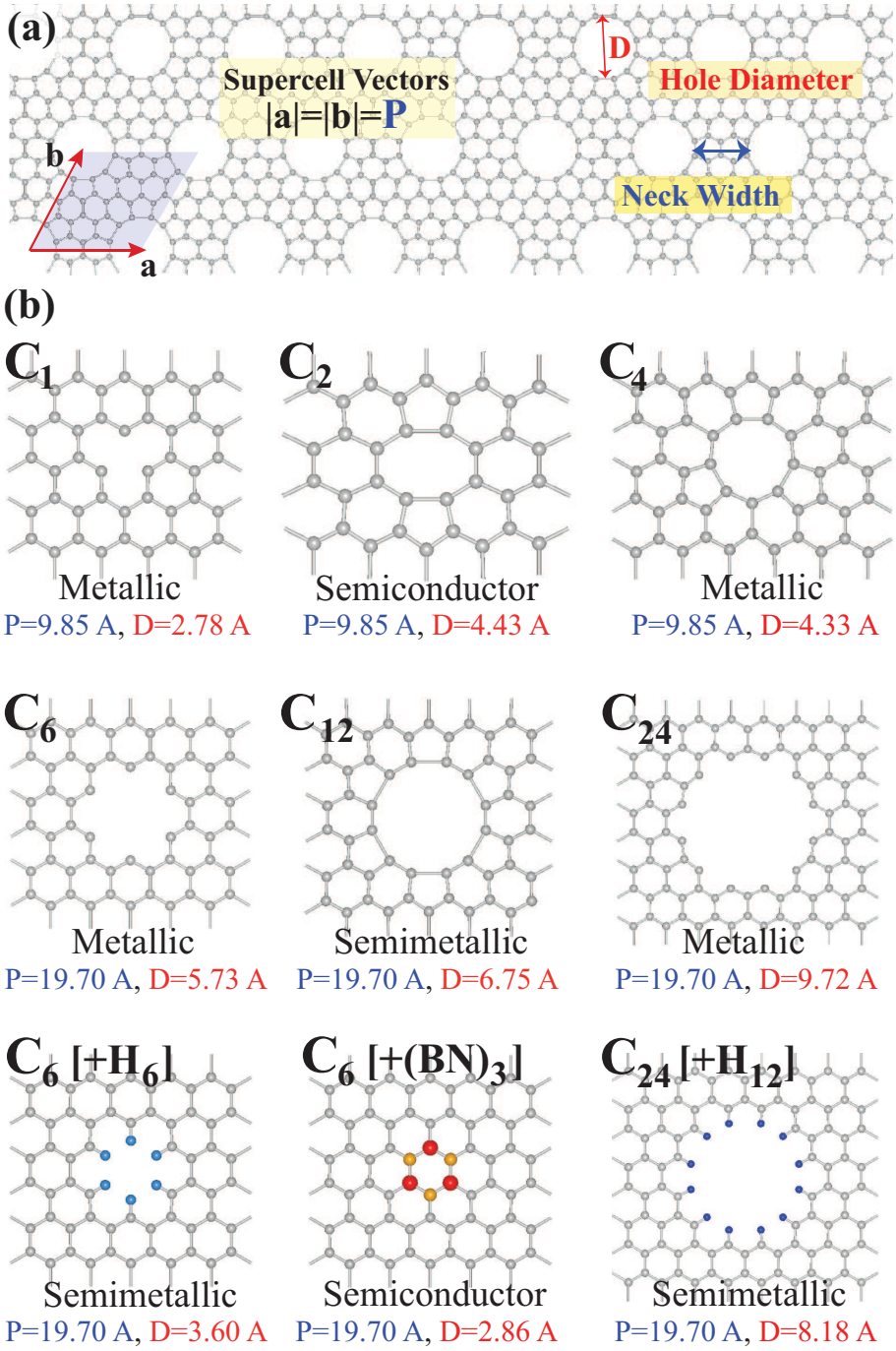


Figure 8.4: (a) Structural parameters for a nanomesh of $C_n$ hole. (b) Large supercells of hexagonal lattice each containing single hole of $C_1$, $C_2$, $C_4$, $C_6$, $C_{12}$, $C_{24}$. The nanomeshes in the third row are obtained by saturating $C_6$ and $C_{24}$ holes by hydrogen and also by B and N atoms alternatingly.

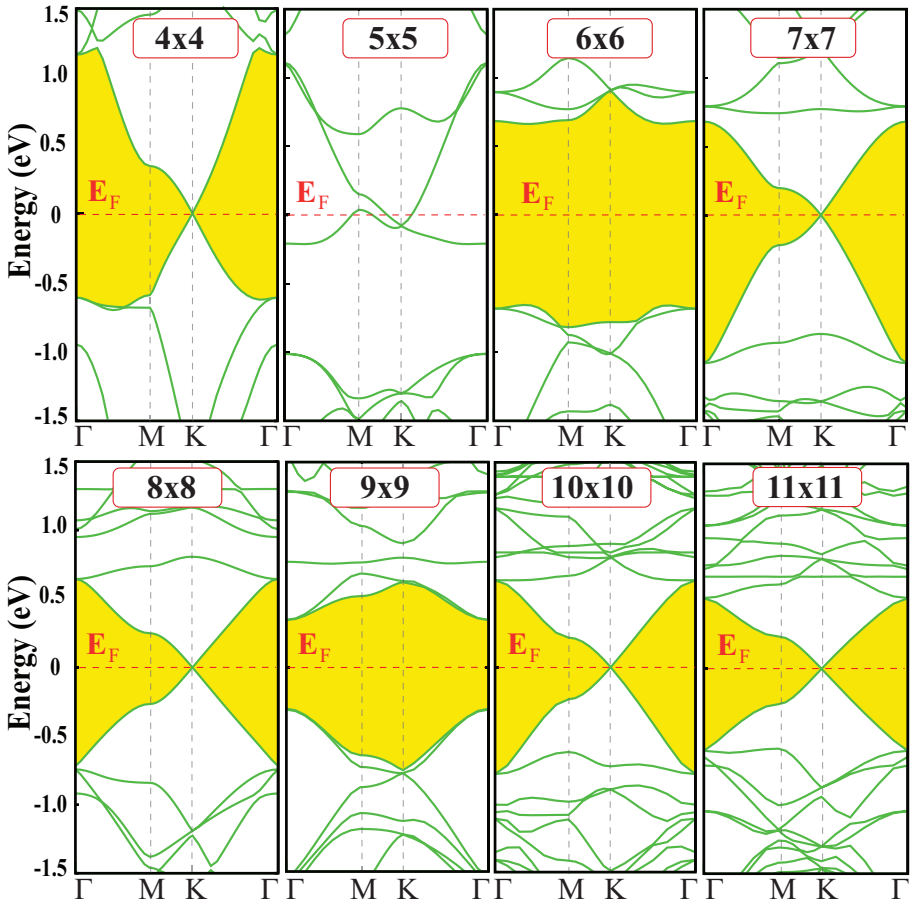


Figure 8.5: Band structure of nanomeshes of $C_{12}$ forming in the ($n$x$n$) supercells of graphene with $n$=4...11.

The energy band structures of graphene nanomeshes exhibit interesting variations with respect to their sizes, diameters and shapes of nanohole as illustrated in Fig.8.4 (b). While nanomesh of $C_1$ defect have metallic behavior, periodic structure of $C_2$ defect becomes indirect band gap semiconductor of 0.65 eV. However, $\pi$ and $\pi^*$-bands above the Fermi level still very close to each other (0.09 eV gap) at the $K$-point. $C_4$ defected GNM has metallic behavior. The situation becomes even more remarkable for larger defects $C_6$, $C_{12}$ and $C_{24}$. GNMs including either $C_6$ or $C_{24}$ hole have zigzag edges and are metals with antiferromagnetic (AFM) ground state. We note that the defect induced flat electronic bands around the Fermi level occur if the electron spins become unpaired. On the other hand, the reconstruction or the dimerization of carbon dangling bonds around the defect can cause the flat bands in the gap to disappear. Interestingly, nanomeshes of $C_6$ and $C_{24}$ holes, which are metallic, become semimetal upon the saturation of dangling bonds of carbon atoms around the hole by hydrogen atoms. This metal-semimetal transformation can have applications in graphene-based nanoelectronics. On the other hand, GNM of $C_6$ turns semiconducting with a band gap of 0.1 eV upon the termination of the dangling bonds of C atoms around the hole by B and N alternatingly to from a $B_3N_3$ hexagon. The band opening is explained by the breaking of sixfold symmetry due to $B_3N_3$ hexagon. The formation extended $B_nN_n$ honeycomb structure can be achieved directly in the course of epitaxial growth of graphene and single layer BN.[124]

As for GNM with $C_{12}$, it is a nonmagnetic semimetal because of carbon atoms at the edge are dimerized. The analysis of the orbital character of linearly crossing $\pi$- and $\pi^*$-bands near $K$-point using isosurface charge densities suggests that these bands originate from bonding and antibonding combinations of $\pi$- orbitals at the neck and around $C_6$ hole. Here we discuss an important aspect of GNMs with $C_{12}$, that the size of the hexagonal supercell or repeat periodicity of $C_{12}$ is crucial for the resulting electronic structure. Fig. 8.5 shows band structures of GNMs including single $C_{12}$ hole in the supercell of ($n$x$n$) where $n$=4...11. For $n$=4, GNM has the neck region consisting of single hexagon is a semimetal. For $n$=5, GNM is a metal and has a neck region which is relatively ticker, but its C-C bond angles strongly deviate from $120^o$. Surprisingly, GNM with $n$=6 is a semiconductor

having 1.3 eV band gap. The bond angles still continue to deviate from those of graphene. However, from $n$=7 on the bond angles at the neck region start to be graphene like with regular honeycomb structure. Both GNMs with $n$=7 and 8 are semimetals and have $\pi$- and $\pi^*$-bands which linearly cross at Fermi level at the $K$-point. Isosurface charge densities of these bands near $K$-points demonstrate that they, in fact, originate from the combination of graphene $\pi$-orbitals. As $n$ increases, GNM exhibit the similar trend for $n$=6-9; namely it is semiconductor for $n$=9, but semimetals for $n$=10 and 11. This variation of band gaps is reminiscent of the family behavior of graphene nanoribbons and is related to the variation of the thickness of necks between periodically repeating $C_{12}$ holes. Here, even if the six fold rotation symmetry is conserved, the band gap opens for every $n$=3x$N$ with $N$ being an integer $\geq 2$. However, this gap becomes smaller and eventually is closed as $n \to \infty$. We also note that the family like behavior of GNMs is related with the edge structure of the hole. In regard to the size of GNM of $C_{12}$, we note also that the lattice constants of corresponding ($n$x$n$) supercell is modified with size. For example, for $n$=11, the lattice constant of supercell is contracted by 1%, the contraction is 4% for $n$=5 and 40% for $n$=4.

Finally, in addition to triangular defect patterns, we also discuss the electronic structure of holes arranged in a rectangular lattice. In Fig. 8.6 we show the electronic band structures of $C_{12}$ nanomeshes realized by the supercells of (3x6), (4x8) and (5x10). While $C_{12}$ holes in a small rectangular supercells with small repeat periodicity (leading to significant coupling) become semiconducting, the semimetallic nature indigenous to graphene is achieved in large supercells. As shown in Fig. 8.6(c), even if the rotation symmetry required for band crossing is absent, graphene-like Bloch wave functions in the rectangular mesh of sparse patterns of $C_{12}$ holes show a semimetallic behavior. This indicates that as the size of the supercell becomes larger and the neck gets wider relative to the size of the hole, the symmetry requirement necessary for the linear band crossing can be relaxed.

## 8.5 Mechanical Properties of Nanomeshes

Honeycomb structure with $sp^2$ bonding underlies the unusual mechanical properties providing very high in-plane strength, but transversal flexibility. Here we investigate how the mechanical properties of nanomeshes generated with patterns of adatoms or holes. We focused on the harmonic range of the elastic deformation, where the structure responded to strain $\epsilon$ linearly. Here $\epsilon$ the elongation per unit length. The strain energy is defined as $E_s = E_T(\epsilon) - E_T(\epsilon = 0)$; namely, the total energy at a given strain $\epsilon$ minus the total energy at zero strain. Normally, the Young's modulus is the value, which characterizes the mechanical strength of a bulk material. Owing to ambiguities in defining the Young's modulus of two dimensional structures like a GNM, one can use in-plane stiffness $C = (1/A_0)\cdot(\partial^2 E_S/\partial\epsilon^2)$ in terms of the equilibrium area of the supercell, $A_0$.[125] We calculated the in-plane stiffness of graphene, and nanomeshes consisting of $C_{32}H_6$ , BN substituted graphene (i.e $C_{26}[(BN)_3]$ and $C_6$ hole in graphene using (4x4) supercell in Fig. 8.3. The stiffness of bare graphene is calculated to be 334 N/m, which is in good agreement with the experimental value of 340±50 N/m. Furthermore, the in-plane stiffness values of nanomeshes generated on graphene through $B_3N_3$ substitution, $H_6$ adatom pattern and $C_6$ hole are 308 N/m, 283 N/m and 167 N/m, respectively. Apparently, the bare graphene matrix is weakened by the formation of any of these nanomeshes. In addition to the calculation of in-plane stiffness, we extend our analysis to include the plastic deformation region, where the honeycomb like structure is destroyed after the yielding point (i.e. on set of plastic deformation), and GNM undergoes a massive structural deformation. Our preliminary simulations indicate that the yielding strain of $C_6$ hole GNM is significantly lower than the yielding strains of both $C_{26}[(BN)_3]$ and $C_{32}H_6$ GNMs.

While graphene and its various derivatives, GO, CH and CF, are important nanomaterials with diverse electronic, magnetic and mechanical properties, their properties can be modified and multiplied using different methods of functionalization. The most pronouncing property of graphene, namely linearly crossing

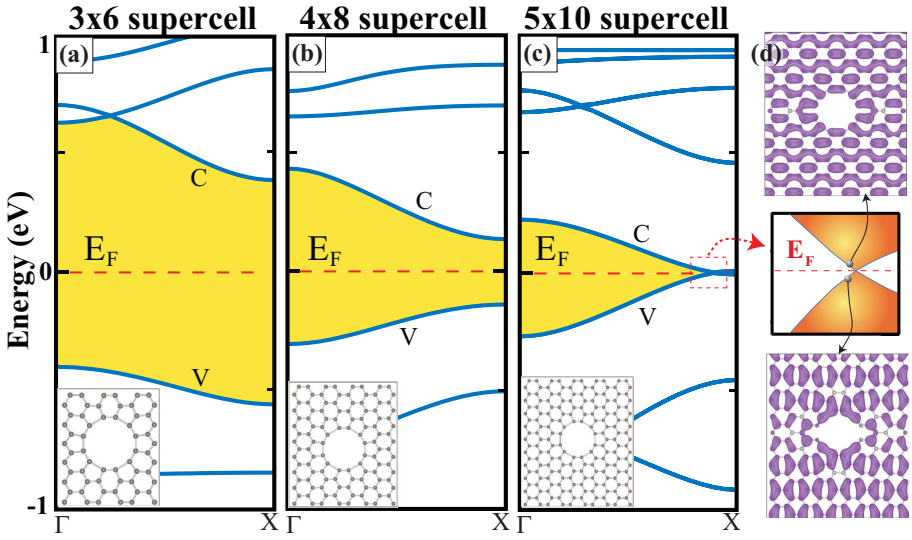


Figure 8.6: (a)-(c) Rectangular patterns of $C_{12}$ holes repeated in (3x6), (4x8) and (5x10) graphene supercells. Atomic structure of nanomeshes are given by inset. (d) Semimetallic electronic structure and isosurface charge densities of valence (V) and conduction (C) bands of (5x10) nanomesh are also shown.

bands at the Fermi level and electron-hole symmetry arising therefrom is usually destroyed, when graphene is functionalized through dopant or vacancy defects. In this work we demonstrated that the electron-hole symmetry, even Dirac Fermion behavior can be recovered for periodically repeating superstructures or nanomeshes having special point group symmetry. In this study we considered nanomeshes, which are generated by the decoration of adatoms, adatom groups or holes, which repeats periodically in graphene matrix. We found that types of adatoms and their patterns, the geometry of the holes of carbon atoms, the sizes and lattice symmetries of nanomesh provide us with several parameters to engineer the electronic and magnetic properties of the nanomesh. In particular, we showed that by varying only the size of the nanomesh including a specific hole one can tune between metallic and semiconducting state including semimetal with linearly crossing bands. This is reminiscent of the family behavior of graphene nanoribbons.

# Chapter 9

# Conclusion

This dissertation is devoted to the investigation of functionalized graphene materials and the prediction of novel stoichiometric graphene derivatives. Graphene's surfaces are quite suitable for chemical modifications and it can be converted to a material having entirely different electronic, magnetic, vibrational and mechanical properties. Very recent experimental studies have demonstrated that chemical conversion of graphene to its stoichiometric derivatives is possible by hydrogenation, fluorination and chlorination. Latest developments in experimental techniques have also shown that wellknown characteristic properties of graphene can be tuned by creation graphene nanomeshes having periodically ordered impruities or holes.

At the begining of thesis work, we dealt with the hydrogenated graphene, namely graphane. It was shown that the interaction between unpaired spins associated with H vacancies in graphane gives rise to interesting magnetic structures. Simple physical mechanisms underlying the magnetism of single-sided and double-sided vacancy domains were explained. At the end, the net magnetic moments can be attained in vacancy domains depending on their size and shape. Our results provide an elegant method for the magnetization of graphene by means of hydrogenation. While magnetic 2D systems attract a great deal of attention due to their tunable properties at nanoscale, our results suggest that the size and ordering of magnetic moments of hydrogen vacancy domains with thin walls can

be used for future data storage and spintronics applications.

Ultra-narrow nanoribbon forms graphene-like structures, as a one-dimensional media, are essential for graphene based-nanodevice applications. Our calculations revealed that of graphane nanoribbons have a number of important features and hence constitute basic structures to fabricate various devices. It was found that both the zigzag and armchair edged graphane nanoribbons are nonmagnetic wide band gap semiconductors. There is a strong dependence between band gap and ribbon width and the lots of the properties of graphene naoribbons can be tuned through H-passivation of their edges, adatom adsorption, vacancy creation, edge profiling and superlattice formation. In conclusion, the present study demonstrates that hydrogenated graphene nanoribbons can be an important basic nanomaterial and presents interesting properties for future technological applications.

Fluorographene is the two-dimensional and several-atom-thick counterpart of Teflon. Its graphene-like chemical inertness, thermal stability even at high temperatures and wide bandgap have attracted considerable interest on this material. Our analysis on fluorinated graphenes shows that different $C_nF$ structures can form at different level of F coverage. Relevant data reported in various experiments do not appear to agree with the properties calculated any one of the stable $C_nF$ structures. This finding lets us to conclude that domains of various $C_nF$ structures can form in the course of the fluorination of graphene. Therefore, the experimental data may reflect a weighted average of diverse $C_nF$ structures together with extended defects in grain boundaries. Our results show a wide range of interesting features of $C_nF$ structures. For example, a perfect CF structure is a stiff, nonmagnetic wide band gap nanomaterial having substantial surface charge. Moreover, unlike hydrogenated graphenes, one side fluorinated graphenes are found to be stable, which can be further functionalized by the adsorption of adatoms to other side. Lastly, the stability of the fluorinated surface of fluorographene and its interaction with foreign adsorbates were examined. It was found that atoms of nonmetals, alkali metals, alkaline earth metals, transition metals and metalloids can be grouped with respect to their adsorption on fluorographene. Interestingly, while the the alkali atoms Na and K bind very strongly to the fluorographene surface without disturbing its crystal structure, their diffusion take

place almost without barrier.

The most recent graphene derivative is the chlorinated graphene. Graphene's succesfull chlorination was reported only a few months ago. Motivated with the recent works on photochlorination of graphene, we carried out a first principle investigation of chlorination of graphene starting from single Cl adatom to fully chlorinated graphene. We found that at one sided chlorination adsorbed Cl atoms can migrate on the surface of graphene almost with no barrier. Formation of $Cl_2$ molecule from two individual migrating adatoms is energetically favorable. On the other hand, the configuration, where two Cl atoms which are adsorbed to adjacent carbon atoms in different sites are stable. Once the bare graphene is fully chlorinated from both side resulting in its buckling, the resulting conformation named as chlorographene, is a stable structure with various exceptional properties. With its 1.21 eV direct band gap, stiff mechanical properties and rapid response to homogeneous strain this new material can be used in diverse applications. However, this material may not be stable if it contains vacancy defects. The results obtained in this part of the thesis correct some erroneous conclusions drawn in earlier studies and illuminates some ambiguous points of experimental observation.

Nanoscale coatings have gained importance in the recent times due to the emergence of nanoscale devices that are quite sensitive to enviromental factors. Extremely strong lattice structure of graphene can be considered as an ideal coating material. As a nanocoating application of graphene, we demonstrated that continuous coating of pristine graphene on reactive surfaces can provide for an excellent protection from oxidation of reactive surfaces at nanoscale. The binding of oxygen atom at low coordinated carbon atoms is rather high, but their barrier to penetrate to the reactive surface under graphene is low. Therefore discontinuities in graphene coating or defects, such as vacancies or holes weaken the protection from oxidation by creating spots on the coating with low oxidation barrier. This limitation can be circumvented by coating of bilayer or preferably graphene sheets comprising a few graphene layers, which provides even more effective protection. At macroscale, our results suggests that graphene additives can improve the strength of antioxidant paints. Graphene coating, which is thin

at the atomic scale can also serve as a natural barrier between environment and solid surfaces for other atoms.

Graphene's exceptional features originates from the hexagonal symmetry and these can be tuned by various functionalization techniques. Though the semimetallic graphene, which has a zero band gap, allows relativistic carrier mobility, from the viewpoint of requirements for nanodevices it becomes useless as a semiconductor to amplify or switch electronic signals. However, the inert and strong monolayer structure of graphene provides an ideal playground for its functionalization. In the last part of my thesis, motivated by the recently reported state of the art methods for fabricating high density periodic nanoscale defects in graphene, the structural, mechanical and electronic properties of defect-patterned graphene nanomeshes are investigated. It is found that various patterns of adatom groups yield metallic or semimetallic, even semiconducting behavior and specific patterns can be in a magnetic state. Even though the patterns of single adatoms dramatically alter the electronic structure of graphene, adatom groups of specific symmetry can maintain the Dirac fermion behavior. Nanoholes forming nanomesh are also investigated. Depending on the interplay between the repeat periodicity and the geometry of the hole, the nanomesh can be in different states ranging from metallic to semiconducting including semimetallic state with the bands crossing linearly at the Fermi level. We showed that forming periodically repeating superstructures in graphene matrix can develop a promising technique to engineer nanomaterials with desired electronic and magnetic properties.

The subject matter of my thesis is the investigation of structural, electronic, magnetic, mechanical and vibrational properties of various stoichiometric derivatives of graphene. Our studies reveal a lot of important features such as tunable bandgap, tunable magnetization, strong and flexible lattice structure and strain dependent features of hydrogenated, fluorinated and chlorinated graphenes. The studies presented here focuses on the materials that have been synthesized in just a few years, and will shed light on the enormous potential of functionalized graphenes and graphene derivatives.

# Bibliography


[1] W. Kohn and L. J. Sham. Self-consistent equations including exchange and correlation effects. *Phys. Rev.*, 140:A1133–A1138, Nov 1965.

[2] P. Hohenberg and W. Kohn. Inhomogeneous electron gas. *Phys. Rev.*, 136:B864–B871, Nov 1964.

[3] R. P. Feynman. Forces in molecules. *Phys. Rev.*, 56:340–343, Aug 1939.

[4] Dario Alfe. PHON: A program to calculate phonons using the small displacement method. *COMPUTER PHYSICS COMMUNICATIONS*, 180(12):2622–2633, DEC 2009.

[5] Stefano Baroni, Stefano de Gironcoli, Andrea Dal Corso, and Paolo Giannozzi. Phonons and related crystal properties from density-functional perturbation theory. *Rev. Mod. Phys.*, 73:515–562, Jul 2001.

[6] KS Novoselov, AK Geim, SV Morozov, D Jiang, Y Zhang, SV Dubonos, IV Grigorieva, and AA Firsov. Electric field effect in atomically thin carbon films. *SCIENCE*, 306(5696):666–669, OCT 22 2004.

[7] P. R. Wallace. The band theory of graphite. *Phys. Rev.*, 71:622–634, May 1947.

[8] KS Novoselov, D Jiang, F Schedin, TJ Booth, VV Khotkevich, SV Morozov, and AK Geim. Two-dimensional atomic crystals. *PROCEEDINGS OF THE NATIONAL ACADEMY OF SCIENCES OF THE UNITED STATES OF AMERICA*, 102(30):10451–10453, JUL 26 2005.

[9] YB Zhang, YW Tan, HL Stormer, and P Kim. Experimental observation of the quantum Hall effect and Berry's phase in graphene. *NATURE*, 438(7065):201–204, NOV 10 2005.

[10] Claire Berger, Zhimin Song, Xuebin Li, Xiaosong Wu, Nate Brown, Cecile Naud, Didier Mayou, Tianbo Li, Joanna Hass, Atexei N. Marchenkov, Edward H. Conrad, Phillip N. First, and Wait A. de Heer. Electronic confinement and coherence in patterned epitaxial graphene. *SCIENCE*, 312(5777):1191–1196, MAY 26 2006.

[11] A. H. Castro Neto, F. Guinea, N. M. R. Peres, K. S. Novoselov, and A. K. Geim. The electronic properties of graphene. *Rev. Mod. Phys.*, 81:109–162, Jan 2009.

[12] Motohiko Ezawa. Peculiar width dependence of the electronic properties of carbon nanoribbons. *Phys. Rev. B*, 73:045432, Jan 2006.

[13] Katsuyoshi Kobayashi. Electronic structure of a stepped graphite surface. *Phys. Rev. B*, 48:1757–1760, Jul 1993.

[14] Kyoko Nakada, Mitsutaka Fujita, Gene Dresselhaus, and Mildred S. Dresselhaus. Edge state in graphene ribbons: Nanometer size effect and edge shape dependence. *Phys. Rev. B*, 54:17954–17961, Dec 1996.

[15] Katsunori Wakabayashi, Mitsutaka Fujita, Hiroshi Ajiki, and Manfred Sigrist. Electronic and magnetic properties of nanographite ribbons. *Phys. Rev. B*, 59:8271–8282, Mar 1999.

[16] P. O. Lehtinen, A. S. Foster, A. Ayuela, A. Krasheninnikov, K. Nordlund, and R. M. Nieminen. Magnetic properties and diffusion of adatoms on a graphene sheet. *Phys. Rev. Lett.*, 91:017202, Jun 2003.

[17] K. Nordlund, J. Keinonen, and T. Mattila. Formation of ion irradiation induced small-scale defects on graphite surfaces. *Phys. Rev. Lett.*, 77:699–702, Jul 1996.

[18] Elizabeth J. Duplock, Matthias Scheffler, and Philip J. D. Lindan. Hallmark of perfect graphene. *Phys. Rev. Lett.*, 92:225502, Jun 2004.

[19] H. Şahin and R. T. Senger. First-principles calculations of spin-dependent conductance of graphene flakes. *Phys. Rev. B*, 78:205423, Nov 2008.

[20] H. Şahin, S. Cahangirov, M. Topsakal, E. Bekaroglu, E. Akturk, R. T. Senger, and S. Ciraci. Monolayer honeycomb structures of group-iv elements and iii-v binary compounds: First-principles calculations. *Phys. Rev. B*, 80:155453, Oct 2009.

[21] S. Cahangirov, M. Topsakal, E. Aktürk, H. Şahin, and S. Ciraci. Two- and one-dimensional honeycomb structures of silicon and germanium. *Phys. Rev. Lett.*, 102:236804, Jun 2009.

[22] Melinda Y. Han, Barbaros Özyilmaz, Yuanbo Zhang, and Philip Kim. Energy band-gap engineering of graphene nanoribbons. *Phys. Rev. Lett.*, 98:206805, May 2007.

[23] Xiaolin Li, Xinran Wang, Li Zhang, Sangwon Lee, and Hongjie Dai. Chemically derived, ultrasmooth graphene nanoribbon semiconductors. *Science*, 319(5867):1229–1232, 2008.

[24] Young-Woo Son, Marvin L. Cohen, and Steven G. Louie. Energy gaps in graphene nanoribbons. *Phys. Rev. Lett.*, 97:216803, Nov 2006.

[25] Dmitry A. Abanin, Patrick A. Lee, and Leonid S. Levitov. Spin-filtered edge states and quantum hall effect in graphene. *Phys. Rev. Lett.*, 96:176803, May 2006.

[26] Hosik Lee, Young-Woo Son, Noejung Park, Seungwu Han, and Jaejun Yu. Magnetic ordering at the edges of graphitic fragments: Magnetic tail interactions between the edge-localized states. *Phys. Rev. B*, 72:174431, Nov 2005.

[27] Yoshiyuki Miyamoto, Kyoko Nakada, and Mitsutaka Fujita. First-principles study of edge states of h-terminated graphitic ribbons. *Phys. Rev. B*, 59:9858–9861, Apr 1999.

[28] Alessandro Cresti, Giuseppe Grosso, and Giuseppe Pastori Parravicini. Numerical study of electronic transport in gated graphene ribbons. *Phys. Rev. B*, 76:205433, Nov 2007.

[29] H. Sevinçli, M. Topsakal, E. Durgun, and S. Ciraci. Electronic and magnetic properties of $3d$ transition-metal atom adsorbed graphene and graphene nanoribbons. *Phys. Rev. B*, 77:195434, May 2008.

[30] T. B. Martins, R. H. Miwa, Antônio J. R. da Silva, and A. Fazzio. Electronic and transport properties of boron-doped graphene nanoribbons. *Phys. Rev. Lett.*, 98:196803, May 2007.

[31] H. Sahin, R. T. Senger, and S. Ciraci. Spintronic properties of zigzag-edged triangular graphene flakes. *Journal of Applied Physics*, 108(7):074301, 2010.

[32] Jia-An Yan, W. Y. Ruan, and M. Y. Chou. Phonon dispersions and vibrational properties of monolayer, bilayer, and trilayer graphene: Density-functional perturbation theory. *Phys. Rev. B*, 77:125401, Mar 2008.

[33] P. G. Klemens. Theory of thermal conduction in thin ceramic films. *International Journal of Thermophysics*, 22:265–275, 2001. 10.1023/A:1006776107140.

[34] A. C. Ferrari, J. C. Meyer, V. Scardaci, C. Casiraghi, M. Lazzeri, F. Mauri, S. Piscanec, D. Jiang, K. S. Novoselov, S. Roth, and A. K. Geim. Raman spectrum of graphene and graphene layers. *Phys. Rev. Lett.*, 97:187401, Oct 2006.

[35] S. Piscanec, M. Lazzeri, Francesco Mauri, A. C. Ferrari, and J. Robertson. Kohn anomalies and electron-phonon interactions in graphite. *Phys. Rev. Lett.*, 93:185503, Oct 2004.

[36] H. Sahin, C. Ataca, and S. Ciraci. Magnetization of graphane by dehydrogenation. *APPLIED PHYSICS LETTERS*, 95(22):222510, NOV 30 2009.

[37] N. M. R. Peres, A. H. Castro Neto, and F. Guinea. Conductance quantization in mesoscopic graphene. *Phys. Rev. B*, 73:195411, May 2006.

[38] H. Sevinçli, M. Topsakal, E. Durgun, and S. Ciraci. Electronic and magnetic properties of $3d$ transition-metal atom adsorbed graphene and graphene nanoribbons. *Phys. Rev. B*, 77:195434, May 2008.

[39] E. Durgun, S. Ciraci, W. Zhou, and T. Yildirim. Transition-metal-ethylene complexes as high-capacity hydrogen-storage media. *Phys. Rev. Lett.*, 97:226102, Nov 2006.

[40] C. Ataca, E. Aktürk, and S. Ciraci. Hydrogen storage of calcium atoms adsorbed on graphene: First-principles plane wave calculations. *Phys. Rev. B*, 79:041406, Jan 2009.

[41] D. C. Elias, R. R. Nair, T. M. G. Mohiuddin, S. V. Morozov, P. Blake, M. P. Halsall, A. C. Ferrari, D. W. Boukhvalov, M. I. Katsnelson, A. K. Geim, and K. S. Novoselov. Control of graphene's properties by reversible hydrogenation: Evidence for graphane. *Science*, 323(5914):610–613, 2009.

[42] Jorge O. Sofo, Ajay S. Chaudhari, and Greg D. Barber. Graphane: A two-dimensional hydrocarbon. *Phys. Rev. B*, 75:153401, Apr 2007.

[43] G KRESSE and J HAFNER. ABINITIO MOLECULAR-DYNAMICS FOR LIQUID-METALS. *PHYSICAL REVIEW B*, 47(1):558–561, JAN 1 1993.

[44] G Kresse and J Furthmuller. Efficient iterative schemes for ab initio total-energy calculations using a plane-wave basis set. *PHYSICAL REVIEW B*, 54(16):11169–11186, OCT 15 1996.

[45] M. Shishkin and G. Kresse. Implementation and performance of the frequency-dependent GW method within the PAW framework. *PHYSICAL REVIEW B*, 74(3):035101, JUL 2006.

[46] PE BLOCHL. PROJECTOR AUGMENTED-WAVE METHOD. *PHYSICAL REVIEW B*, 50(24):17953–17979, DEC 15 1994.

[47] DM CEPERLEY and BJ ALDER. GROUND-STATE OF THE ELECTRON-GAS BY A STOCHASTIC METHOD. *PHYSICAL REVIEW LETTERS*, 45(7):566–569, 1980.

[48] Zhiheng Liu, L. C. Feldman, N. H. Tolk, Zhenyu Zhang, and P. I. Cohen. Desorption of h from si(111) by resonant excitation of the si-h vibrational stretch mode. *Science*, 312(5776):1024–1026, 2006.

[49] L. Breaux, B. Anthony, T. Hsu, S. Banerjee, and A. Tasch. Homoepitaxial films grown on si (100) at 150 [degree]c by remote plasma-enhanced chemical vapor deposition. *Applied Physics Letters*, 55(18):1885–1887, 1989.

[50] E. Durgun, R. T. Senger, H. Mehrez, H. Sevincli, and S. Ciraci. Size-dependent alternation of magnetoresistive properties in atomic chains. *The Journal of Chemical Physics*, 125(12):121102, 2006.

[51] Hosik Lee, Young-Woo Son, Noejung Park, Seungwu Han, and Jaejun Yu. Magnetic ordering at the edges of graphitic fragments: Magnetic tail interactions between the edge-localized states. *Phys. Rev. B*, 72:174431, Nov 2005.

[52] Elliott H. Lieb. Two theorems on the hubbard model. *Phys. Rev. Lett.*, 62:1201–1204, Mar 1989.

[53] H. Şahin, C. Ataca, and S. Ciraci. Electronic and magnetic properties of graphane nanoribbons. *Phys. Rev. B*, 81:205417, May 2010.

[54] Veronica Barone, Oded Hod, and Gustavo E. Scuseria. Electronic structure and stability of semiconducting graphene nanoribbons. *Nano Letters*, 6(12):2748, 2006.

[55] M Z S Flores, P A S Autreto, S B Legoas, and D S Galvao. Graphene to graphane: a theoretical study. *Nanotechnology*, 20(46):465704, 2009.

[56] Yafei Li, Zhen Zhou, Panwen Shen, and Zhongfang Chen. Structural and electronic properties of graphane nanoribbons. *The Journal of Physical Chemistry C*, 113(33):15043–15045, 2009.

[57] S. Lebègue, M. Klintenberg, O. Eriksson, and M. I. Katsnelson. Accurate electronic band gap of pure and functionalized graphane from gw calculations. *Phys. Rev. B*, 79:245117, Jun 2009.

[58] F. Fuchs, J. Furthmüller, F. Bechstedt, M. Shishkin, and G. Kresse. Quasiparticle band structure based on a generalized kohn-sham scheme. *Phys. Rev. B*, 76(11):115109, Sep 2007.

[59] Mads R. Sørensen, Mads Brandbyge, and Karsten W. Jacobsen. Mechanical deformation of atomic-scale metallic contacts: Structure and mechanisms. *Phys. Rev. B*, 57:3283–3294, Feb 1998.

[60] M. Evaldsson, I. V. Zozoulenko, Hengyi Xu, and T. Heinzel. Edge-disorder-induced anderson localization and conduction gap in graphene nanoribbons. *Phys. Rev. B*, 78:161407, Oct 2008.

[61] Kevin T. Chan, J. B. Neaton, and Marvin L. Cohen. First-principles study of metal adatom adsorption on graphene. *Phys. Rev. B*, 77:235430, Jun 2008.

[62] Bhalchandra S. Pujari and D. G. Kanhere. Density functional investigations of defect-induced mid-gap states in graphane. *The Journal of Physical Chemistry C*, 113(50):21063–21067, 2009.

[63] H. Sevinçli, M. Topsakal, and S. Ciraci. Superlattice structures of graphene-based armchair nanoribbons. *Phys. Rev. B*, 78:245402, Dec 2008.

[64] Xiaolin Li, Xinran Wang, Li Zhang, Sangwon Lee, and Hongjie Dai. Chemically derived, ultrasmooth graphene nanoribbon semiconductors. *Science*, 319(5867):1229–1232, 2008.

[65] H. Şahin, M. Topsakal, and S. Ciraci. Structures of fluorinated graphene and their signatures. *Phys. Rev. B*, 83:115432, Mar 2011.

[66] Dikin D.A. Piner R.D. Kohlhaas K.A. Kleinhammes A. Jia Y. Wu Y. Nguyen S.T. Ruoff R.S. Stankovich, S. Synthesis of graphene-based nanosheets via chemical reduction of exfoliated graphite oxide. *Carbon*, 45(7):1558–1565, 2007. cited By (since 1996) 1025.

[67] Dmitriy A. Dikin, Sasha Stankovich, Eric J. Zimney, Richard D. Piner, Geoffrey H. B. Dommett, Guennadi Evmenenko, SonBinh T. Nguyen, and

Rodney S. Ruoff. Preparation and characterization of graphene oxide paper. *NATURE*, 448(7152):457–460, JUL 26 2007.

[68] M. Topsakal, S. Cahangirov, and S. Ciraci. The response of mechanical and electronic properties of graphane to the elastic strain. *Applied Physics Letters*, 96(9):091912, 2010.

[69] J.-C. Charlier, X. Gonze, and J.-P. Michenaud. First-principles study of graphite monofluoride $(cf)_n$. *Phys. Rev. B*, 47:16162–16168, Jun 1993.

[70] Yoshiteru Takagi and Koichi Kusakabe. Transition from direct band gap to indirect band gap in fluorinated carbon. *Phys. Rev. B*, 65:121103, Mar 2002.

[71] D.W. and Boukhvalov. Stable antiferromagnetic graphone. *Physica E: Low-dimensional Systems and Nanostructures*, 43(1):199 – 201, 2010.

[72] S.-H. Cheng, K. Zou, F. Okino, H. R. Gutierrez, A. Gupta, N. Shen, P. C. Eklund, J. O. Sofo, and J. Zhu. Reversible fluorination of graphene: Evidence of a two-dimensional wide bandgap semiconductor. *Phys. Rev. B*, 81:205435, May 2010.

[73] Jeremy T. Robinson, James S. Burgess, Chad E. Junkermeier, Stefan C. Badescu, Thomas L. Reinecke, F. Keith Perkins, Maxim K. Zalalutdniov, Jeffrey W. Baldwin, James C. Culbertson, Paul E. Sheehan, and Eric S. Snow. Properties of fluorinated graphene films. *Nano Letters*, 10(8):3001–3005, 2010.

[74] Rahul R. Nair, Wencai Ren, Rashid Jalil, Ibtsam Riaz, Vasyl G. Kravets, Liam Britnell, Peter Blake, Fredrik Schedin, Alexander S. Mayorov, Shengjun Yuan, Mikhail I. Katsnelson, Hui-Ming Cheng, Wlodek Strupinski, Lyubov G. Bulusheva, Alexander V. Okotrub, Irina V. Grigorieva, Alexander N. Grigorenko, Kostya S. Novoselov, and Andre K. Geim. Fluorographene: A two-dimensional counterpart of teflon. *Small*, 6(24):2877–2884, 2010.

[75] O. Leenaerts, H. Peelaers, A. D. Hernández-Nieves, B. Partoens, and F. M. Peeters. First-principles investigation of graphene fluoride and graphane. *Phys. Rev. B*, 82:195436, Nov 2010.

[76] F. Withers, M. Dubois, and A. K. Savchenko. Electron properties of fluorinated single-layer graphene transistors. *Phys. Rev. B*, 82:073403, Aug 2010.

[77] M. Klintenberg, S. Lebègue, M. I. Katsnelson, and O. Eriksson. Theoretical analysis of the chemical bonding and electronic structure of graphene interacting with group ia and group viia elements. *Phys. Rev. B*, 81:085433, Feb 2010.

[78] C. Ataca, E. Akturk, H. Sahin, and S. Ciraci. Adsorption of carbon adatoms to graphene and its nanoribbons. *Journal of Applied Physics*, 109(1):013704, 2011.

[79] Jochen Heyd, Gustavo E. Scuseria, and Matthias Ernzerhof. Hybrid functionals based on a screened coulomb potential. *The Journal of Chemical Physics*, 118(18):8207–8215, 2003.

[80] G Henkelman, A Arnaldsson, and H Jonsson. A fast and robust algorithm for Bader decomposition of charge density. *COMPUTATIONAL MATERIALS SCIENCE*, 36(3):354–360, JUN 2006.

[81] R. S. Mulliken. Electronic population analysis on lcao[single bond]mo molecular wave functions. ii. overlap populations, bond orders, and covalent bond energies. *The Journal of Chemical Physics*, 23(10):1841–1846, 1955.

[82] *The results pertaining to this chapter submitted for publication in Physical Review B.*

[83] Ning Shen and Jorge O. Sofo. Dispersion of edge states and quantum confinement of electrons in graphene channels drawn on graphene fluoride. *Phys. Rev. B*, 83:245424, Jun 2011.

[84] Jeremy T. Robinson, James S. Burgess, Chad E. Junkermeier, Stefan C. Badescu, Thomas L. Reinecke, F. Keith Perkins, Maxim K. Zalalutdniov,

Jeffrey W. Baldwin, James C. Culbertson, Paul E. Sheehan, and Eric S. Snow. Properties of fluorinated graphene films. *Nano Letters*, 10(8):3001–3005, 2010.

[85] Bo Li, Lin Zhou, Di Wu, Hailin Peng, Kai Yan, Yu Zhou, and Zhongfan Liu. Photochemical chlorination of graphene. *ACS Nano*, 5(7):5957–5961, 2011.

[86] Paulo V C Medeiros, Artur J S Mascarenhas, F de Brito Mota, and Caio M C de Castilho. A dft study of halogen atoms adsorbed on graphene layers. *Nanotechnology*, 21(48):485701, 2010.

[87] Radek Zboril, FrantiÅ¡ek Karlicky, Athanasios B. Bourlinos, Theodore A. Steriotis, Athanasios K. Stubos, Vasilios Georgakilas, Klara Safarova, Dalibor Jancik, Christos Trapalis, and Michal Otyepka. Graphene fluoride: A stable stoichiometric graphene derivative and its chemical conversion to graphene. *Small*, 6(24):2885–2891, 2010.

[88] John P. Perdew, Kieron Burke, and Matthias Ernzerhof. Generalized gradient approximation made simple. *Phys. Rev. Lett.*, 77:3865–3868, Oct 1996.

[89] Stefan Grimme. Semiempirical GGA-type density functional constructed with a long-range dispersion correction. *JOURNAL OF COMPUTATIONAL CHEMISTRY*, 27(15):1787–1799, NOV 30 2006.

[90] Prashant Dhiman, Fazel Yavari, Xi Mi, Hemtej Gullapalli, Yunfeng Shi, Pulickel M. Ajayan, and Nikhil Koratkar. Harvesting energy from water flow over graphene. *Nano Letters*, 11(8):3123–3127, 2011.

[91] M. Topsakal, E. Aktürk, and S. Ciraci. First-principles study of two- and one-dimensional honeycomb structures of boron nitride. *Phys. Rev. B*, 79:115442, Mar 2009.

[92] C. Ataca, M. Topsakal, E. Akturk, and S. Ciraci. A comparative study of lattice dynamics of three- and two-dimensional mos2. *The Journal of Physical Chemistry C*, 115(33):16354–16361, 2011.

[93] F. G. Allen and G. W. Gobeli. Work function, photoelectric threshold, and surface states of atomically clean silicon. *Phys. Rev.*, 127:150–158, Jul 1962.

[94] R. Ditchfield, D. Llera-Rodriguez, and E. G. Seebauer. Semiconductor surface diffusion: Nonthermal effects of photon illumination. *Phys. Rev. B*, 61:13710–13720, May 2000.

[95] H. Şahin and S. Ciraci. Structural, mechanical, and electronic properties of defect-patterned graphene nanomeshes from first principles. *Phys. Rev. B*, 84:035452, Jul 2011.

[96] Shanshan Chen, Lola Brown, Mark Levendorf, Weiwei Cai, Sang-Yong Ju, Jonathan Edgeworth, Xuesong Li, Carl W. Magnuson, Aruna Velamakanni, Richard D. Piner, Junyong Kang, Jiwoong Park, and Rodney S. Ruoff. Oxidation resistance of graphene-coated cu and cu/ni alloy. *ACS Nano*, 5(2):1321–1327, 2011.

[97] Jongweon Cho, Li Gao, Jifa Tian, Helin Cao, Wei Wu, Qingkai Yu, Esmeralda N. Yitamben, Brandon Fisher, Jeffrey R. Guest, Yong P. Chen, and Nathan P. Guisinger. Atomic-scale investigation of graphene grown on cu foil and the effects of thermal annealing. *ACS Nano*, 5(5):3607–3613, 2011.

[98] Paolo Giannozzi, Stefano Baroni, Nicola Bonini, Matteo Calandra, Roberto Car, Carlo Cavazzoni, Davide Ceresoli, Guido L Chiarotti, Matteo Cococcioni, Ismaila Dabo, Andrea Dal Corso, Stefano de Gironcoli, Stefano Fabris, Guido Fratesi, Ralph Gebauer, Uwe Gerstmann, Christos Gougoussis, Anton Kokalj, Michele Lazzeri, Layla Martin-Samos, Nicola Marzari, Francesco Mauri, Riccardo Mazzarello, Stefano Paolini, Alfredo Pasquarello, Lorenzo Paulatto, Carlo Sbraccia, Sandro Scandolo, Gabriele Sclauzero, Ari P Seitsonen, Alexander Smogunov, Paolo Umari, and Renata M Wentzcovitch. Quantum espresso: a modular and open-source software project for quantum simulations of materials. *Journal of Physics: Condensed Matter*, 21(39):395502 (19pp), 2009.

[99] J. K. Grepstad, P. O. Gartland, and B. J. Slagsvold. Anisotropic work function of clean and smooth low-index faces of aluminium. *Surface Science*, 57(1):348–362, 1976.

[100] Zhongqing Wei, Debin Wang, Suenne Kim, Soo-Young Kim, Yike Hu, Michael K. Yakes, Arnaldo R. Laracuente, Zhenting Dai, Seth R. Marder, Claire Berger, William P. King, Walter A. de Heer, Paul E. Sheehan, and Elisa Riedo. Nanoscale tunable reduction of graphene oxide for graphene electronics. *Science*, 328(5984):1373–1376, 2010.

[101] Okan Öner Ekiz, Mustafa Ürel, Hasan Güner, Alpay Koray Mizrak, and Aykutlu Dâna. Reversible electrical reduction and oxidation of graphene oxide. *ACS Nano*, 5(4):2475–2482, 2011.

[102] Luca Signorini, Luca Pasquini, Lorenzo Savini, Roberta Carboni, Federico Boscherini, Ennio Bonetti, Angelo Giglia, Maddalena Pedio, Nicola Mahne, and Stefano Nannarone. Size-dependent oxidation in iron/iron oxide core-shell nanoparticles. *Phys. Rev. B*, 68:195423, Nov 2003.

[103] Inder P. Batra and S. Ciraci. Ideal al-ge(001) interface: From chemisorption to metallization of the al overlayer. *Phys. Rev. B*, 29:6419–6424, Jun 1984.

[104] Adam Kiejna. Vacancy formation and o adsorption at the al(111) surface. *Phys. Rev. B*, 68:235405, Dec 2003.

[105] M. Vanin, J. J. Mortensen, A. K. Kelkkanen, J. M. Garcia-Lastra, K. S. Thygesen, and K. W. Jacobsen. Graphene on metals: A van der waals density functional study. *Phys. Rev. B*, 81:081408, Feb 2010.

[106] A. Buldum, D. M. Leitner, and S. Ciraci. Model for phononic energy dissipation in friction. *Phys. Rev. B*, 59:16042–16046, Jun 1999.

[107] M. Topsakal, E. Aktürk, H. Sevinçli, and S. Ciraci. First-principles approach to monitoring the band gap and magnetic state of a graphene nanoribbon via its vacancies. *Phys. Rev. B*, 78:235435, Dec 2008.

[108] A. Hashimoto, K. Suenaga, K. Gloter, A.and Urita, and S. Iijima. Direct evidence for atomic defects in graphene layers. *Nature*, 430:870–873, 2004.

[109] Johan M. Carlsson, Felix Hanke, Suljo Linic, and Matthias Scheffler. Two-step mechanism for low-temperature oxidation of vacancies in graphene. *Phys. Rev. Lett.*, 102:166104, Apr 2009.

[110] J. M. Garcia-Lastra. Strong dependence of band-gap opening at the dirac point of graphene upon hydrogen adsorption periodicity. *Phys. Rev. B*, 82:235418, Dec 2010.

[111] L. S. Panchakarla, K. S. Subrahmanyam, S. K. Saha, Achutharao Govindaraj, H. R. Krishnamurthy, U. V. Waghmare, and C. N. R. Rao. Synthesis, structure, and properties of boron- and nitrogen-doped graphene. *Advanced Materials*, 21(46):4726–4730, 2009.

[112] Rocco Martinazzo, Simone Casolo, and Gian Franco Tantardini. Symmetry-induced band-gap opening in graphene superlattices. *Phys. Rev. B*, 81:245420, Jun 2010.

[113] Rakesh P. Tiwari and D. Stroud. Tunable band gap in graphene with a noncentrosymmetric superlattice potential. *Phys. Rev. B*, 79:205435, May 2009.

[114] Cheol-Hwan Park and Steven G. Louie. Making massless dirac fermions from a patterned two-dimensional electron gas. *Nano Letters*, 9(5):1793–1797, 2009. PMID: 19338276.

[115] Marco Gibertini, Achintya Singha, Vittorio Pellegrini, Marco Polini, Giovanni Vignale, Aron Pinczuk, Loren N. Pfeiffer, and Ken W. West. Engineering artificial graphene in a two-dimensional electron gas. *Phys. Rev. B*, 79:241406, Jun 2009.

[116] Jingwei Bai, Xing Zhong, Shan Jiang, Yu Huang, and Xiangfeng Duan. Graphene nanomesh. *NATURE NANOTECHNOLOGY*, 5(3):190–194, MAR 2010.

[117] Jayeeta Lahiri, You Lin, Pinar Bozkurt, Ivan I. Oleynik, and Matthias Batzill. An extended defect in graphene as a metallic wire. *NATURE NANOTECHNOLOGY*, 5(5):326–329, MAY 2010.

[118] Richard Balog, Bjarke Jorgensen, Louis Nilsson, Mie Andersen, Emile Rienks, Marco Bianchi, Mattia Fanetti, Erik Laegsgaard, Alessandro Baraldi, Silvano Lizzit, Zeljko Sljivancanin, Flemming Besenbacher, Bjork

Hammer, Thomas G. Pedersen, Philip Hofmann, and Liv Hornekaer. Bandgap opening in graphene induced by patterned hydrogen adsorption. *NATURE MATERIALS*, 9(4):315–319, APR 2010.

[119] Cristina Bena and Gilles Montambaux. Remarks on the tight-binding model of graphene. *NEW JOURNAL OF PHYSICS*, 11, SEP 30 2009.

[120] L. M. Malard, M. A. Pimenta, G. Dresselhaus, and M. S. Dresselhaus. Raman spectroscopy in graphene. *PHYSICS REPORTS-REVIEW SECTION OF PHYSICS LETTERS*, 473(5-6):51–87, APR 2009.

[121] M. Methfessel and A. T. Paxton. High-precision sampling for brillouin-zone integration in metals. *Phys. Rev. B*, 40:3616–3621, Aug 1989.

[122] Oleg V. Yazyev and Lothar Helm. Defect-induced magnetism in graphene. *Phys. Rev. B*, 75:125408, Mar 2007.

[123] A Hashimoto, K Suenaga, A Gloter, K Urita, and S Iijima. Direct evidence for atomic defects in graphene layers. *NATURE*, 430(7002):870–873, AUG 19 2004.

[124] S. Cahangirov and S. Ciraci. Two-dimensional c/bn core/shell structures. *Phys. Rev. B*, 83:165448, Apr 2011.

[125] B. I. Yakobson, C. J. Brabec, and J. Bernholc. Nanomechanics of carbon tubes: Instabilities beyond linear response. *Phys. Rev. Lett.*, 76:2511–2514, Apr 1996.